

Horia Hulubei National Institute for Physics
and Nuclear Engineering
University of Bucharest

**Studies of transverse momentum
spectra and relative ratios of pions,
kaons and protons from high
multiplicity and azimuthally
symmetric events in p+p collisions
at 7 TeV with the ALICE experiment**

Cristian ANDREI

Supervisor
Prof. Dr. Mihai Petrovici

Thesis submitted for the degree of
Doctor of Philosophy

July 2013

Horia Hulubei National Institute for Physics and
Nuclear Engineering
University of Bucharest

Studies of transverse momentum spectra and
relative ratios of pions, kaons and protons from
high multiplicity and azimuthally symmetric
events in p+p collisions
at 7 TeV with the ALICE experiment

Cristian ANDREI

Supervisor
Prof. Dr. Mihai Petrovici

Doctoral Commission:

President: Prof. Dr. Stefan Antohe, University of Bucharest

Supervisor: Prof. Dr. Mihai Petrovici, IFIN-HH

Reviewers:

1. Dr. Amalia Pop, IFIN-HH
2. Dr. Stefan Berceanu, IFIN-HH
3. Prof. Dr. Virgil Baran, University of Bucharest

IMPORTANT NOTICE

All the plots presented in this thesis are either taken from a source that is cited in the respective figure caption or are the results of the presented analysis and, consequently, labeled as “This Work”. These plots are not yet approved by the ALICE Collaboration and do not represent ALICE official results.

Exception: The two plots from the *Addendum* (Fig. 11.1 and 11.2) are the results of this analysis and were approved, recently, as “Preliminary” by the ALICE Collaboration.

Contents

1	Introduction	4
2	Theoretical Framework	6
2.1	Phase Diagram of Strongly Interacting Matter	6
2.2	Motivation of the Present Study	11
3	Existing experimental results	15
3.1	Collective phenomena in heavy ion collisions	16
3.2	Search for collective phenomena in p + p(\bar{p}) collisions	21
4	The ALICE Experiment	24
4.1	Large Hadron Collider (LHC)	24
4.2	A Large Ion-Collider Experiment (ALICE)	25
4.2.1	Inner Tracking System (ITS)	25
4.2.2	Time-Projection Chamber (TPC)	27
4.2.3	Transition Radiation Detector (TRD)	27
4.2.4	Time Of Flight (TOF)	28
4.2.5	T0	29
4.2.6	V0	30
4.3	ALICE Computing framework	30
5	Event and Track Selection	33
5.1	Event selection	33
5.2	Multiplicity distribution	36
5.3	Track selection	39
6	Particle Identification	42
7	Corrections	48
7.1	Tracking efficiency	49
7.2	Matching efficiency	50
7.3	PID efficiency and percentage of misidentified particles	51
7.4	Material and weak decay contamination	53
7.5	Multiplicity dependence of the corrections	55

7.6	Trigger and Vertex efficiencies	59
7.7	Distribution of the vertex on the z-axis	60
7.8	Monte-Carlo closure test	61
8	Systematic errors	64
8.1	Variation of the track quality cuts	64
8.2	Influence of the TRD subdetector	66
8.3	PID procedure	66
8.4	Tracking and matching	70
8.5	Multiplicity variation of the corrections	70
8.6	Combined systematic errors	72
9	p_T distributions	75
9.1	Comparison with similar MB p_T spectra	75
9.2	Comparison with similar p_T spectra as a function of multiplicity	77
9.3	p_T spectra as a function of multiplicity	81
9.4	Comparison with models predictions	83
9.5	$\langle p_T \rangle$ and particle ratios multiplicity dependence	85
10	Azimuthally symmetric events	90
11	Conclusions	95
	Addendum: <i>Preliminary</i> ALICE plots	97
	Appendix A: Analysis Task Schema	100
	Appendix B: ALICE Coordinate System	103
	List of Figures	105
	List of Tables	110
	Bibliography	111

Chapter 1

Introduction

The high energy collisions of hadrons and heavy ions are the only experimental way of recreating, even for a very short time and in a very small volume, the state of the Universe as it was, based on cosmological scenarios, at about a microsecond after the Big Bang. The collective effects evidenced in these systems are crucial for probing the production of such a deconfined state of quarks and gluons and for the study of its properties and dynamics. As it will be shown in this thesis, the transverse momentum distributions of the particles that are created as these systems expand and cool down, are carrying information from the deconfined state and their study provides a very promising way of understanding the involved processes.

This Introduction is followed by a short overview of the high energy physics field that represents Chapter 2 of this thesis. A description of the phase diagram of strongly interacting matter is included in this Chapter along with a motivation of the present study.

Chapter 3 starts with a review of past, present and future experimental devices and it is divided in two Sections presenting experimental heavy-ion results concerning the collective phenomena as well as the search of collective phenomena in proton-proton collisions.

The ALICE (***A** Large Ion Collider **E**xperiment*) experimental device is described in Chapter 4. The Chapter starts with a enumeration of the accelerator parameters during the year 2010 when the data sample used in this analysis was obtained. Then, a short technical description of the sub-detectors that provide the experimental observables used in this analysis and of the computing environment are included.

In Chapter 5 are summarized the selections applied for the events and the tracks that are analyzed. To explain the choice of these selections criteria the trigger schemes and the vertex reconstruction algorithm are described. Also, the tracking algorithm is discussed as well as the used multiplicity estimator. The highly complex procedure that provides the identification of charged hadrons is described in Chapter 6.

This is followed, in Chapter 7 by an extensive discussion of all the corrections that are applied in order to obtain the final p_T spectra. The behavior of these

corrections as a function of multiplicity was also studied and details on this study are presented in this Chapter.

The procedure used to estimate the systematic errors that are associated with p_T spectra and the final values obtained for these errors as a function of p_T are presented in Chapter 8.

The fully corrected p_T spectra are presented in Chapter 9. Comparisons with results from similar analysis for the minimum bias (MB) spectra as well as multiplicity bins spectra are also included. Finally the mean p_T as a function of multiplicity and the parameters obtained from fits of the spectra with a Boosted Boltzmann-Gibbs formula end this Chapter.

The performance of the event shape observable directivity and the p_T spectra obtained by selecting events using this observable are shown in Chapter 10. Finally, in Chapter 11 the obtained results are summarized and the perspectives are discussed.

The thesis ends with an Addendum presenting the results of the present analysis that were approved by the ALICE Collaboration as *preliminary*, followed by two Appendixes that described the software that was developed for this analysis and the ALICE experiment coordinates system.

Chapter 2

Theoretical Framework

2.1 Phase Diagram of Strongly Interacting Matter

As it is well known, a basic property of the QCD as a non-Abelian gauge theory of quarks and gluons is the asymptotic freedom, namely the running coupling constant expressed in terms of QCD intrinsic scale parameter Λ as can be seen in Eq. 2.1, becomes small for momentum transfer Q^2 much larger than Λ^2 . Therefore, a perturbative description in terms of quarks and gluons becomes applicable.

$$\alpha_s(Q^2) = \frac{12\pi}{(33 - 2n_f)\log(Q^2/\Lambda^2)} \quad (2.1)$$

For Q^2 at the level of Λ^2 the quarks and gluons are strongly bound in states called hadrons. As it can be seen in Fig. 2.1 [1], the running coupling constant is by now confirmed by experiments to a very high precision and the authors: Gross, Wilczek and Politzer were awarded the Nobel Prize in physics for this prediction.

A qualitative representation of the property of QCD can be seen in Fig. 2.2 and Fig. 2.3 where the behavior of electric and color screening, respectively are represented.

In Quantum Field Theory an electron can suddenly emit a photon or it can emit a photon which subsequently annihilates into a electron-positron pair and so on. As a consequence an electron in quantum field theory can exhibit itself like in Fig. 2.2 being surrounded by e^+e^- pairs and due to Coulomb interaction the positrons are preferentially closer to the electron. If we want to measure the charge of the electron via the Coulomb force experienced by a test charge, the measured charge becomes larger approaching the electron. Color charge screening would behave similarly if gluons would not turn into pairs of gluons. This reverses the above description characteristic to quantum electrodynamics, i.e. a red charge being surrounded preferentially by other red charges as it shown on the right plot. Therefore when a test probe

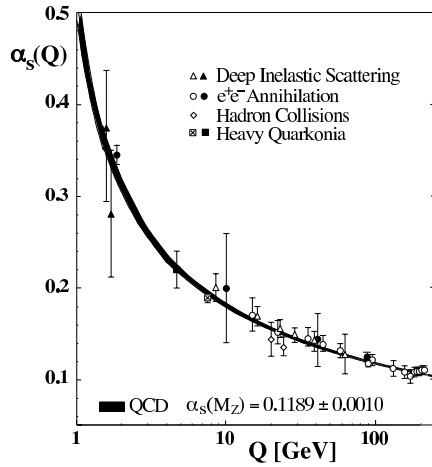


Figure 2.1: The running coupling constant as a function of Q [1].

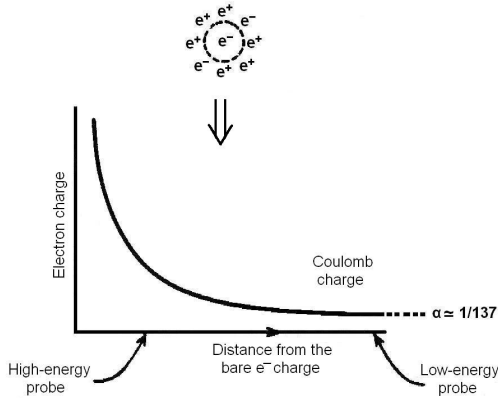


Figure 2.2: QCD electric screening [2].

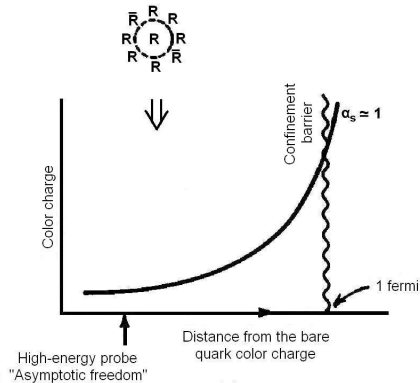


Figure 2.3: QCD color screening [2].

moves closer to the original red quark, the probe penetrates a sphere of predominantly red charge and the amount of measured red charge decreases. The resulting “antiscreening” of the red color is known as “asymptotic freedom” [2]. Therefore, at high density, $Q^2 \gg \Lambda^2$ is expected to be true and one could think of a transition from hadrons to on shell quarks and gluons. QCD in equilibrium can be characterized by two parameters, i.e. temperature T and barionic number density ρ_B .

In a grand canonical ensemble baryon chemical potential can be introduced as a conjugate variable to the baryon density.

Since the intrinsic scale of QCD is $\Lambda_{QCD} \sim 200$ MeV, it is expected that the QCD phase transition could take place around $T \sim \Lambda_{QCD} \sim O(10^{12}K)$ or $\rho_B \sim \Lambda_{QCD}^3 \sim 1fm^{-3}$. Qualitatively this can be followed in the sequence in Fig. 2.4. At low density we have to do with strongly bound clusters called hadrons.

If they are compressed by any means such that they start to overlap at about

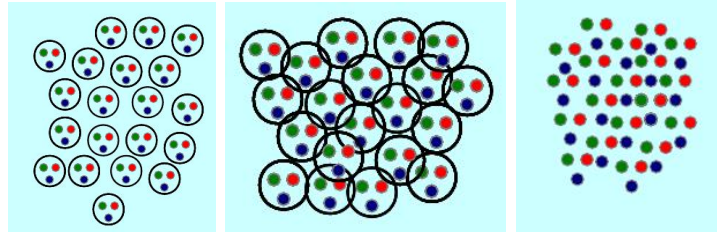


Figure 2.4: Strongly bound clusters: hadrons (left); Phase transition (middle); Weakly interacting: quarks and gluons (right) [3].

$1 fm^{-3}$ they start to lose their identity and a phase transition to weakly interacting quarks and gluons takes place.

First prototype of QCD phase diagram in $T - \rho_B$ plane was proposed by Cabibo and Parisi [4], Hagedorn's limiting temperature being interpreted as a critical temperature T_c for a second-order transition.

Within the hadron resonance picture of Hagedorn the density of states (mostly mesonic) as a function of mass is proportional with e^{m/T^H} where $T^H \sim 0.19$ GeV. The exponential growing is balanced by Boltzmann factor of the partition function. When $T > T^H$ the integration over m becomes singular, therefore T^H plays the role of limiting temperature.

The same argument is applied to critical value μ_B . For temperature $T > (1 - \mu_b/m_B)T_B^H$ the integration over m becomes singular. The critical value of μ_B at zero temperature is given by $m_B (\leq 1 \text{ GeV})$. Weakly interacting quark matter at large baryonic density due to asymptotic freedom has been recognized by Collins and Perey in mid 70's [5].

Besides the local gauge symmetry, in QCD has to be considered also the chiral symmetry which is exact in the limit of vanishing quark masses Fig. 2.5. Quantum fluctuations of QCD vacuum are responsible for the generation of

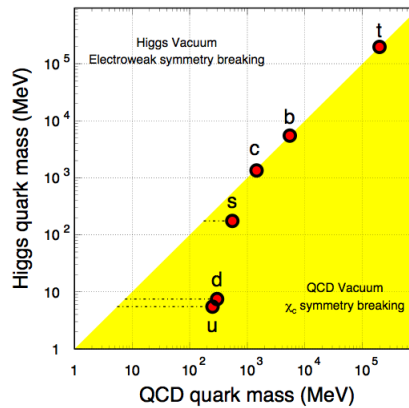


Figure 2.5: Quark masses in the QCD vacuum and the Higgs vacuum [6].

non-perturbative quark masses.

In a hot and dense medium it is expected that quarks turn bare due to asymptotic freedom and a phase transition from a state with heavy constituent quarks to light current quarks takes place. This is called Chiral phase transition.

A QCD critical point at $\mu_B = \mu_E$, $T = T_E$ is suggested by most of the chiral models.

For $\mu_B > \mu_E$ the chiral transition becomes a first-order transition and for $\mu_B < \mu_E$ it is a cross-over for realistic u, d and s quarks masses. There are also predictions for another critical point F at low T and high μ_B (μ_F , T_F) below which the cold dense QCD matter with 3 degenerate flavors has no border between superfluid nuclear matter and superconducting quark matter.

Non-vanishing density of nuclear matter starts arising at $\mu_B = \mu_{NM} = 924$ MeV $= m_N$, the density varies from zero to normal nuclear density $\rho_0 = 0.17$ fm⁻³. For $0 < \rho_B < \rho_0$ the nuclear matter is fragmented in droplets. This is typical first-order phase transition of liquid-gas type which eventually ends up with a second order critical point at (μ_G, T_G) .

Statistical models, based on the assumption of a gas of non-interacting mesons, baryons and resonances in thermal equilibrium, extract the temperature T and chemical potential μ_B by fitting particle ratios or yields at different collision energies. The extracted values of T and μ_B clusterize along a curve in the $\mu_B - T$ plane called chemical freeze-out line. Although there are arguments in claiming that the chemical freeze-out is located close to the phase transition, the freeze-out line is not associated with any QCD phase boundaries. Along this line the thermal degrees of freedom are dominated by mesons for $\mu_B \ll \mu_N$ and at higher μ_B more baryons are excited. This indicates that there must be a transitional change at (T_H, μ_T) where the importance of baryons in thermodynamics surpasses that of mesons. This takes place at about $\mu_H = 350$ -400 MeV and $T_H = 150$ -160 MeV according with statistical model analysis.

Such a phase structure is suggested by large N_c limit of QCD. In this limit the quarks loops are suppressed by $1/N_c$ relative to gluon contribution and we have to do with a cold dense matter called quarkonic matter. Therefore one could expect in fact three regions, confined, deconfined and quarkonic phase separated by 1st order phase transitions. The meeting point of these is the triple point whose remanent for finite N_c is indicated by H in Fig. 2.6. Based on these considerations a representation of the QCD phase diagram with boundaries defining different states and critical points looks like the one presented in Fig. 2.7 [7].

In nature, according to Big Bang cosmology, matter composed of quarks and gluons was specific for a few microseconds after the Big Bang characterized by negligible baryon chemical potential and high temperature while the deep interior of stellar objects such like neutron stars would be the place where QCD matter at low temperature could exist.

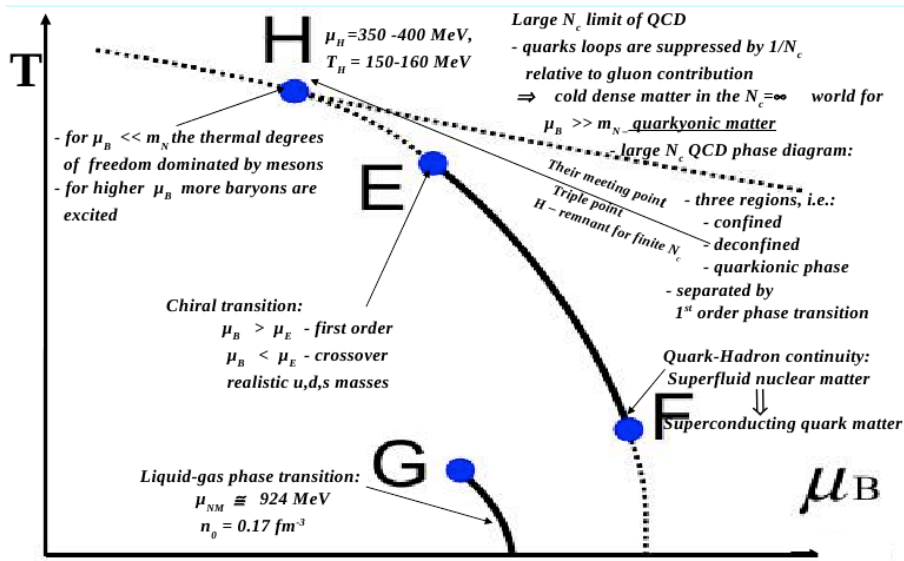


Figure 2.6: QCD critical points and phase boundaries [3].

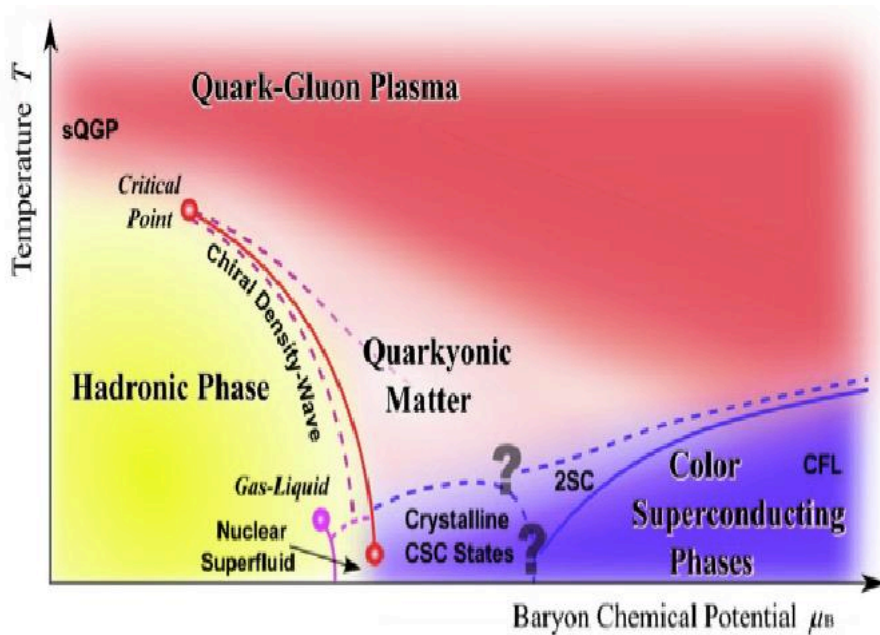


Figure 2.7: QCD Phase Diagram [7].

The first natural question which comes is in which extent such states of matter can be produced in the laboratory. Fig. 2.8 is a space-time diagram of two colliding nuclei and of the sequence of processes taking place, left side - without producing deconfined matter and right side - producing deconfined matter. Obviously an experimental setups measures only the products which survive long enough to reach it as it is represented in the upper part of

Fig. 2.8.

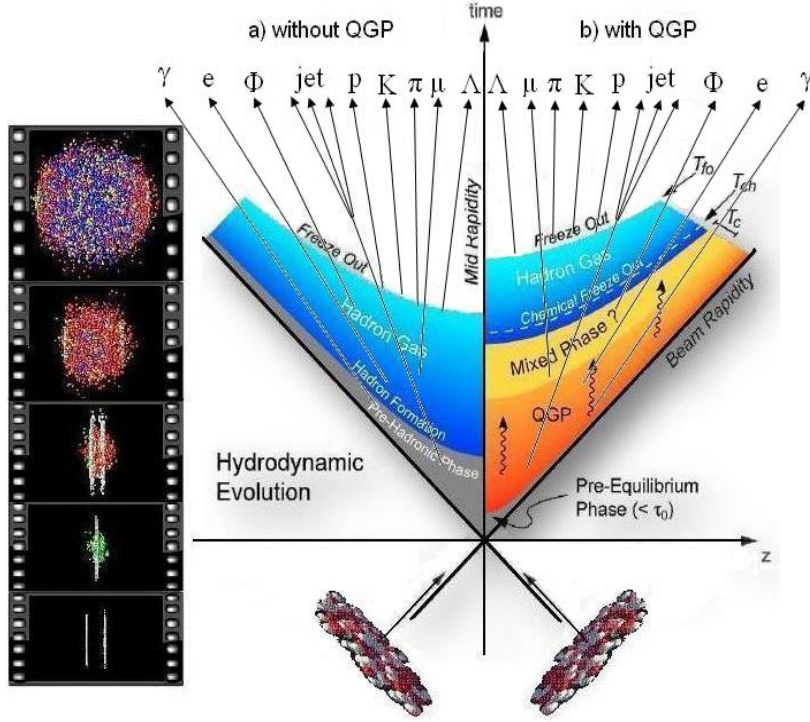


Figure 2.8: Space-time diagram of a collision process [3].

The second question is in which extent from measuring these products and their properties one could reconstruct backwards the properties of each step in the evolution.

It is worth mentioning here the three aspects which have to be considered from the very beginning, i.e. i) even in the case of the collision of the heaviest ions, the size of the system which is created in the laboratory is finite and rather small, ii) the initial state of the system is highly non-homogeneous, iii) the system is not a static object, on the contrary, it has a rather violent evolution in time, dynamical effects playing an important role.

2.2 Motivation of the Present Study

As it was already mentioned above, typical hadronic interactions are soft processes which occur at large distance of the order of hadron radius $r^{(soft)} \sim R_{hadron}$, therefore they have large cross section $\sigma^{(soft)} \sim R_h^2$ and perturbative QCD can not be applied. Opposite to these, conventional hard processes are those processes where a highly virtual object with off-shell mass $q^2 \gg 1/R_h^2$, therefore with very small dimension, hits a hadron and carries away a large portion $x \sim 1$ of the initial hadron energy. Such processes take place at small distances, much smaller than hadron radius $1/(q^2)^{1/2} \ll R_h$ and

thus the perturbative QCD can be applied and their cross section is small. Semihard processes are those in which a virtual probe knocks out only a small portion of hadron energy $x \ll 1$. Although the cross section is small the initial hadron is densely populated by partons with small dimensions and the global cross section turns out to be rather large making it more like a soft process. Unlike soft processes the semihard ones take place at small distance and can be calculated in perturbative QCD.

The main feature of a deep inelastic process in the semihard region can be easily understood if one considers the hadron as a continuous medium of partons [8]. Although this approximation looks quite rough, it turns out to be quite reasonable, in good agreement with the results obtained using explicit perturbation calculations. Let's consider a point like probe called "partonometer" which for sake of simplicity is chosen to be a virtual photon γ^* and the associated Breit frame where $q = (0,0,0,-q_z)$, $p = (p_0,0,0,p_z)$; $\sqrt{-q^2} = q_z = 2x_B p_z$. In the Breit reference frame the hadron is very fast and due to Lorentz constriction it can be considered as a disk of radius R_h with an area of $A \sim R_h^2$ with a momentum p_z , filled with a continuous medium probed by the γ^* . The interaction time between hadron and γ^* is $\tau_{int} \sim 1/q_z = 1/\sqrt{-q^2}$ probing an area $\Delta A \sim 1/q^2$ carrying a momentum $\Delta p_z = (\Delta A/A)p_z = p_z/(q^2 R_h^2)$. The interaction is possible if $x = x_B = 1/(q^2 R_h^2)$ (Fig. 2.9).

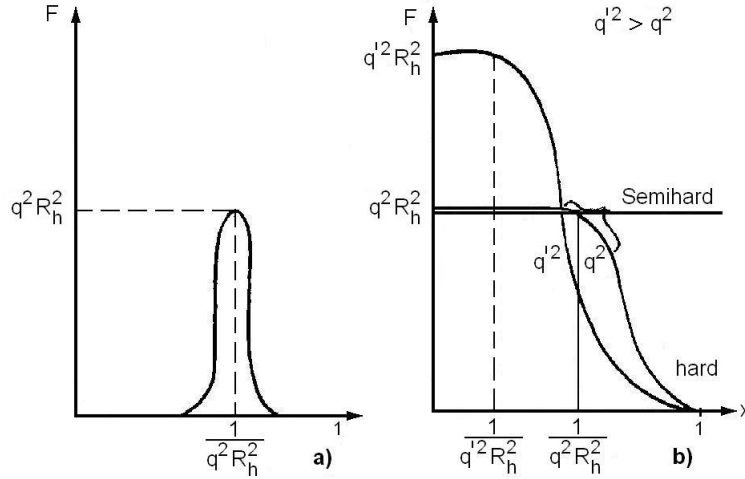


Figure 2.9: (a) The structure function F in the continuous medium model; (b) The same with the fluctuations taken into account [8].

A convenient way to characterize a deep inelastic process is the number of partons which absorb a photon, $F(x, q^2)$, connected with the structure function $D(x, q^2)$: $F = xD$. Therefore the cross section for a γ^* absorption is $\sigma^{\gamma^*} \sim (\alpha_{e.m.}/q^2)F(x, q^2)$. In the case of solid medium approximation the number of pieces (partons) seen by γ^* as a function of x has a δ distribution

(Fig. 2.9a). When x is different than $1/(q^2 R_h^2)$ the photon does not see any pieces, i.e. the interaction is not possible, while for $x=1/(q^2 R_h^2)$ the photon sees $F(x)=A/\Delta A = q^2 R_h^2$ partons, as a consequence of the fact that there are $A/\Delta A$ pieces of area ΔA in a disc A . As it was mentioned above, this is the outcome of the continuum partonic medium approach.

In reality the hadron is different:

- for a fast hadron a parton with a given x lives for long time and can easily decay in a number of partons carrying smaller momenta - gluon bremsstrahlung in QCD, one of them absorbing the γ^*
- if the hadron is slow ($x > 1/(q^2 R_h^2)$) an average piece ΔA has not enough energy to absorb the photon, however, in the real hadron, fluctuations are possible, $F(x)$ decreases rapidly with x but is not zero and the result can be seen in (Fig. 2.9b).

In each decay a parton produces two new partons, x_i being the fraction of hadron energy carried by partons. The transverse dimension $\Delta b_{i\perp} \sim 1/k_{it}$ of the partons produced in a decay are much smaller than those of their parent, their transverse dimension decreasing from $\Delta b_{\perp}^{hadron} \sim R_h$ to $\Delta b_{\perp}^{gamma^*} \sim 1/\sqrt{(q^2)}$. The cascade can be in this way characterized by a trajectory $b_{i\perp}(x_i)$ represented in (Fig. 2.10). In QCD the probability for parton decay is determined by the coupling constant α_s . Due to the fact that asymptotic freedom α_s increases with b_{\perp} , partons with large b_{\perp} decay faster than those with smaller b_{\perp} and, as a consequence, the density of the parton population has a maximum somewhere in the middle.

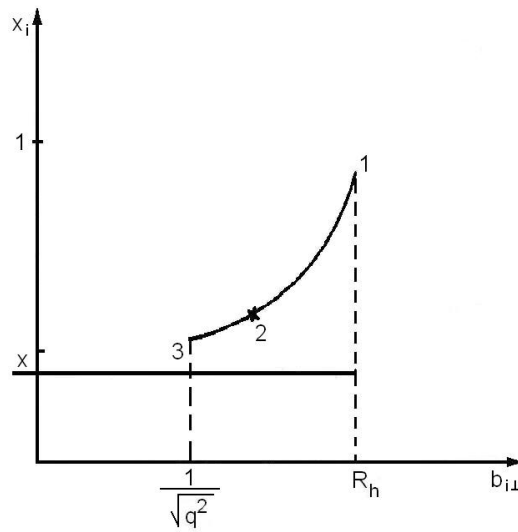


Figure 2.10: $b_{i\perp}(x_i)$ trajectory of the cascade [8]

A schematic representation of these considerations is shown in Fig. 2.11. Therefore, a fast free hadron is at each moment a cloud of quasireal partons which belong to a cascade. If the parton of the cascade meets on its way an object, interacts with it, the whole cascade changes, the coherence is broken, the partons can not assembly back, they continue to live and decay in secondary hadrons and last but not least the struck cascade could interact with the others. Indeed, multi parton interactions, double and triple partonic

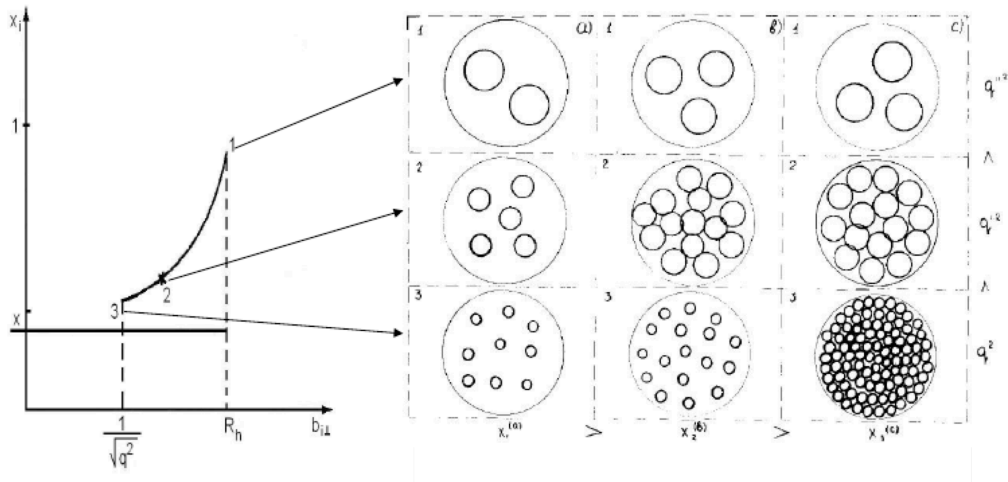


Figure 2.11: Interaction between partons correlated with the position in the cascade [8]

collisions, and their cross sections as a function of $\ln s$, where s is the energy in the center of mass of the colliding system, were evidenced at Tevatron energy [9, 10]. At about 4 times larger incident energy, the case of the present study, such processes contribute to a large energy transfer in the collision volume of proton size. If deconfinement is produced and one considers a mean free path of $\sim 0.2-0.3$ fm for its constituents, estimated from QGP viscosity, and that two-three collisions are in principle sufficient for thermalization, a close to equilibrium deconfined initial state could be expected. Therefore is quite probable that at such energies, a piece of matter of proton size, with a radius a few times larger than the mean free path, hydrodynamically explodes once the energy transfer becomes significantly large [11, 12, 13, 14].

Chapter 3

Existing experimental results

An overview of the existing and under construction facilities which deliver heavy ions and hadron beam of different energies, from a couple of GeV up to 2.76 TeV per nucleon pair for heavy ions and up to 8 TeV for protons in the center of mass is presented in Fig. 3.1. While at energies covered by Beam Energy Scan (BES) program at RHIC and future FAIR and NICA facilities one could reach the largest freeze-out baryon density, based on microscopic transport model calculations estimates, at LHC energies is reached the highest energy density and temperature of matter.

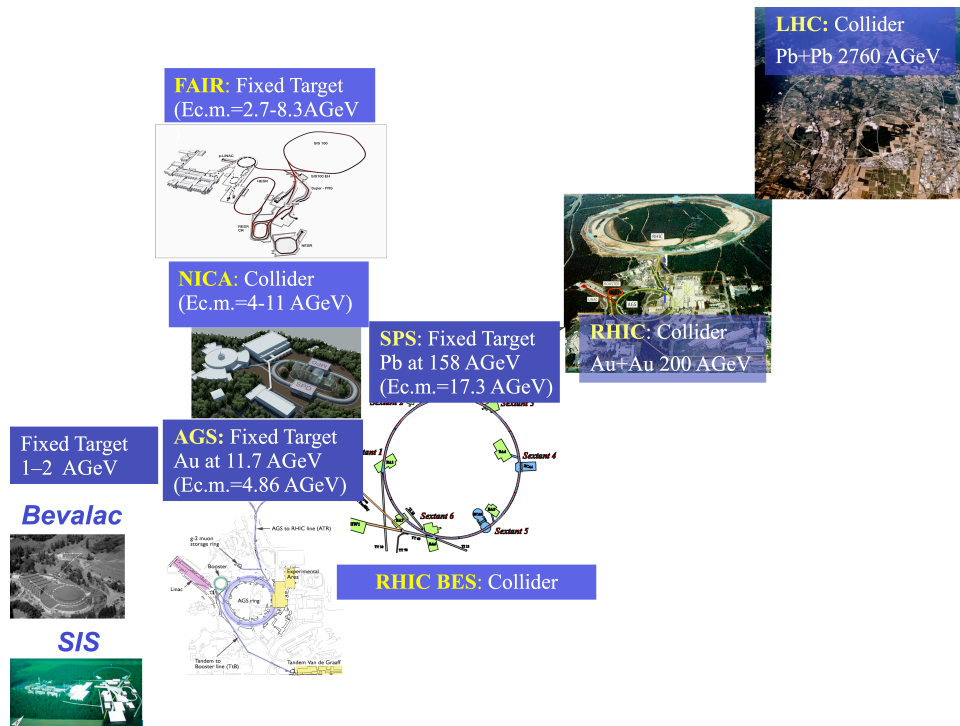


Figure 3.1: Overview of the existing and under construction experimental facilities [3].

Detailed mapping of Phase Diagram presented in Fig. 2.6 and Fig. 2.7 in terms of temperature (T) and density (μ_B) is the main focus of the BES program at RHIC and future facilities NICA and FAIR with the aim to evidence and study the properties of matter in different phases, phase transition borders and their types and a possible support for the existence of critical point predicted by lattice QCD calculations. At LHC, where the highest temperature and energy density could be reached in the laboratory, using the advantage of accessing besides Pb+Pb collisions at 2.76 TeV also p+Pb and p+p collisions at similar energies, is possible not only to create deconfined matter but also to understand details of its properties and dynamics starting from the simplest case of p+p collisions.

3.1 Collective phenomena in heavy ion collisions

In the collisions of heavy-ions large systems are created, particles within suffer multiple interactions and this leads to a large pressure build-up. The collective expansion of the matter that is being populated in ultra-central collisions, driven by the pressure, is known as *radial flow*. If the pieces of this matter are moving with the same velocity then the heavier particles will have a larger momentum. Therefore, by studying the shape of the p_T spectra for particles with different masses, the velocity of this flow can be extracted. Another observable that is used in order to characterize the collective expansion is the azimuthal anisotropy, known as *elliptic flow*. In ultra-central collisions the radial flow is the dominant component, while the elliptic flow, which depends on the system's initial asymmetry dominates the semi-central and peripheral collisions. This asymmetry of the initial state creates an energy density gradient and, following this gradient, the flow will be stronger on the direction of the small axis of the elliptical overlap region (*in-plane*) then on the direction of the long axis (*out-of-plane*), which leads to an anisotropy of the momenta of the produced particles. This anisotropy can be described by using a Fourier decomposition of the azimuthal distribution:

$$E \frac{d^3 N}{d^3 p} = \frac{1}{2\pi} \frac{d^2 N}{p_t dp_t dy} \left(1 + \sum_{n=1}^{\infty} 2\nu_n \cos(n(\phi - \Psi_r)) \right)$$

$$\nu_2 = \langle \cos 2(\phi - \Psi_r) \rangle, \phi = \tan^{-1} \left(\frac{p_y}{p_x} \right),$$

where Ψ_r is the reaction plane angle.

The evolution of the second coefficient (ν_2) of the mentioned decomposition as a function of the beam energy is showed in Fig. 3.2.

As it can be seen, for energies below 100 A·MeV the emission takes place predominantly in-plane, while at larger energies this emission goes mainly on a direction which is perpendicular on the reaction plane. For energies above

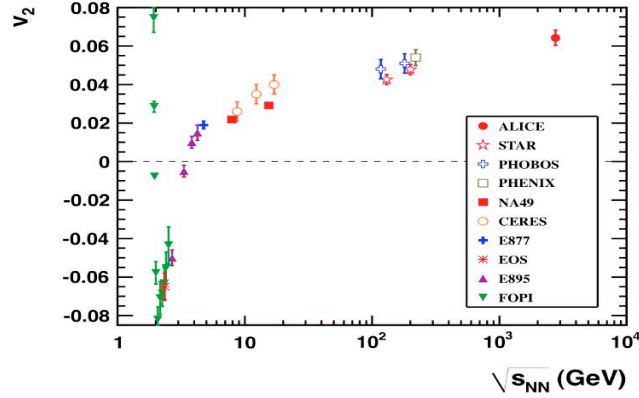


Figure 3.2: Elliptic flow as a function of the beam energy [15].

4 A·GeV the v_2 becomes again positive, which shows a predominant in-plane emission. More recent results from RHIC show that this trend continues while the energy increases with an order of magnitude [16].

The flow at the RHIC energies is characterized by the scaling of this flow as a function of the number of quarks. The $v_2/(\text{no. of quarks})$ as a function of the transverse kinetic energy, also scaled to the number of quarks, is shown in Fig. 3.3. This scaling was interpreted as a signature that, at the time of hadronization the quarks are the dominant degree of freedom [17].

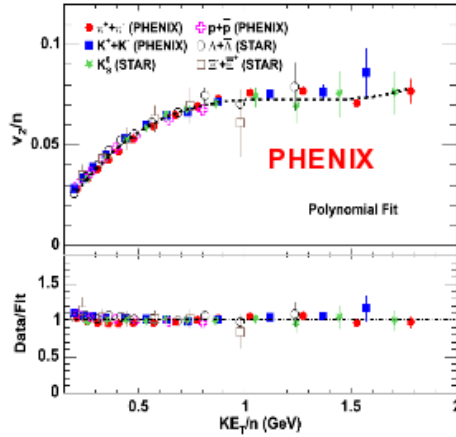


Figure 3.3: v_2/n_q as a function of E_{kt}/n_q [17].

The transverse momentum distributions of the identified particles, as obtained by the STAR experiment at RHIC, can be well described using a hydrodynamic model in which a mean expansion velocity $\langle \beta \rangle$ and a freeze-out temperature T_{kin} are considered. These p_T distributions, obtained in Au+Au collisions at 200 A·GeV are shown in Fig. 3.4.

The behavior of these two parameters as a function of the particle multiplicity is shown in Fig. 3.5. Their values are compared with the chemical

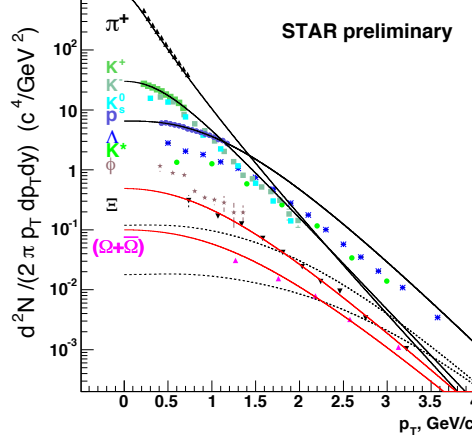


Figure 3.4: p_T distributions for all the identified species [18].

temperature T_{ch} , which is obtained by reproducing the production probabilities ratios of different hadrons using statistical models. One can see that with the increase of the multiplicity the kinetic temperature decreases, the chemical temperature remains constant and $\langle \beta \rangle$ increases. The strange hadrons do not follow the general trend: they have a high T_{kin} , close to the chemical one, and a smaller expansion velocity. This behavior and the fact that these hadrons have a low hadron interaction cross-section suggests that they retain information from the partonic stage of the expansion [18].

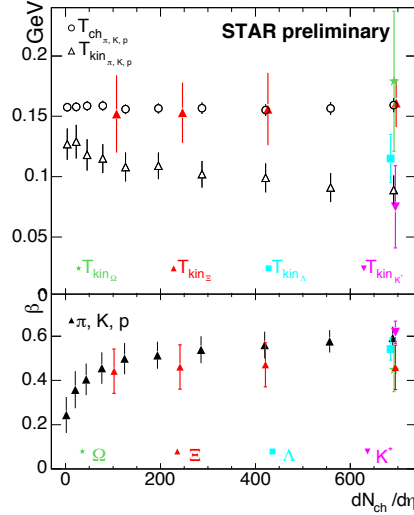


Figure 3.5: top: T_{kin} as a function of multiplicity and comparison with T_{ch} ; bottom: $\langle \beta \rangle$ as a function of multiplicity [18].

In Fig. 3.6 the behavior of the chemical and the kinetic freeze-out temperatures as a function of the collision geometry is shown. As it can be seen the

chemical temperature rises steeply up to about 10 GeV collision energy and then it saturates, the values it reaches being close to the transition temperature predicted by lattice QCD.

The kinetic freeze-out temperature is similar with the chemical one at low energies but then it decreases at higher energies. This can be explained by the fact that the period between the chemical and the kinetic freeze-outs increases with the increase in energy and, in this period, the system continues to expand and cool.

The behavior of the $\langle \beta \rangle$ as a function of the collision geometry is shown in Fig 3.7. This flow velocity always increases with the increase of the collision energy, but the rate of this increase is lower at higher energies. The collective flow that this parameter quantifies is the sum of the one that is produced in the early phase of the evolution, before chemical freeze-out, and the one that is produced afterwards.

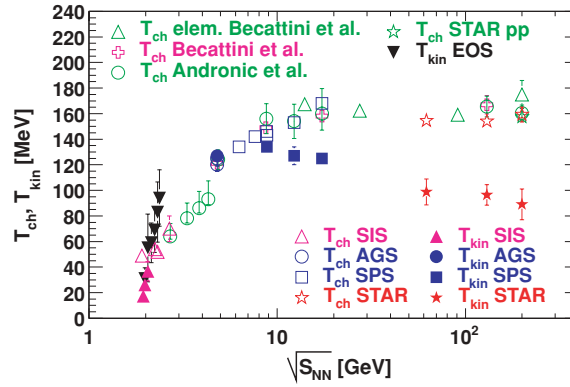


Figure 3.6: Extracted chemical (open symbols) and kinetic (filled symbols) freeze-out temperatures for central heavy-ion collisions as a function of the collision energy [19].

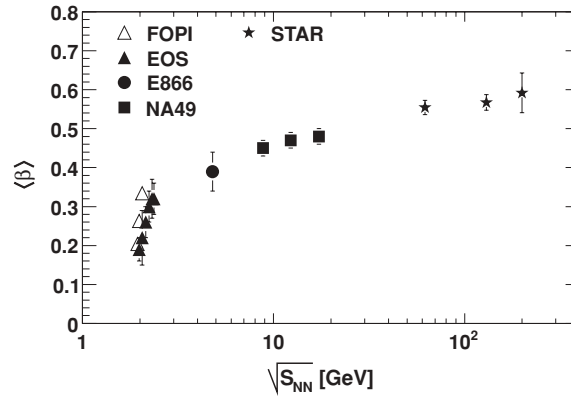


Figure 3.7: Average transverse radial flow velocity extracted from the blast-wave model for central heavy-ion collisions as a function of the collision energy [19].

Plotting the $\langle p_T \rangle$ as a function of mass for π^- , k^- and \bar{p} for different colliding systems: p+p, Cu+Cu and Au+Au, an increase of the slope is observed at the same incident energy (200 A·GeV). Also, the same phenomena was observed if one considers the same system (Au+Au) at different energies (Fig. 3.8).

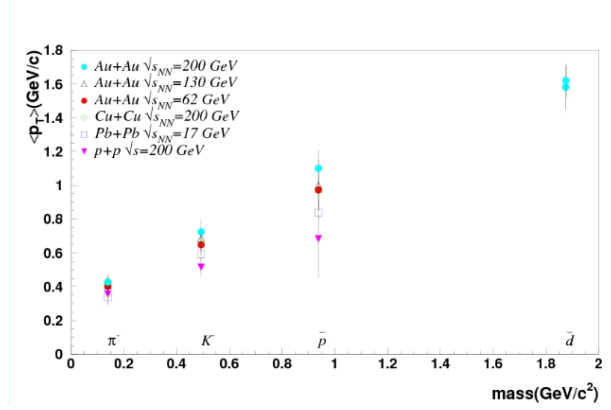


Figure 3.8: $\langle p_T \rangle$ as a function of mass for p+p, Cu+Cu and Au+Au collisions [20].

If all the identified hadrons from p+p and central Au+Au collisions at 200 A·GeV are considered (STAR published data compilation [21]) and the experimental data are fitted with an expression which includes collective flow on top of local thermal equilibrium within the error bars the obtained T_{kin} has the same value for the two systems (Fig. 3.9). The much larger expansion velocity obtained for Au+Au collisions can be explained by the fact that, in this case, the partonic expansion continues at the hadronic level.

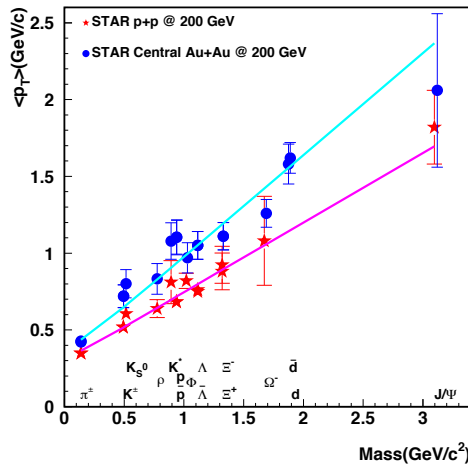


Figure 3.9: $\langle p_T \rangle$ as a function of mass for p+p and Au+Au collisions, compilation of STAR published data [22].

If only the strange hadrons and the J/ψ from Au+Au collisions are considered, the value obtained for $\langle \beta \rangle$ is 0.36 and the T_{kin} value: 172 MeV, is close to the critical temperature predicted by theoretical models for the phase transition. For the other hadrons the value for $\langle \beta \rangle$ is larger (0.59) and the T_{kin} value is smaller (104 MeV). This can be explained by the fact that, for these hadrons, the expansion continues at the hadronic level and they cool down and achieve a larger velocity.

These studies show that a proper analysis of the transverse momentum spectra can be used to extract information about the expansion and the temperature in the different phases of the matter populated in these collisions [22, 20, 23].

3.2 Search for collective phenomena in $p + p(\bar{p})$ collisions

Transverse momentum spectra of identified charged hadrons in $p+p(\bar{p})$ collisions were studied as a function of incident energy below 900 GeV at CERN ISR and Sp \bar{p} S [24] and up to 1800 GeV at Fermilab Tevatron [25] colliders. While UA5 Collaboration reported, starting from 200 GeV, an increase of $\langle p_T \rangle$ of kaons in the central region larger than that expected based on ISR data (Fig. 3.10), the E735 Collaboration evidenced a mass dependent slope of $\langle p_T \rangle$ as a function of c.m. energy from 300 to 1800 GeV (Fig. 3.11).

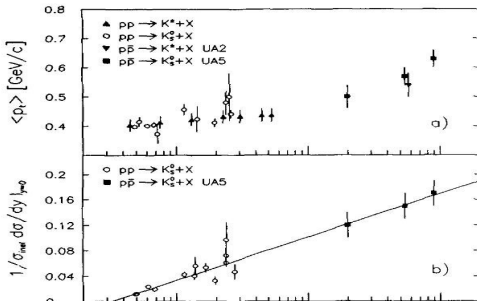


Figure 3.10: UA5: $\langle p_T \rangle$ of kaons in the central region as a function of c.m. energy [24].

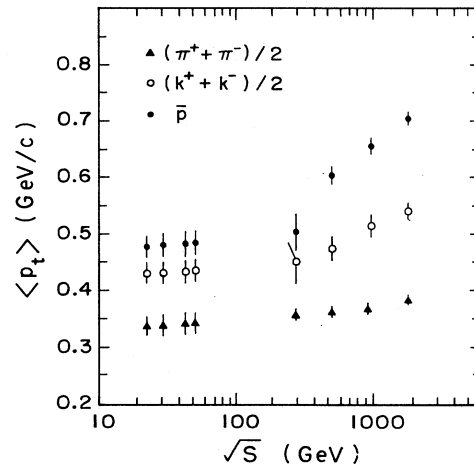


Figure 3.11: E735: $\langle p_T \rangle$ of π , K and \bar{p} as a function of c.m. energy [25].

Definitely such trend which significantly deviates from a $\ln(s)$ (Fig. 3.12) extrapolation from lower energies measured at ISR [26] cannot be explained by models based on statistical equilibrium (Fig. 3.13) [27, 28, 29].

Detailed studies of E735 Collaboration at 1800 GeV have shown that the increase of $\langle p_T \rangle$ with $dN_c/d\eta$ depends on the mass of particle (Fig. 3.14)

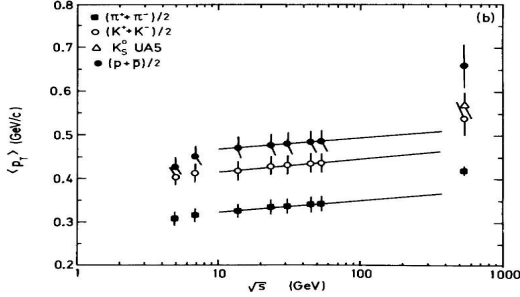


Figure 3.12: $\langle p_T \rangle$ vs. $\ln(s)$ extrapolations [26].

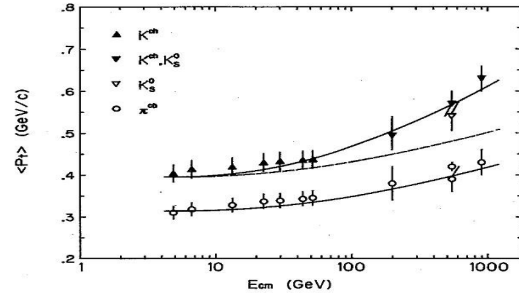


Figure 3.13: $\langle p_T \rangle$ statistical models [29].

[25].

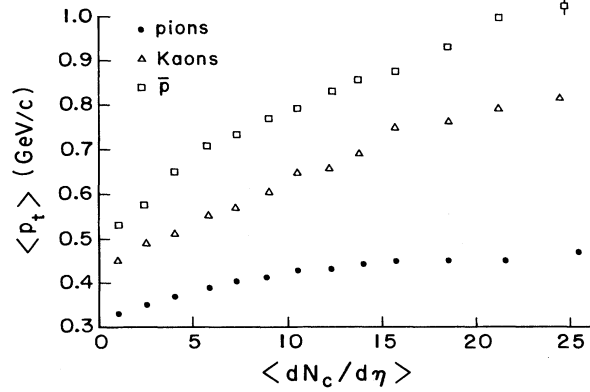


Figure 3.14: E735: $\langle p_T \rangle$ at 1800 GeV as a function of $\langle dN_c/d\eta \rangle$ [25].

These studies are of real interest for different QCD inspired models like PYTHIA [30, 31] or EPOS [32] which predict such a dependence as a consequence of multi-parton interactions or of a hydrodynamic type evolution with flux tube initial conditions. CDF Collaboration, comparing two energies, i.e. 630 GeV and 1800 GeV, evidenced an energy invariance of the $\langle p_T \rangle$ distribution at fixed multiplicity for soft interactions (Fig. 3.15) [33].

This shows that the multiplicity of produced particles is a measure of the amount of energy involved in the process. Such a conclusion is supported by recent low relative momentum two-pion correlation studies at 0.9 and 7 TeV (Fig. 3.16) [34] which evidenced that the correlation functions at the two energies are similar at a given multiplicity, the size of the emitting system growing with the charged particle multiplicity of the event.

It was also evidenced that double and triple partonic interactions start to be significant at higher energies and their cross sections seem to increase linearly with $\ln(s)$, where s is the energy in the center of mass of the colliding system (Fig. 3.17) [9, 10].

At about 4 times larger incident energies, as is the case of the present study,

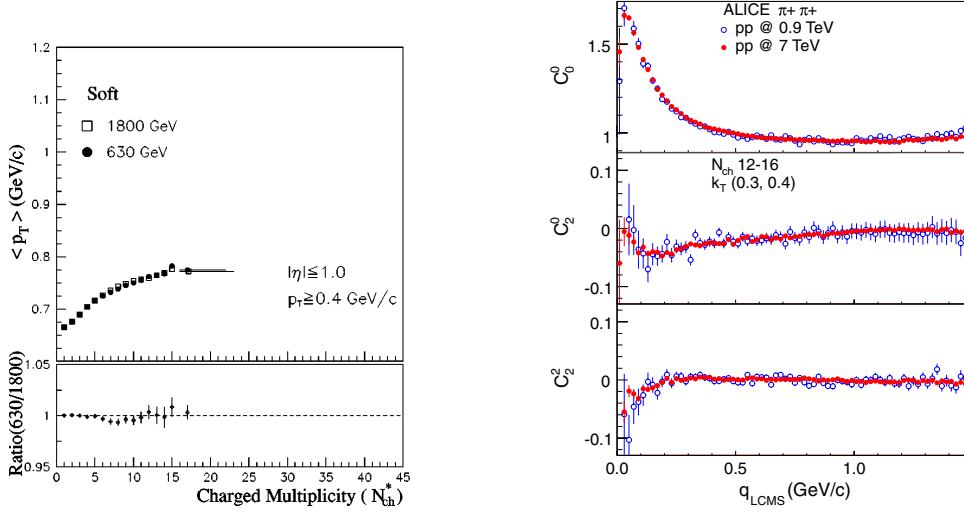


Figure 3.15: CDF: $\langle p_T \rangle$ at 630 GeV and 1800 GeV as a function of N_{ch} [33].

Figure 3.16: ALICE: two-pion correlation studies at 0.9 TeV and 7 TeV [34].

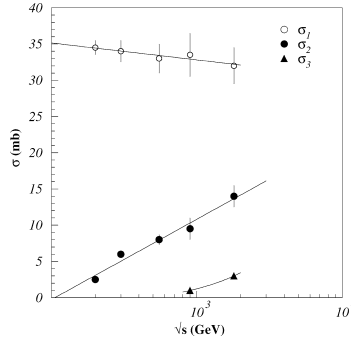


Figure 3.17: Double and triple partonic interactions as a function of $\ln(s)$ [10].

such processes contribute to a large energy transfer in the collision volume of proton size which could be very well thermalized if we consider the mean free path of 0.2 – 0.3 fm derived from QGP viscosity and that two - three collisions are in principle sufficient for thermalization.

Therefore is quite probable that at such energies, a piece of matter of proton size, with a radius a few times larger (2.5 - 4.5) than the mean free path, hydrodynamically explodes if enough energy is produced inside.

In order to evidence such phenomena, a detailed analysis of identified charged hadrons transverse momentum distributions as a function of the hadron mass, for high multiplicity and close to azimuthal isotropy events, is necessary.

Chapter 4

The ALICE Experiment

4.1 Large Hadron Collider (LHC)

The LHC synchrotron is the last stage of a chain of accelerators, operating at CERN, that are able to accelerate protons up to a nominal total energy of 14 TeV. The protons obtained by ionizing hydrogen atoms are injected into the Linac 2 linear accelerator at the end of which they reach a energy of 50 MeV. The next stage is represented by the Proton Synchrotron Booster and the Proton Synchrotron which together accelerate the protons to 25 GeV. Before being injected in the LHC the protons are accelerated up to 450 GeV by the Super Proton Synchrotron. Inside the beam pipes of the LHC the two beams are circulated clockwise and anticlockwise for several minutes before reaching the maximum energy. After that, the beams are collided at four interaction points that are located inside the four main detectors: ALICE, ATLAS, CMS and LHCb (Fig. 4.1) [35].

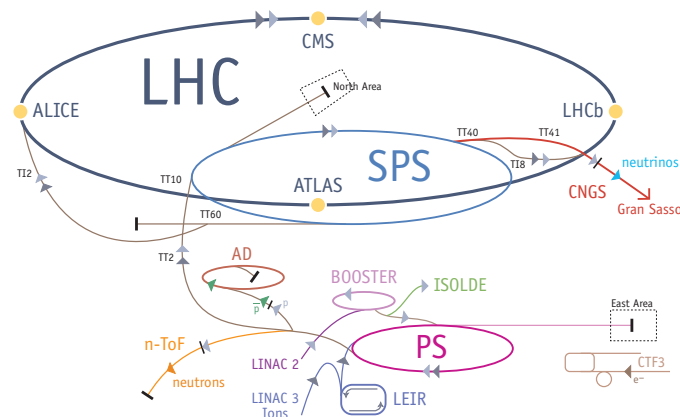


Figure 4.1: The CERN accelerator chain complex [36].

In the following table the accelerator parameters from 2010, when the data sample used in this analysis was produced, are summarized and compared

with the nominal parameters.

	2010	Nominal
Energy [TeV]	3.5	7
β^* [m]	3.5, 3.5, 3.5, 3.5	0.55, 10, 0.55, 10
Emittance [μm]	2.0 - 3.5 start of fill	3.75
Transverse beam size at IP [μm]	~ 60	16.7
Bunch current	$1.2 \cdot 10^{11}$	$1.15 \cdot 10^{11}$
Number of bunches	368	2808
	348 collisions/IP	
Stored energy [MJ]	28	360
Peak luminosity [$\text{cm}^{-2}\text{s}^{-1}$]	$2 \cdot 10^{32}$	$1 \cdot 10^{34}$

Table 4.1: LHC parameters in 2010 [37].

4.2 A Large Ion-Collider Experiment (ALICE)

The main detectors of the highly complex ALICE experiment (Fig. 4.2) are the *Inner Tracking System* (ITS), the large *Time Projection Chamber* (TPC), the *Transition Radiation Detector* (TRD) and a *Time of Flight* detector (TOF). These form the so called *Central Barrel* that covers a pseudorapidity range of -0.9 to 0.9 and the full azimuthal angle and allows the reconstruction of tracks and also provides information that is used for the *Particle Identification* (PID).

The Central Barrel detectors are placed inside a massive solenoidal magnet that is able to generate a homogeneous magnetic field of 0.5 T. Also inside the main magnet there are two smaller area detectors: the *High-Momentum Particle Identification Detector* (HMPID) and the *PHOTon Spectrometer* (PHOS).

A *Muon Spectrometer*, a *Photon Multiplicity Detector* (PMD) and a *Forward Multiplicity Detector* (FMD) are located at large rapidities. The experimental setup is completed by two fast trigger detectors *TO* and *VO* and a detector that allows the measurement of the impact parameter i.e. the *Zero Degree Calorimeter* (ZDC) [38].

All the observables used in the present analysis were determined using the detectors of the Central Barrel.

4.2.1 Inner Tracking System (ITS)

The ITS [39] is positioned right next to the beam axis and, therefore it has to cope with a very high particle density which can reach 80 particles per cm^2 , for the inner most layer. It is positioned between the outer radius of

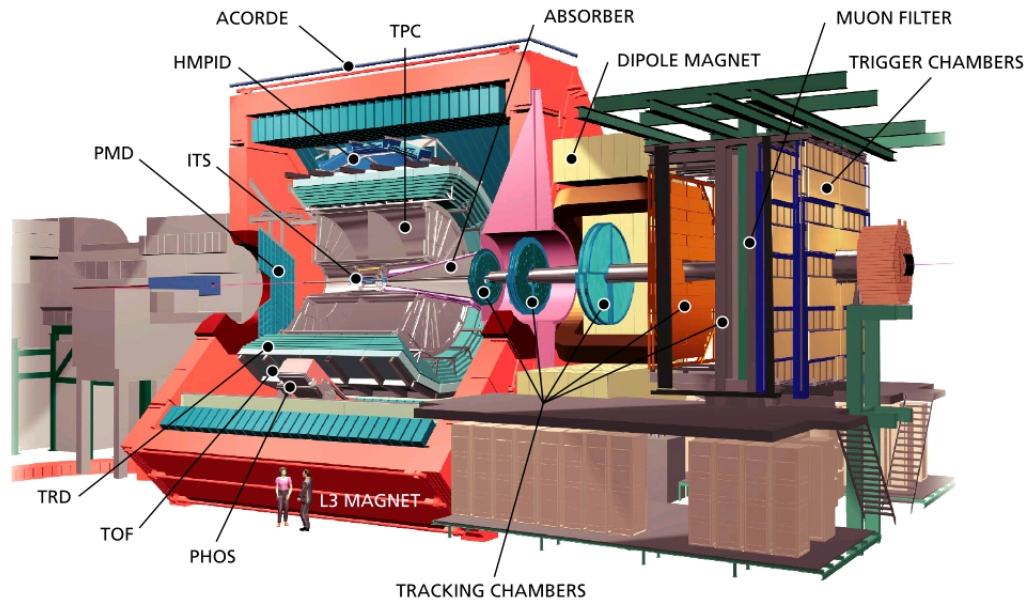


Figure 4.2: The ALICE experiment [38].

the beam pipe (3 cm) and the inner radius of the Time-Projection Chamber (TPC).

The main goals of the ITS are: i) the reconstruction of the main vertex with a resolution better than $10 \mu\text{m}$, ii) tracking and identification of the particles with a momentum below 100 MeV and iii) contribution to the ALICE global tracking by improving the momentum and angle resolution of the TPC.

In order to fulfill this goals while operating within the constraints already described, a design with six concentric layers of silicon detectors was selected (Fig. 4.3).

The first two layers, positioned at 4 and 7 cm from the center of the beam pipe are made from pixel detectors and are followed by another 2 layers (at 15 and 24 cm) of silicon drift detectors. The last two layers, positioned at 39 and 44 cm are equipped with double-sided silicon strip detectors.

This design makes it possible for the ITS to cover a pseudorapidity range of $|\eta| < 0.9$ for all the vertices that are located within a ± 10.6 cm range, on the z -axis, relative to the center of the barrel. Because the full coverage of the ITS is achieved for events with vertices in this ± 10.6 cm range, in the analysis a cut in the position of the main vertex of ± 10 cm was used for all the considered events, as it will be described in Section 5.1.

The last four layers of the ITS have analog readout which make it possible to perform standalone particle identification using the dE/dx measurement.

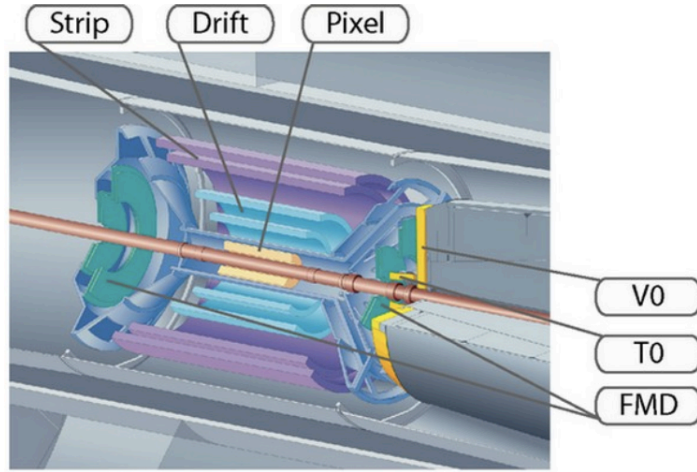


Figure 4.3: The Inner Tracking System [40].

4.2.2 Time-Projection Chamber (TPC)

After the ITS, the next concentric detector of the ALICE Central Barrel is the TPC [41].

The main difficulty which is faced by the TPC comes from the central Pb-Pb collisions where a very high multiplicity event could generate up to 20000 charged tracks within the detector acceptance.

In this conditions the TPC has to provide, with full azimuthal coverage, high resolution charged particles momentum measurements, vertex determination and particle identification for all the tracks in a $|\eta| < 0.9$ pseudorapidity range. The momentum resolution achieved by the TPC for the tracks that have a momentum between 0.1 and 1 GeV/c is 1-2%. By using the TPC in combination with the ITS and the Transition Radiation Detector (TRD) a momentum resolution of 10% is obtained for tracks with a momentum up to 100 GeV/c. Particle identification is possible in the TPC, at low momenta, using the dE/dx measurement where the expected ionization for different particle types is well separated. To achieve these goals the TPC has a massive cylindrical layout with a inner radius of 85 cm and a outer radius of 2.5 m, the length along the beam direction being 5.0 m (Fig. 4.4). A massive field cage filled with a Ne - CO₂ gas mixture transports the electrons resulted from the initial ionizations over a maximum distance of 2.5 m. This is the distance between the central electrode and the end-plates into which the multiwire, cathode pad readout, proportional chambers are mounted.

4.2.3 Transition Radiation Detector (TRD)

The TRD [42] represents the next layer of detectors of the ALICE Central Barrel and it is positioned between the TPC and the Time Of Flight detec-

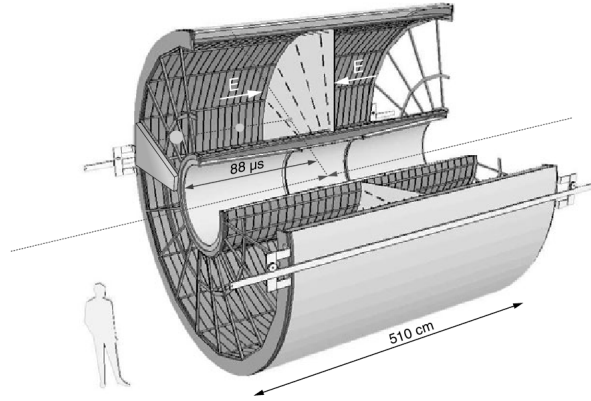


Figure 4.4: Time Projection Chamber [38].

tors. Its main goals are to identify the electrons with a momentum above 1 GeV/c, where the separation between electrons and pions in the TPC's dE/dx measurement is no longer sufficient for identification, and to provide momentum measurements with a resolution of 5% at 5 GeV/c, which allows it, as already mentioned, to contribute to the global momentum measurements along with the ITS and the TPC. In addition to this, because of its fast tracking abilities it can be used as trigger for high momentum electrons. The TRD has 6 individual layers and it is segmented along the azimuthal direction into 18 sectors (Fig. 4.5). Each individual TRD chamber consists of a radiator, in which the emission of the transition radiation takes place, and a proportional multiwire chamber.

It is important to note that, for the present analysis which uses proton-proton collisions data gathered during the 2010 LHC run, at that time the TRD was not fully installed. As it can be seen in Fig.4.6 only 7 out of the 18 TRD sectors (the yellow trapezoids) were present in the experiment. The effect of the presence of TRD modules in front of the time of flight (TOF) was studied as part of the estimation of systematic errors, by comparing the fully corrected p_T spectra of the tracks that cross the TRD with the fully corrected spectra of the tracks that do not encounter the TRD in their path (see Section 8.2).

4.2.4 Time Of Flight (TOF)

The main detector used for particle identification in this analysis is the TOF [44]. It was designed to cover a pseudorapidity range of almost $|\eta| < 0.9$ and to provide identification for particles with a momentum between 0.2 and 2.5 GeV. The signal generated by a particle in the TOF represents also the final point of the track that is associated with that particle.

It consists of a cylindrical surface with an internal radius of 3.7 m and, similar with the TRD and the readout chambers of the TPC, it is divided into 18

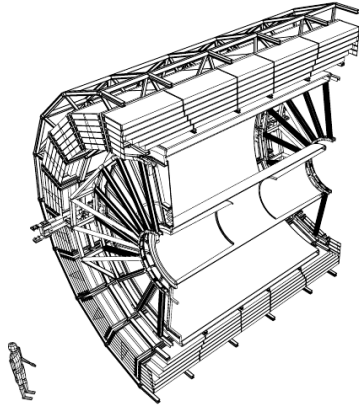


Figure 4.5: Longitudinal cross-section of the TRD [38].

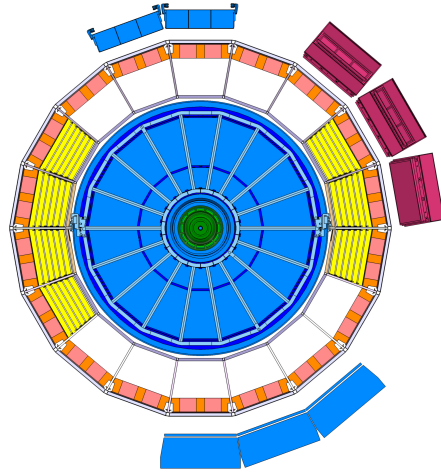


Figure 4.6: Cross-section of the ALICE experiment during the 2010 data taking period [43].

sectors (Fig. 4.7).



Figure 4.7: Schematic view of a TOF sector [38].

The technical solution selected for this detector was based on Multi-gap Resistive-Plate Chambers which, being gas detectors, are able to cover the large active area. In addition, due to the high and uniform electric field of the detector the avalanche process generated by a ionization will start immediately with no associated drift time. With this design a intrinsic resolution of 80 ps is achieved.

4.2.5 T0

The main roles of the T0 [45] detector are to provide a start time (with a precision of 50 ps) for the time of flight measurement performed by the TOF and to measure roughly the position of the vertex in order to generate a L0 trigger signal. Because of the fact that it generates the earliest L0 trigger signal this signals are completely generated online and the dead time of the

detector is less than 25 ns.

The T0 consist of two arrays of Cherenkov counters which are place at 70 cm, covering a pseudorapidity range $2.9 < \eta < 3.3$ and at 3.5 m, covering a pseudorapidity range $-5 < \eta < -4.5$, respectively.

4.2.6 V0

The V0 [45] detector generates a minimum bias trigger signal for the central barrel.

Due to its capability to provide time of flight measurements in addition to charge signals it can be used to eliminate beam-gas interactions which are an important source of background especially in the case of proton-proton collisions.

Its layout is rather similar with the one of the T0 detector: there are 2 arrays of four concentric rings of plastic scintillators, located at 90 cm and 3.4 m, respectively.

4.3 ALICE Computing framework

In the cases of such highly complex experimental devices, the integrated software environment that is used for the Monte-Carlo simulations, the reconstruction of the experimental information and the analysis of the resulted data, reaches a complexity similar with that of the experimental device itself. The performance of this software environment is, therefore, a critical factor which determines the quality and reliability of the data analysis results.

In todays high energy physics experiments the software framework has to cope with a wide range of demands. The Monte-Carlo simulations of the studied phenomena provide the means to account in the final results for the detector limitations and to estimate the related systematic errors, as described in Chapters 7 and 8. Also, much earlier, in the development phase of the experimental device, such simulations provide very important estimations with high impact on the chosen technological solution. The reconstruction of the recorded experimental events i.e. the extraction of the physical observables from the various signals generated by the detectors is also a highly complex task which has to be handled by the computing environment. The analysis of the resulted experimental data is done usually using elaborated algorithms and uses a high amount of processing power as well as data storage volume.

As the ALICE computing environment, the AliRoot [46], is used for extremely diverse and complex tasks, large portions of the code are developed by experts thus making them a very valuable resource, therefore, the possibility of reusing the code and the possibility of developing portions of code with minimum interference with other users are extremely important.

This goals were achieved by developing AliRoot based on the CERN de-

veloped ROOT framework [47], which offers an extensive, object-oriented layered hierarchy of classes.

“ROOT is written in C++ and offers, among other features, integrated I/O with class schema evolution, an efficient hierarchical object store with a complete set of object containers, C++ as a scripting language and a C++ interpreter, advanced statistical analysis tools (multidimensional histogramming, several commonly used mathematical functions, random number generators, multi-parametric fit, minimization procedures, cluster finding algorithms etc), hyperized documentation tools and advanced visualization tools” [38].

In addition to this, the ROOT framework was interfaced with the ALICE distributed computing environment (AliEn [48]). The use of distributed computing (the GRID) is the only way in which a LHC era experiment can gather the processing power and the storage capacity which is needed for simulations, reconstruction and data analysis. The GRID is a global network of data centers, maintained and financed by local research institutions, operating in a hierarchical structure and being connected via the existing internet network.

The AliEn middleware handles the migration of the experimental or simulated data to the designated data centers and the management of the available processing power. It also plays a huge role in end-user’s analysis (the so called “chaotic” analysis) by transparently assigning and running the analysis tasks on the relevant data centers i.e. the ones storing the requested data, in order to minimize the transfer of data over the network.

The GRID site of the Hadron Physics Department was, in the last six years, constantly among the most performant ones in the ALICE GRID. In terms of done jobs, a job representing the Monte-Carlo simulation of an event, the reconstruction of a data event or the execution of a user analysis task, the NIHAM (Nuclear Interactions and HAdronic Matter) was in the first three ALICE GRID sites until July 2012 (Fig. 4.8). Then, despite a long shutdown period of about 6 months, used for the complete upgrade of the data center, the NIHAM GRID site is still in the first five ALICE GRID centers, having a performance comparable to the Tier-1 centers.

The computing power of the data center consists of 2000 CPU cores. As described above, the reconstruction codes and the users analysis task are assigned to the GRID sites that store the relevant data. A very reliable 2 PB of storage capacity is also installed in the NIHAM data center (Fig. 4.9). In addition to the very robust software setup, a set on industrial grade UPSs and a diesel power generator ensures a very high (above 96%) availability of the site. For code developing, tests and large scale model calculations a dedicated significant computing facility (NAF - NIHAM Analysis Facility) was recently installed and presently running.

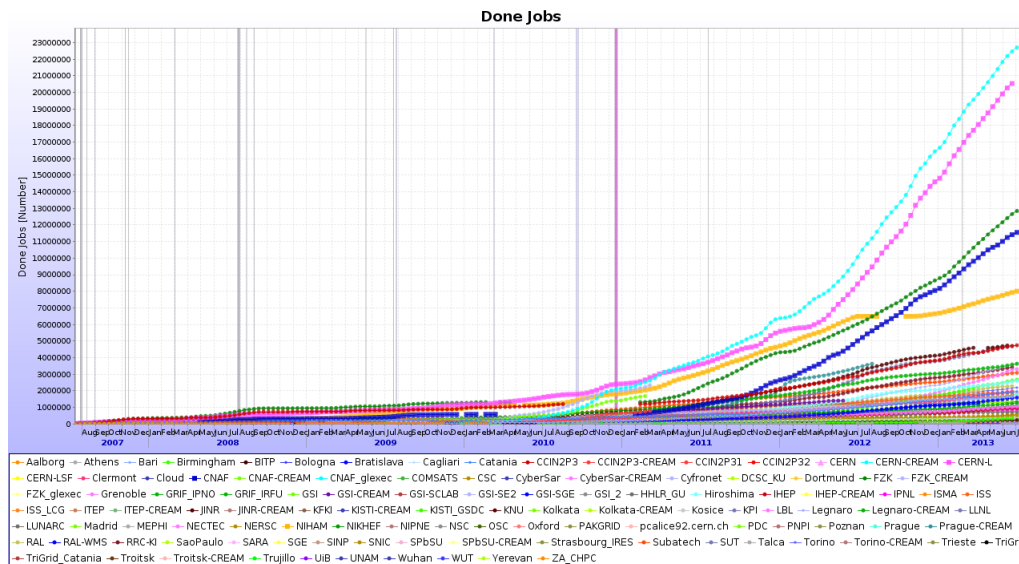


Figure 4.8: The performance in terms of done jobs for the ALICE GRID sites starting with August 2007; NIHAM is represented by the dark yellow curve [49].

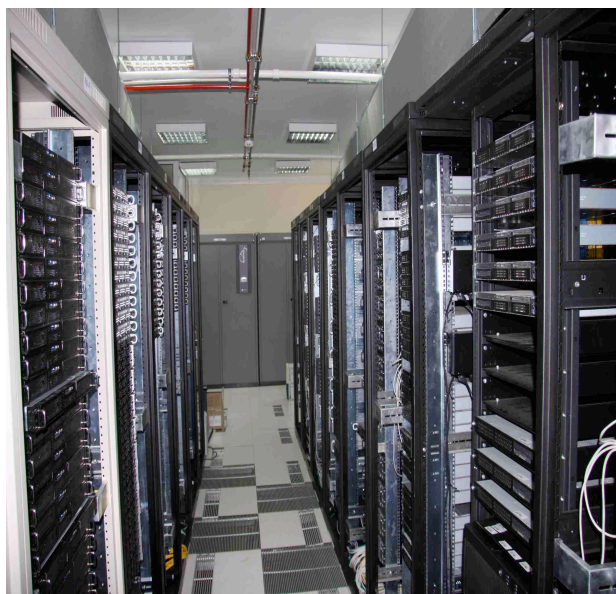


Figure 4.9: Photo of the NIHAM GRID site data center.

Chapter 5

Event and Track Selection

5.1 Event selection

The quality of the analyzed events is, obviously, a critical issue that could have an important impact on the final results of the analysis. Therefore, special attention was given to the selection of data runs that were analyzed and to the trigger conditions.

Online, the *Minimum Bias trigger* (MB) is based on the V0 detector and it requires a signal in either of its arrays or at least one hit in either of the two internal layers of the ITS. This online trigger setup is optimized for high efficiency and, in the same time, it has the task to reject beam-gas and beam-pipe interactions.

Offline, a more complex software procedure (*PhysicsSelection*) is used in order to select the events using, in addition, the timing information of the V0. This selection is done by applying several conditions on the considered events: has the correct event type; has the interaction trigger; fulfills the online trigger condition (recomputed offline); is not flagged as beam-gas by the V0 detector (recomputed offline); is not flagged as beam-gas based on the ITS clusters vs tracklets (association of clusters in the two silicon pixel detector planes) correlation [50, 51].

The *pile-up events* (superposition of independent p+p collisions with $\Delta\tau_{pileUp} < 100$ ns) must be eliminated as they could mimic a high multiplicity event and at the same time mix a whole range of phenomena, which could result in a bias of the final results. A two steps approach is used in order to achieve this: (i) only data runs with a small estimated average number of collisions per bunch crossing ($\mu < 0.079$) were selected; (ii) an offline software method that uses the SPD sub-detector to identify pile-up vertices is applied within the analysis task.

A very important test of the influence of pile-up events on the analysis results was done by removing the pile-up rejection from the analysis task and comparing the fully corrected p_T spectra for the two cases. It has to be noted that for the analyzed data sample, in this work, the pileup rejection procedure removed only 0.91% of the total number of events for the MB

trigger events and 8.9% for the HM trigger events. In Fig. 5.1 the ratio of the spectra obtained with the pileup rejection procedure to the spectra obtained without that procedure is plotted for the MB case and for the first six multiplicity bins (up to multiplicity between 40 and 49). As it can be seen in the figure, for all the species and all the multiplicity bins, the differences are below $\pm 1\%$.

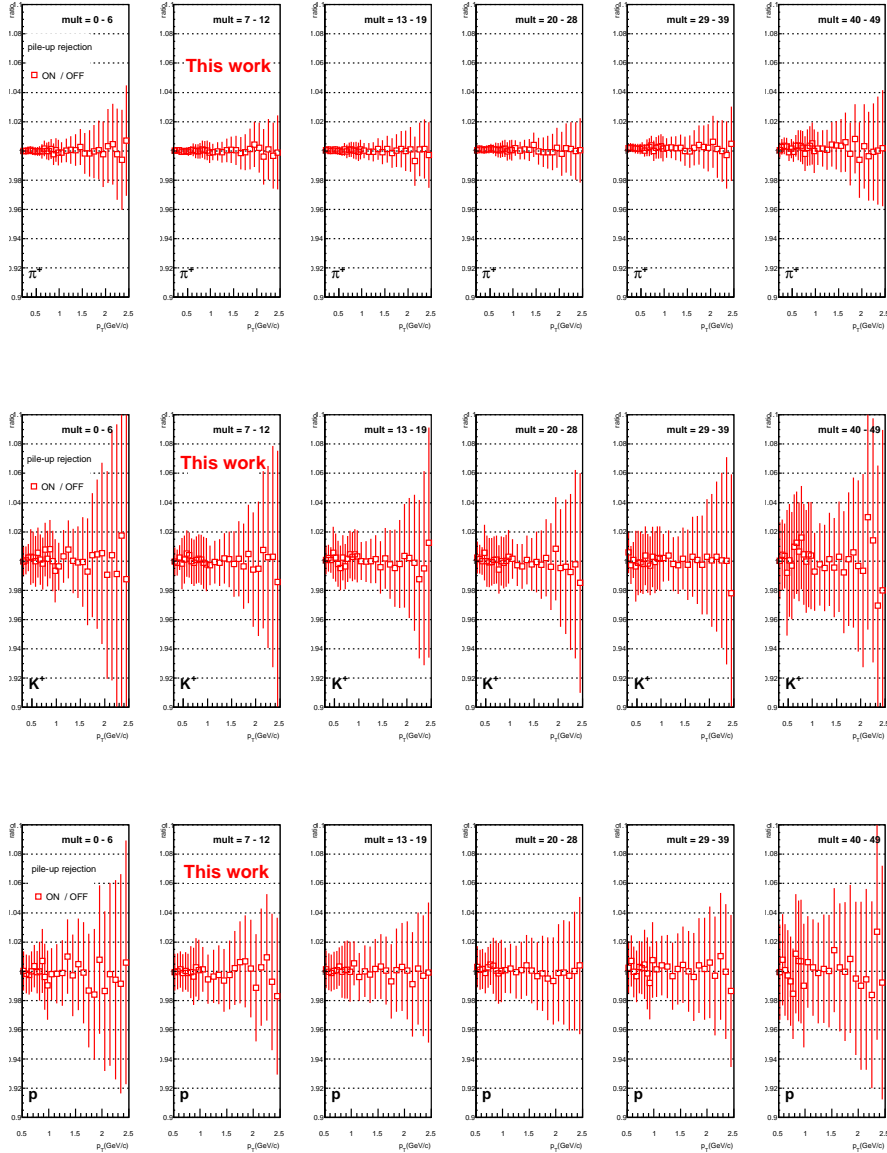


Figure 5.1: Ratio of the fully corrected p_T obtained with and without the pileup rejection procedure for pions, kaons and protons.

This check was also done using the HM trigger and, for the highest multiplicity bin (72 - 82), the ratio was fitted with a zero degree polynomial function in order to eliminate the statistical fluctuations. The results of that

fit are summarized below, and as it can be seen there is no systematic effect produced by the pileup.

- pions: 1.005 ± 0.006
- kaons: 0.995 ± 0.021
- protons: 1.004 ± 0.025

In addition to this, for events with the multiplicity between 50 and 59 (the last bin with reasonable statistics), using the HM trigger, the fully corrected spectra was obtained using the run with $\mu = 0.04$ (130179) which is the lowest μ in the analyzed data sample and the run with $\mu = 0.079$ which is almost two times greater and it is the highest μ in the analyzed data sample. The ratio of the fully corrected spectra was plotted and then it was fitted with a zero degree polynomial function as described above, the results being again very good:

- pions: 0.996 ± 0.008 with $\chi^2/NDF = 0.94$
- kaons: 0.972 ± 0.027 with $\chi^2/NDF = 1.06$
- protons: 0.969 ± 0.031 with $\chi^2/NDF = 0.95$

This result, computed for the worst case scenario i.e. the difference between the two extreme runs in terms of μ values, confirms that pileup is too low to introduce any bias for this data sample.

For each of the analyzed events the existence of a *reconstructed main vertex* is, obviously, a mandatory condition.

The position of the main vertex is determined, in a first approximation, by using, as in the case of the trigger, the two innermost layers of the ITS. The vertex finding algorithm [52] considers the z coordinates of the reconstructed space points in the first layer of the ITS. For a vertex position that is not further than about 12 cm from the center of the barrel, the distribution of the z coordinates is symmetric and its centroid is a good estimation of the true vertex position. This ITS based vertex is used, in the analysis, as a fall back solution in the case of the events for which the vertex is not reconstructed, with a higher resolution, by using complete tracks, as described below.

The approximate ITS based estimation for the position of the main vertex is used primarily as a starting point for the tracking algorithm described in Section 5.3. However, only by using fully reconstructed tracks the position of the main vertex can be estimated with enough resolution for physics studies like the reconstruction of D and B mesons. For this, “each track, reconstructed in the TPC and in the ITS, is approximated with a straight line at the position of the closest approach to the nominal primary vertex position (the nominal vertex position is supposed to be known with a precision of 100-200 μm). Then, all possible track pairs are considered and for each pair, the centre of the segment of minimum approach between the two lines is

found. Finally, the position of the vertex is reconstructed minimizing the χ^2 function” [53, 54].

This high resolution position of the vertex was considered in the present analysis for the selection of events. In order to avoid any bias in the determination of the main vertex as well as to have the full coverage of the ITS available, in the present analysis, only events which have a main vertex in the range of ± 10 cm in the z direction were considered.

5.2 Multiplicity distribution

As this study focuses on the behavior of the p_T spectra as a function of multiplicity and event-shape, the considered multiplicity estimator and its influence on the studied observables were carefully evaluated.

The number of global tracks with $|\eta| < 0.8$ is a straight forward information that can be used in order to obtain a multiplicity estimation and it was, historically, the first option for this analysis. However, a detailed analysis of the behavior of the corrections as a function of multiplicity revealed that, using this estimator, the tracking efficiency (see chapter 7) is different for events in different multiplicity bins. More than that, counterintuitively, the tracking efficiency was increasing as a function of multiplicity, showing that this effect was not generated by a detector limitation. Reaching a detector limitation in p+p events was not possible anyway due to the fact that the ALICE experiment was designed to cope with very high multiplicity Pb+Pb events. This bias that affected the tracking efficiency can be explained by the fact that the correlation between the reconstructed global tracks multiplicity and the generated one, obtained based on the same PYTHIA simulations that are used in order to estimate the corrections for the particle spectra, is broad and far from the first diagonal (Fig. 5.2). This results in a bias because, when selecting events with a high reconstructed multiplicity, one favors events with a higher tracking efficiency.

Within the ALICE collaboration, extensive studies found that multiplicity estimators with a far better performance can be defined [55]. One example is the combined multiplicity estimator (Fig. 5.3).

In this case the multiplicity is obtained by summing the global tracks within the event with the complementary ITS standalone tracks and the complementary SPD tracklets (Fig. 5.4).

As it can be seen by comparing Fig. 5.2 and 5.3 this estimator has a much better performance than the global tracks estimator, the multiplicity generated in Monte-Carlo simulations being reconstructed with a better accuracy. In this way the bias in the tracking efficiency is eliminated.

The combined multiplicity estimator was used in this analysis and indeed, as it is described in Chapter 7 the corrections have no dependence on the multiplicity.

The multiplicity bins in which the p_T spectra were obtained and the cor-

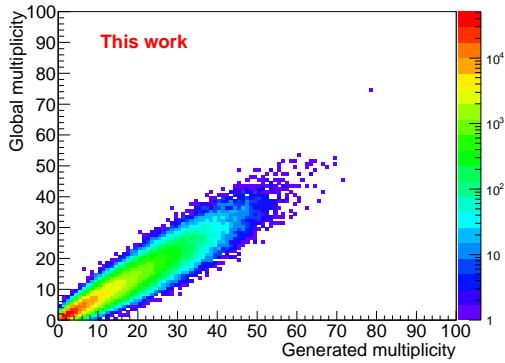


Figure 5.2: Reconstructed global multiplicity vs generated multiplicity.

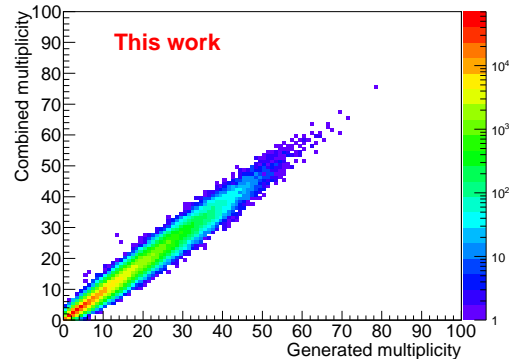


Figure 5.3: Reconstructed combined multiplicity vs generated multiplicity.

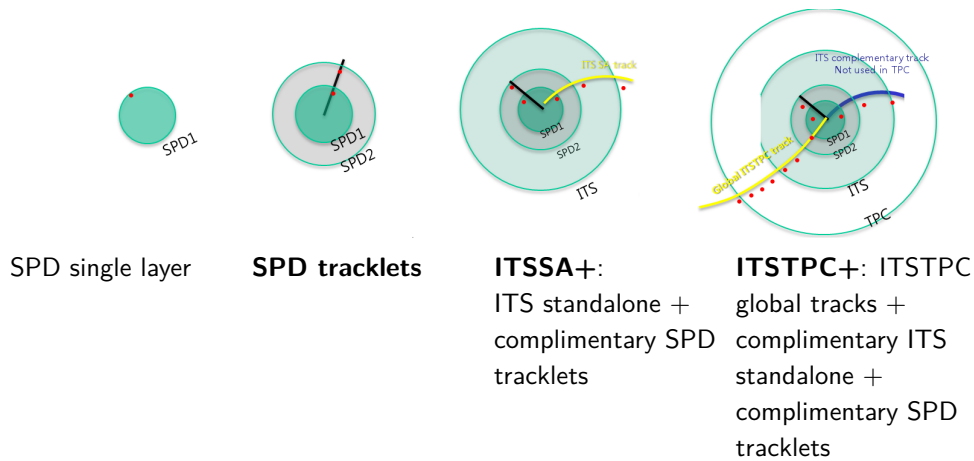


Figure 5.4: Combined multiplicity estimator definition: labeled as “IT-STPC+” in this figure [56].

correspondence between the global tracks multiplicity bins and the combined multiplicity bins can be seen in Table 5.1. This correspondence was obtained using the same method that is described below for the correspondence between the combined multiplicity bins and the CMS generated multiplicity. The result of this correspondence is also included in Table 5.1.

The correspondence is obtained using a two-dimensional representation of the correlation of the global multiplicity with the PYTHIA based Monte-Carlo generated multiplicity within the CMS acceptance of $|\eta| < 2.4$ (Fig.5.5). The maximum of that correlation is obtained (black line in Fig.5.5) and, using this approximation, the combined multiplicity bin limits (red lines in the same figure) are translated in CMS generated multiplicity bin limits.

This estimation can be used to compare the final results of this analysis with similar results obtained by the CMS experiment, comparison which is pre-

Global $ \eta < 0.8$	Combined $ \eta < 0.8$	CMS $ \eta < 2.4$ (PYTHIA)
0 - 5	0 - 6	0 - 18
6 - 9	7 - 12	19 - 35
10 - 14	13 - 19	36 - 55
15 - 22	20 - 28	56 - 81
23 - 31	29 - 39	82 - 113
32 - 39	40 - 49	114 - 142
40 - 49	50 - 59	143 - 170
50 - 62	60 - 71	-
63 - 72	72 - 82	-

Table 5.1: Multiplicity bins correspondence: global tracks - combined multiplicity - generated CMS.

sented in Chapter 9.

In addition to this, using the same method that was described above, the correlation between the combined multiplicity bins and the multiplicity generated in PYTHIA based Monte-Carlo simulations was estimated and the results are shown in Table 5.2.

Combined	Generated (PYTHIA)		
	bin limits	Mean	Sigma
0 - 6	0 - 6	3.4	1.7
7 - 12	7 - 12	9.1	2.2
13 - 19	13 - 20	15.9	2.6
20 - 28	21 - 29	23.7	3.2
29 - 39	30 - 41	33.2	3.7
40 - 49	42 - 51	44.1	3.7
50 - 59	52 - 62	-	-
60 - 71	63 - 74	-	-
72 - 82	75 - 86	-	-

Table 5.2: Multiplicity bins correspondence: combined multiplicity - generated PYTHIA multiplicity.

This correlation is presented in terms of bin limits in column two. Then, in the next two columns, the mean and the sigma of the generated multiplicity distribution that is obtained when considering events within a certain combined multiplicity bin are also estimated. For the last three high multiplicity bins, because of the low available Monte-Carlo statistics, the above mentioned distribution was not well determined and therefore the corresponding values are not included in the table.

As it can be seen, the bin limits in the combined multiplicity and the ones in

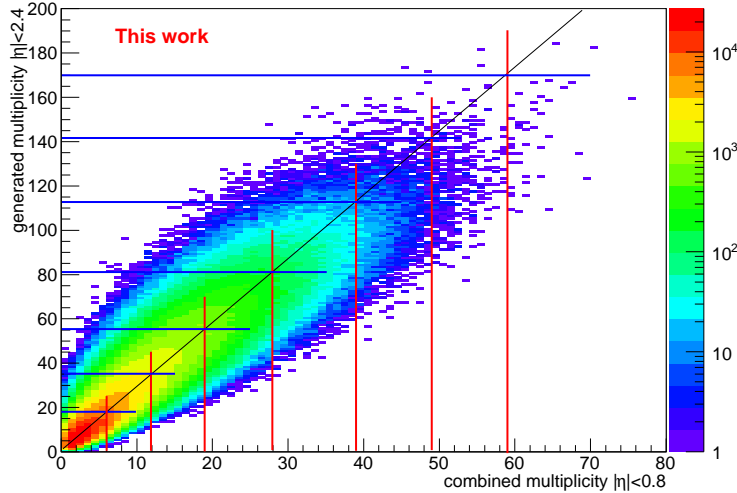


Figure 5.5: The method used to determine the correspondence of bin limits between the combined multiplicity estimator ($|\eta| < 0.8$) and the generated multiplicity in the CMS acceptance ($|\eta| < 2.4$).

the generated multiplicities are very similar, as they should be given the very good performance of the combined multiplicity estimator (Fig. 5.3).

This correlation is useful for comparing the results of this analysis with theoretical model predictions, also included in Chapter 9.

The LHC10e data period, that was used in this analysis, has a very important feature that made it the best candidate for analyzing high multiplicity events. For this period, in addition to the MB trigger, a *high multiplicity* hardware trigger (HM) was used during the data taking. As it can be seen in Fig. 5.6 the use of this HM trigger dramatically increases the available statistics at high multiplicities. In order to check for any bias that could appear at high multiplicities when this trigger is used, the ratio of the combined multiplicity distributions for the MB and the HM trigger was constructed (right side of Fig. 5.6). This shows that the ratio of the two distributions becomes flat for multiplicities above 50. Therefore, in this analysis, whenever the HM trigger events were analyzed, a cut in the minimum event multiplicity of 50 was applied.

5.3 Track selection

In addition to the event level selection, the tracks considered in the analysis must also pass several criteria in order to be accepted.

The ALICE detector was designed to provide reconstruction capabilities for tracks down to very low p_T values (about 0.1 GeV/c), while maintaining a high efficiency and a high resolution.

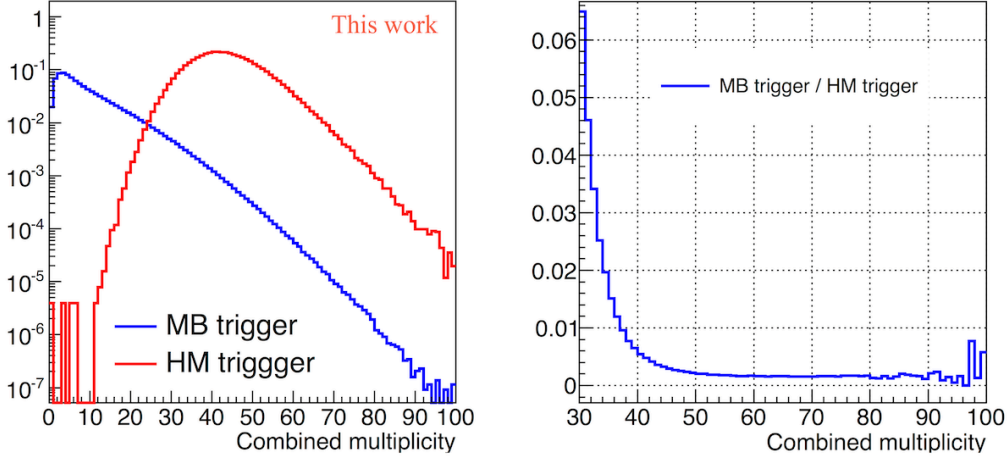


Figure 5.6: The comparison of the MB trigger and of the HM trigger combined multiplicity distributions.

There are several difficulties that the tracking algorithm has to cope with in the ALICE detector. The two main ones are represented by the significant material budget of the ITS and the TRD, which creates non-negligible energy losses and multiple scatterings, and by the significant dead zones between the tracking detectors. In these conditions the best choice for the tracking algorithm is the Kalman-filtering approach [57].

The first step of the tracking procedure is finding the clusters in the ITS, TPC, TRD, TOF, HMPID and PHOS detectors. As already mentioned, the clusters in the first two layers of the ITS are used for a low resolution estimation of the main vertex and this position is used for the track reconstruction. In order to have the tracks well separated at the start, this position is chosen to be the outer radius of the TPC which is the best tracking detector.

The second step is the assigning of a small number of clusters to a track candidate. This low precision track candidate is then propagated towards smaller TPC radii and new clusters are assigned to it, using the Kalman-filter procedure, thus improving the track precision.

After all the track candidates were successfully propagated to the inner limit of the TPC, the ITS tracking starts. In the ITS these tracks are propagated towards the main vertex on the way collecting more ITS clusters, the track parameters becoming more and more precise.

When this stage is complete, a new tracking procedure is started, this time using only the ITS information. In this way the ITS tracks that did not reach the TPC, because various reasons such as TPC dead zones, decays or low p_T cut-off, can still be reconstructed.

Next, the tracking procedure restarts from the main vertex position towards the outer limit of the TPC. At this point the precision of the track param-

eters is good enough to allow the extrapolation of the tracks to the outer detectors (TRD, TOF, HMPID and PHOS).

The final step is to refit, using the Kalman-filter, from the outer-most position of the track back to the main vertex [53].

The tracks reconstructed in this way are selected using several quality cuts. First, the *quality of the track* is ensured by requesting at least 70 clusters in the TPC with a maximum χ^2 per cluster of 4. The *kink daughters* are rejected and a *successful refit of the trajectory* in both the TPC and the ITS is mandatory. At least a cluster in the SPD sub-detector is also requested and the maximum χ^2 per cluster for the ITS is set to 36. All tracks must have a *distance to closest approach* (DCA) to the main vertex, along the z-axis, of maximum 2 cm. A rapidity cut: $|y| < 0.5$ was also required.

As only the primary tracks (the ones that are generated by particles that are created in the initial collision) are of interest for the present analysis, they are selected by imposing a maximum *distance of closest approach* (DCA) to the main vertex in the x-y plane. This cut depends on p_T of the particle according to the following formula, which corresponds to 7 sigmas for pions:

$$DCA_{xy} \text{ cut} = 0.0182 + 0.0350/p_T^{1.01} \quad (5.1)$$

This cut is not able to eliminate all the secondary particles that are generated by the weak decays of the primary particles. Also, secondary particles that are generated by the interaction of the primary ones with the detector material have a probability of satisfying the DCA cut. An elaborated data driven procedure was developed in order to further eliminate this secondary particles (see Section 7.4).

In Table 5.3 all the event and track cuts used in the present analysis are summarized.

Condition	Value
main vertex	existence
main vertex position on the z axis	± 10 cm
clusters in the TPC	> 70
χ^2 in the TPC	< 4
kink daughters	reject
clusters in ITS inner layers	> 1
DCA in z coordinate	2 cm
DCA in x-y plane	$0.0182 + 0.0350/p_T^{1.01}$
mismatch probability (TOF only)	< 0.01

Table 5.3: Summary of the event and track cuts used in the present analysis.

Chapter 6

Particle Identification

The Particle Identification (PID) is the most delicate and complex part of this analysis. Unlike the other used observables such as the particle trajectory, momentum or charge which are unambiguously determined during the reconstruction phase, the determination of the mass of the particle requires the use of elaborated methods and extensive computations during the analysis.

Very soon after the first data were obtained by the ALICE collaboration in p+p collisions at $\sqrt{s} = 900$ GeV, the PID software being still in a development and tuning phase, the feasibility of this analysis was tested by developing a simple PID method. Sharp cuts were determined by looking at the velocity distribution in each p_T bin and determining the position of the minima between the lines of the pions, kaons and protons. These points were then fitted and the results are the red lines in Fig. 6.1, right side. Next, these lines were used as sharp cuts in order to separate the three species. In addition to that, in order to separate the electrons from the pions, another cut was applied, only for pions in the TPC dE/dx vs p_T distribution (red horizontal line in Fig. 6.1, left side) [58].

Since then the ALICE analysis framework (AliRoot) evolved very much in terms of performance and complexity.

The main PID signals that are used are the energy loss in the ITS and TPC (Fig. 6.2) and the time of flight measurement provided by the TOF (Fig. 6.4). The energy loss signal is based on the ionization phenomena that a charged particle produces in the detector. As it can be seen in Fig. 6.2 the kaon and pion bands are very well separated by the TPC up to a p_T of 0.6 GeV/c. The protons are easily distinguished from the pions up to 1.2 GeV/c.

The mean energy loss per path length ($\langle dE/dx \rangle$) can be related with the particle velocity (β) using the Bethe-Bloch formula:

$$\langle dE/dx \rangle = \frac{C_1}{\beta^2} (\ln(C_2 \beta^2 \gamma^2) - \beta^2 + C_3) \quad (6.1)$$

In this formula the three constants are specific to the considered detector. By correlating this information with the momentum, the mass of the respective

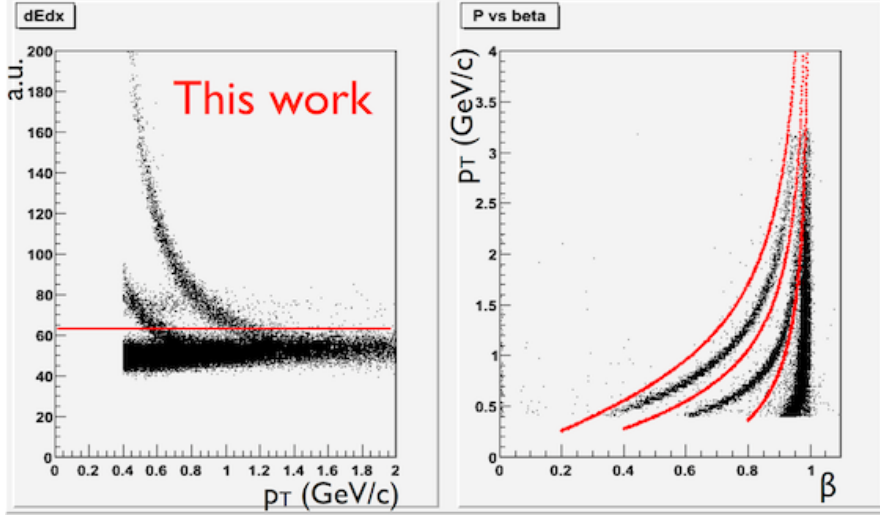


Figure 6.1: First PID method developed for testing the analysis feasibility.

particle can be determined [53, 59] .

The parametrization of this formula for electrons, pions, kaons and protons are represented in Fig. 6.2 by the black lines.

Using the Bethe-Bloch parametrization a straightforward n-sigma PID method can be implemented by defining n-sigma (with $n = 1, 2, 3, \dots$) bands, corresponding to each particle hypothesis, around these parametrizations and assigning an identity to particles if they are “located” inside these bands. Two versions of this method can be defined:

- The *exclusive 2-sigma*: a 2-sigma band is defined around the parametrizations and a particle is considered to be identified only if it is located within this band for a single identity hypothesis; if it satisfies this condition for more than one hypothesis then the respective particle is dropped. This method generates very low percentages of misidentified particles but it also has a low PID efficiency.
- The *inclusive 2-sigma* PID method is also based on the 2-sigma band defined around the above mentioned parametrizations but, this time, if a particle satisfies more than one hypothesis it is considered as having multiple identities. Obviously, this leads to very high PID efficiencies but also to high percentages of misidentified particles.

In this analysis these two PID methods were implemented and the obtained fully corrected p_T spectra were used as a crosscheck for the bayesian PID, described below, which was used for all the other results. The comparison of the three mentioned PID methods, restricted to the p_T range where the separation in the TPC dE/dx is large, can be seen in Fig 6.3.

The very good agreement that can be observed in the figure is a validation not only of the PID procedure but also of the corrections and normalization

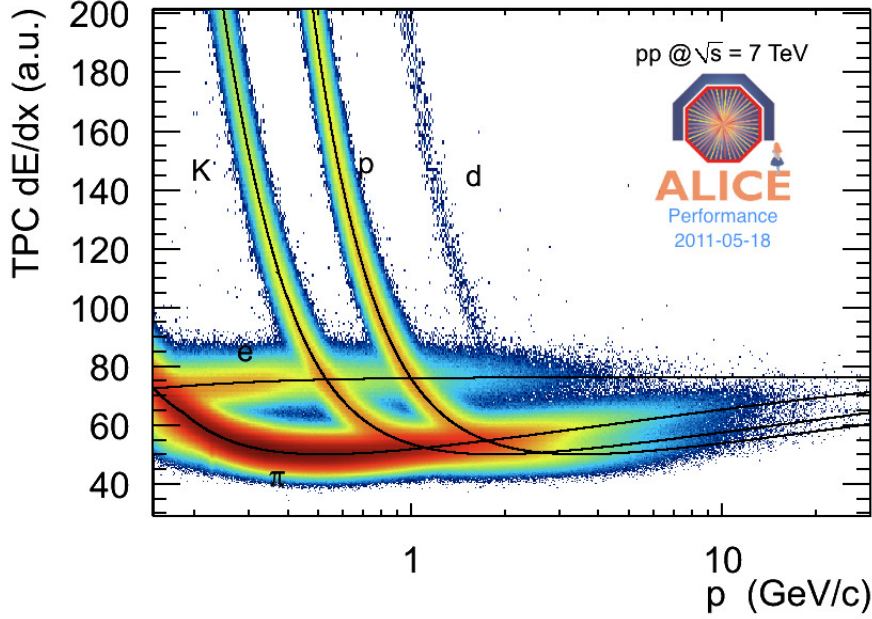


Figure 6.2: dE/dx spectrum versus momentum in p+p collisions at $\sqrt{s} = 7\text{TeV}$ using TPC. The lines are a parameterization of the Bethe-Bloch curves [43].

methods.

The time of flight measurement provided by the TOF is essential to this analysis due to the fact that it extends the p_T range on which reliable PID is possible.

The identification relies on the fact that knowing the p_T of the considered particle, the length of its trajectory and time interval in which the particle traveled from the vertex to the TOF hit, its mass can be easily determined using the following formula:

$$m = p \cdot \sqrt{\frac{t^2}{l^2} - 1} \quad (6.2)$$

The determination of the time interval can be done, obviously, only if, in addition to the time stamp of the TOF hit, a start time is available. This start time is common to all the particles of an event and it is represented by the time stamp of the collision. Normally the determination of the start time is done by the T0 detector, as described in Chapter 4.2, however during the 2010 data run this detector worked intermittently. Within the ALICE collaboration, the TOF reconstruction group developed a method to determine the start time of the event using the tracks that reach the TOF. This procedure assigns sequentially, to each track, every possible identity hypothesis and, with that hypothesis and the track length, it calculates a start time. For every combination of hypothesis for all the tracks within the event the χ^2 of

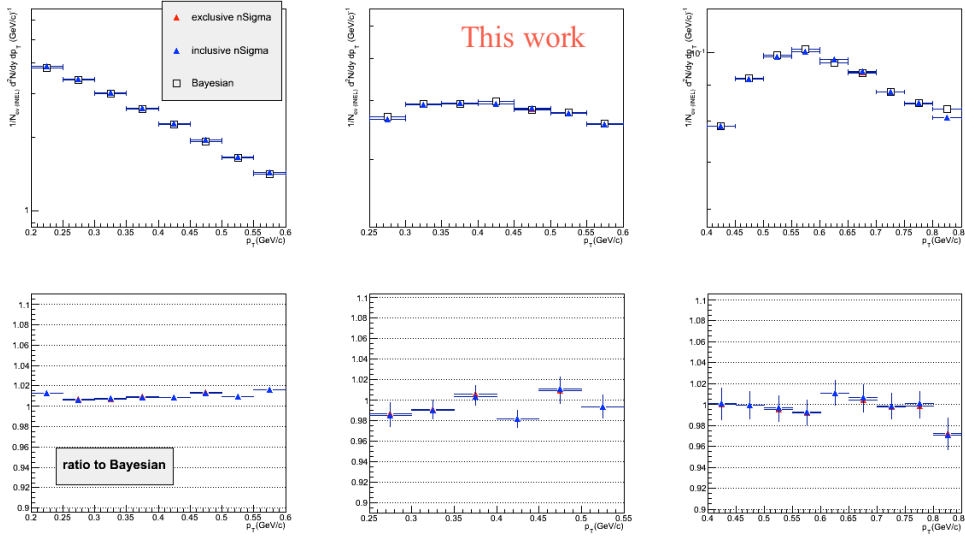


Figure 6.3: Comparison of 2-sigma inclusive and exclusive PID and the Bayesian PID.

the start time distribution is computed and the start time for that combination is assigned to the event [60]. Obviously the method works best for high multiplicity events where more tracks are available as an input for the procedure. For the high p_T kaons, which are, because of the high contamination from misidentified pions and protons, most sensitive to the PID method, this could result in a bias for the lowest multiplicity bin (see Fig. 7.15).

In the ALICE collaboration an integral PID method based on the time of flight measurement was used and the results of that analysis are compared with the ones from the present analysis, which is using the Bayesian PID, in Fig. 9.1. The integral method uses a fit with three gaussian, corresponding to the pions, kaons and protons, of the TOF determined velocity distribution relative to the theoretical one, in each p_T bin, in order to extract the particle yields.

As it was already mentioned, in the present analysis, a Bayesian approach was used for the PID. The Bayesian method produces probabilities for each identity hypothesis that depend not only on the detector response but also on the relative particles abundances. This dependence is described by the following formula:

$$w(i|s) = \frac{r(s|i)C_i}{\sum_{k=e,\pi,K,p} r(s|k)C_k} \quad (6.3)$$

where $w(i|s)$ is the probability to have a particle of type i if a signal s is obtained and $r(s|i)$ is the probability to obtain, in the considered detector, a PID signal s if a particle of type i is detected (further referred to detector response functions). The C_i factors are derived from the relative particles abundances and represent the *a priori* probabilities of finding a particle of

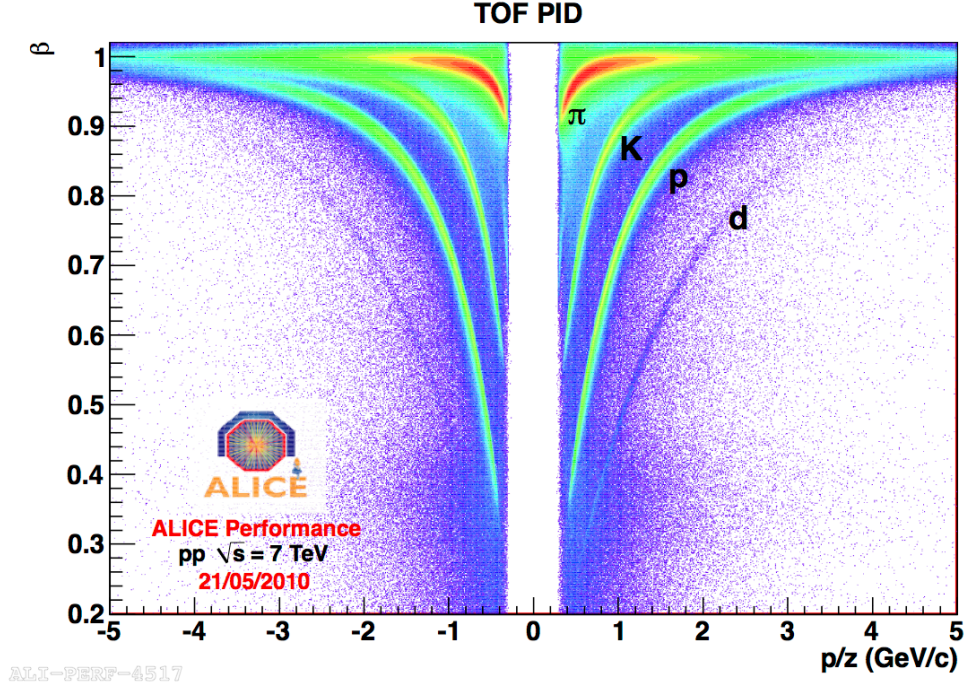


Figure 6.4: TOF measured particle beta vs. momentum measured by TPC in p+p collisions at $\sqrt{s} = 7$ TeV [43].

type i (further referred to as priors).

It can be considered as a very good approximation that the detector response functions depend only on the properties of the considered detector and that the priors depend only on the analysis details. The detector response functions are determined, during the reconstruction phase from the experimental data with no dependence on Monte-Carlo simulations.

The priors used in this analysis were obtained using an iterative method [61] that is described in Section 7.3. The stability of the Bayesian PID procedure to the change of the priors was studied as a part of the systematic errors estimation and the results are described in Section 8.3.

For this analysis the results of the Bayesian PID using separately the TPC and the TOF information, as well as the combination of the ITS and TPC response, were considered.

As describe above the TOF has a very good performance in terms of PID but it also has a low tracking efficiency at low p_T . In this low p_T region the separation between different species in the TPC is still very good. Based on these considerations and on the obtained PID efficiencies and contaminations from misidentified particles (see Section 7.3) the following ranges for the used PID response were established and used in the present analysis:

for pions: TPC based PID from 0.2 to 0.6 GeV; TOF based PID from 0.6 up to 2.5 GeV

for kaons: ITS-TPC based PID from 0.3 to 0.45 GeV; TOF based PID from 0.45 up to 2.5 GeV

for protons: TPC based PID from 0.5 to 0.8 GeV; TOF based PID from 0.8 up to 2.6 GeV

As described in Chapter 7 these regions of the p_T spectra, which are obtained using for PID different detectors, are just placed one next to the other with no factor or matching procedure.

Chapter 7

Corrections

In the previous chapters the procedure of obtaining the so called “raw” p_T spectra was described. It is obvious that the experimental information extracted in this way is biased by the detector performance and by the analysis procedure itself. In order to obtain meaningful results, that can be compared with other experiments or with theoretical predictions, the p_T spectra need to be corrected for such effects.

Most of the corrections that were used in this analysis were obtained by using Monte-Carlo simulated events. These simulated events are produced by Monte-Carlo generators that “produce” the particles originating in the simulated collision, based on theoretical models such as PYTHIA[30, 31], PHOJET[62], HIJING[63], EPOS[32] and others. These theoretical models try to reproduce as accurate as possible the distributions of many experimental observables: event multiplicity, p_T spectra, relative particle yields and so on.

The particles produced by the generator are then propagated through the detector by a transport code such as GEANT[64] or Fluka[65]. As this transport code simulates the interactions of each particle with the materials that it encounters a detailed and accurate description of the experimental device geometry is essential. In addition to this the transport code also simulates the decays of unstable particles and the generation of particles in the detector material. As it will be shown in Section 7.4 these simulations are very important also in the estimation of the correction for secondary particles.

During the propagation of the particles, the signals that each particle generates in the detectors are also simulated. This way, the reconstruction of these simulated events is done using the same procedure as for the experimental data, which allows the estimation of potential biases created by the reconstruction procedure. More than this, in the reconstruction of these simulated events, the real detector database is used on a run-by-run basis. This guaranties that the extracted corrections are well estimated for each run by keeping the simulations correlated with the status of each detector during the actual data taking.

For this analysis the distributions from multiple runs were merged and the

result was used to estimate the corrections. This approach reduces very much the statistical fluctuations that are important for individual runs and it is made possible by the fact that, for each run, the number of simulated events is correlated with the number of recorded data events. This way, any specific detector condition that could modify a certain correction for any given run is taken into account in the final result with a proper weight, weight which is given by the ratio between the number of events in each run and the total number of analyzed events.

For the LHC10e period, on which the results presented in this thesis were obtained, the use of this approach is absolutely necessary because, for each run, the number of simulated events are only 10% of the number recorded data events. The total number of simulated Monte-Carlo events that were used to estimate these corrections was $5.5 \cdot 10^6$.

7.1 Tracking efficiency

An ideal experimental device would be able to detect and measure the characteristics of all the particles that pass through it. In reality, not every particle that passes through the detector generates a track that is considered in the analysis. This might happen if the particle encounters a dead zone of the experimental device. Then, even if it hits an active area of the detector the particle may not generate a viable signal because of the limited detection efficiency of the considered detector. More than this, even if the particle is detected and successfully reconstructed, the obtained track may not pass the track quality cuts that were described in Section 5.3.

These effects are well described in the Monte-Carlo simulated events and, in this analysis, they were included in the *tracking efficiency* (red symbols in Fig. 7.1). This efficiency is defined as the ratio between the successfully reconstructed tracks which pass the track quality cuts and all the generated primary particles (Equation 7.1).

$$\text{tracking eff} = \frac{\text{all reconstructed tracks which pass the track cuts}}{\text{generated primary particles}} \quad (7.1)$$

In the analysis task the calculation of this efficiency is straightforward. Similar with the raw p_T spectra, a 2-dimensional histogram was defined, having on one axis the p_T bins and on the other axis 37 arbitrary bins which correspond to the defined multiplicity and directivity classes. Here, 37 bins are enough because, in this case, there is no need to consider separately the p_T spectra of the particles that are identified by the ITS-TPC, TPC and TOF detectors: due to the fact that the estimation of the efficiencies is done using Monte-Carlo simulations, at this stage of the analysis the identity of each particle is precisely known. The fact that the identity of the particles is known, applying the rapidity cut of $|y| < 0.5$ is also straightforward for both the generated particles and for the reconstructed tracks.

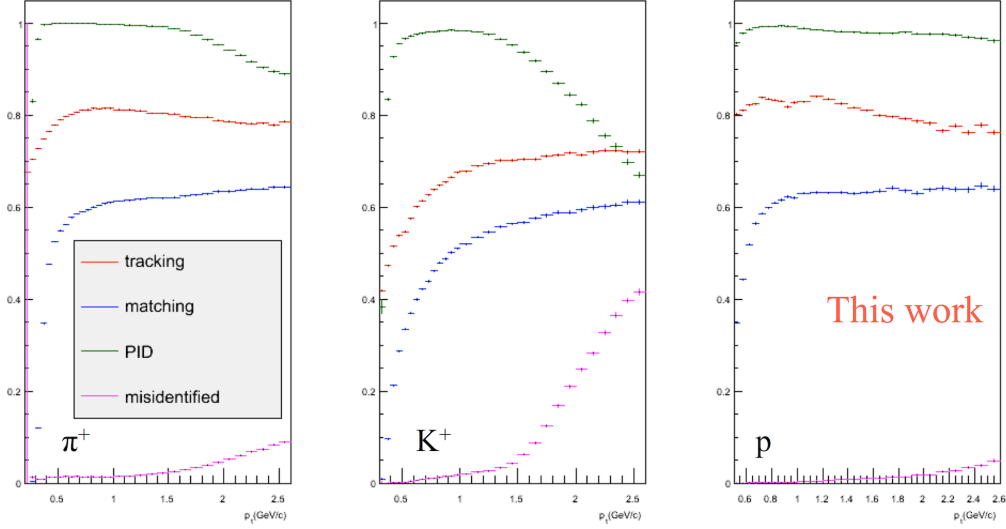


Figure 7.1: Tracking, matching and PID efficiencies and the percentage of misidentified particles. The PID and the misidentified are showed for the TOF.

7.2 Matching efficiency

In addition to the effects described above, the tracks for which the TOF signal is required for identification might be lost because the TOF detector is located at a distance of 3.7 m from the beam axis and because the TRD is located between the TPC and the TOF. This means that the selected reconstructed tracks are matched with a signal in the TOF with a certain probability. This *mismatch efficiency* (blue symbols in Fig. 7.1) is computed as the ratio between the tracks that are successfully matched with a signal in the TOF and the successfully reconstructed tracks which pass the cuts (Equation 7.2).

$$\text{matching eff} = \frac{\text{all tracks matched with a TOF signal}}{\text{all reconstructed tracks which pass the track cuts}} \quad (7.2)$$

This correction must be applied only on the p_T range where the TOF PID signal is requested (see Chapter 6).

Technically, the estimation of this correction is very similar with the determination of the tracking efficiency: the histogram containing all reconstructed tracks which pass the track quality cuts is the same and the identity of the tracks that are matched with a TOF signal are also precisely known from their Monte-Carlo index. Of course, the tracks which were successfully matched with a signal in the TOF are selected using the same condition as the one that is used for the data analysis.

7.3 PID efficiency and percentage of misidentified particles

The PID procedure has a very strong influence on the raw p_T spectra and, in order to correct for it the PID efficiency and the percentage of misidentified particles are used.

The *PID efficiency* (green symbols in Fig. 7.1) is used to correct for the particles that were lost because of the PID procedure. It is defined as the ratio between: the tracks that were correctly identified via the PID method and all successfully reconstructed tracks which pass the track quality cuts, for the low p_T tracks that are identified by using the ITS or the TPC detectors. For higher p_T tracks that require the TOF signal for identification, which are affected by the matching efficiency described above, the PID efficiency is defined by the ratio of the tracks that were correctly identified via the PID method and all the tracks that were successfully matched with a signal in the TOF (Equation 7.3).

$$\text{PID eff} = \begin{cases} \frac{\text{tracks that were correctly identified by the PID method}}{\text{all reconstructed tracks which pass the track cuts}}, & \text{for TPC} \\ \frac{\text{tracks that were correctly identified by the PID method}}{\text{all tracks matched with a TOF signal}}, & \text{for TOF} \end{cases} \quad (7.3)$$

It is important to note that, even though PYTHIA does not reproduce the relative particle yields that are found in the data, the PID efficiency does not depend on these yields and, by running the analysis on the Monte-Carlo sample using the same set of priors for the PID as the one for the data, the PID efficiency is correctly estimated.

The *percentage of misidentified* particles (magenta symbols in Fig. 7.1) is used to remove, from the p_T spectra the contaminations that come from particles that are wrongly identified. This correction is computed using the ratio of all the tracks that are wrongly identified and all the tracks that are identified as a certain species by the PID procedure (Equation 7.4).

$$\text{misidentified} = 1 - \frac{\text{all wrongly identified tracks}}{\text{all identified tracks to be of a certain species by the PID}} \quad (7.4)$$

In Fig. 7.2 the PID efficiency and the percentage of misidentified particles are shown, over the whole p_T range, for ITS-TPC, TPC and TOF based PID responses. The vertical red lines show the actual range in which a certain detector response was used. These p_T ranges (which were mentioned in Chapter 6) were established, based on this representation, in order to have a high PID efficiency and an as low as possible contamination from misidentified particles.

Obtaining these corrections needs a more complex procedure than the one used for the tracking and the matching efficiencies. For each species a 2-dimensional histogram was filled only with the tracks which were correctly

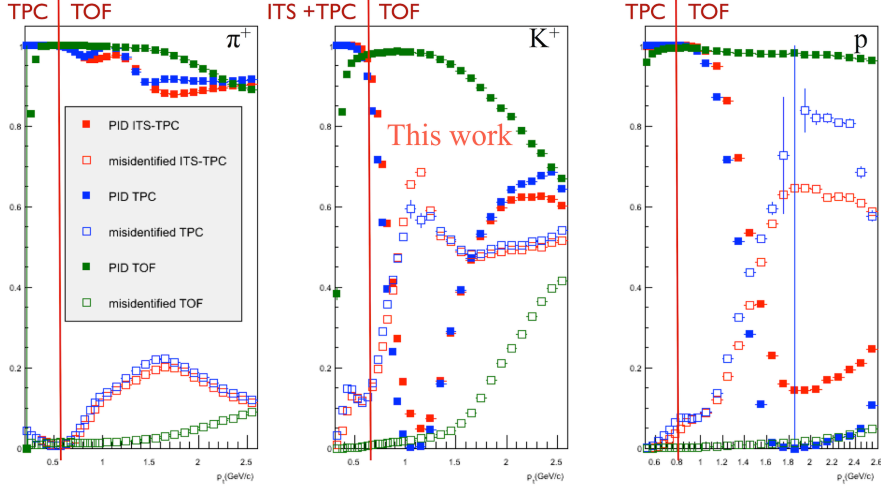


Figure 7.2: PID efficiencies and the percentage of misidentified particles for ITS-TPC, TPC and TOF based on PID responses.

identified by the PID. These tracks were selected by comparing the true identity of each track, based on its Monte-Carlo index, with the identity that was assigned to it by the PID. This histogram has on one axis the p_T bins and, on the other axis, 111 arbitrary bins that correspond to the multiplicity and directivity selections, as in the cases of the tracking and the matching, but this time each of the three detectors were treated separately. The projections along these arbitrary bins gives the numerator in Equation 7.3 and the denominator in Equation 7.4.

For obtaining the numerator of Equation 7.4 a vector of such 2-dimensional histograms was used. For each species this vector has four components: one contains the tracks that are correctly identified and the next three contain the tracks that are wrongly identified, having as sources the other two species and the electrons. As it will be shown next, having the sources of the contaminations accounted for separately is very useful. Obviously, the sum of all these vector components gives all the tracks that were identified as a certain species.

Unlike the case of the PID efficiency which does not depend of the relative particle yields simulated by PYTHIA, the percentage of misidentified particles is sensitive to this. Therefore, in order to take into account this difference in the relative particle yields between PYTHIA and the data, the contaminations from misidentified particles found based on the Monte-Carlo simulations need to be reweighted. This is done by extracting the priors from the data using an iterative procedure developed within the ALICE collaboration [61]. This procedure starts with all priors equal to 1 and, at each step, the detector response is multiplied with the current priors, the result being assigned as the new priors for the next step of the iteration. The procedure converges usually in less than 10 steps and the obtained priors for

the data are plotted with red markers on the second row of Fig. 7.3. The PYTHIA generated relative yields are also plotted with blue markers. Next, the ratios of these distributions coming from the data and the Monte-Carlo simulation are computed for each of the three species (third row of Fig. 7.3). And, finally, as each of the contamination sources is logged independently, these ratios can be used to reweight each contamination source with its own corresponding ratio. The final result is plotted in the first row of Fig. 7.3.

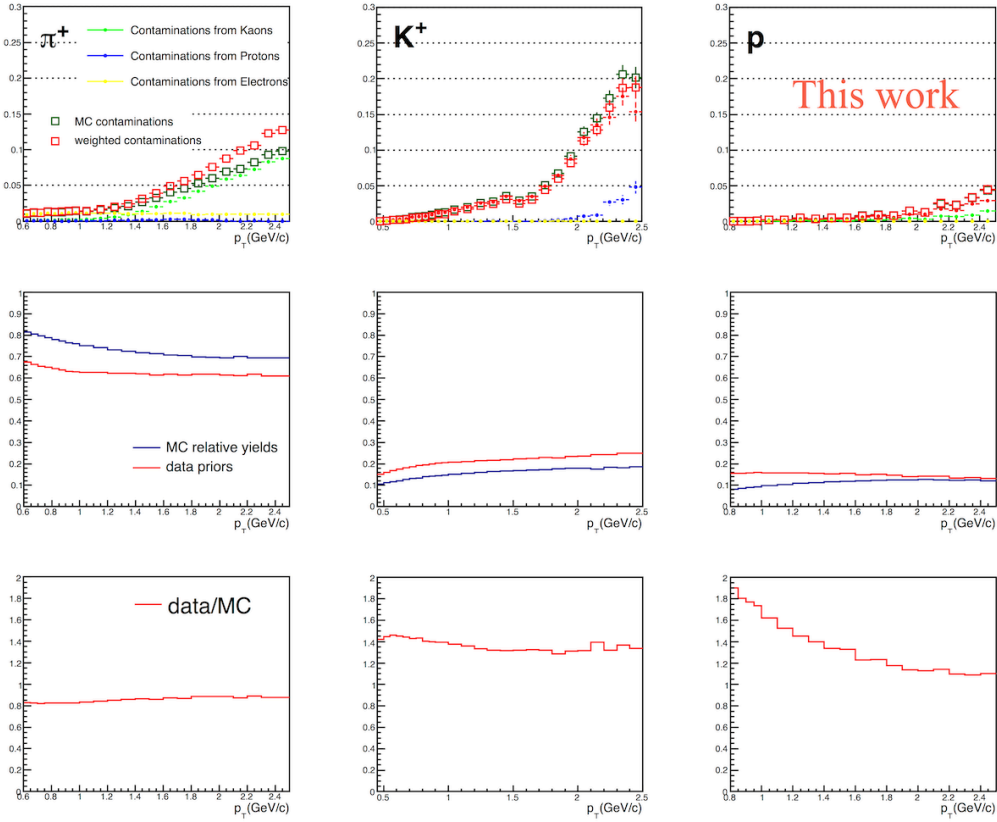


Figure 7.3: Reweighted percentages of misidentified particles.

7.4 Material and weak decay contamination

The p_T spectra of pions and especially that of the protons include, mainly at low p_T , large contributions from secondary particles. As it was described in Section 5.3, primary particles are selected by applying a p_T dependent maximum cut on their distance of closest approach relative to the main vertex (Equation 5.1). Although this condition eliminates most of the secondary particles there is still a quite large number of pions and protons that fulfill this condition but are generated in the weak decays of primary particles or by the interaction of primary particles with the material of the detector.

The procedure used to remove the influence of these particles on the p_T spectra is, in principle, similar with the one used in the case of the misidentified particles. In the Monte-Carlo simulation the origin of each particle is well known so the estimation of the percentage of secondary particles that pass the DCA cut is straightforward. However, as in the case of the percentage of misidentified particles, PYTHIA does not provide an accurate description of the data and a reweighting is needed in order to obtain a proper correction. This reweighting is done by using the DCA distributions of the particles, relative to the main vertex, from the data and from the Monte-Carlo sample. These distributions are obtained by removing the tight p_T dependent DCA cut and considering all the particles in the ± 3 cm range (Fig. 7.4).

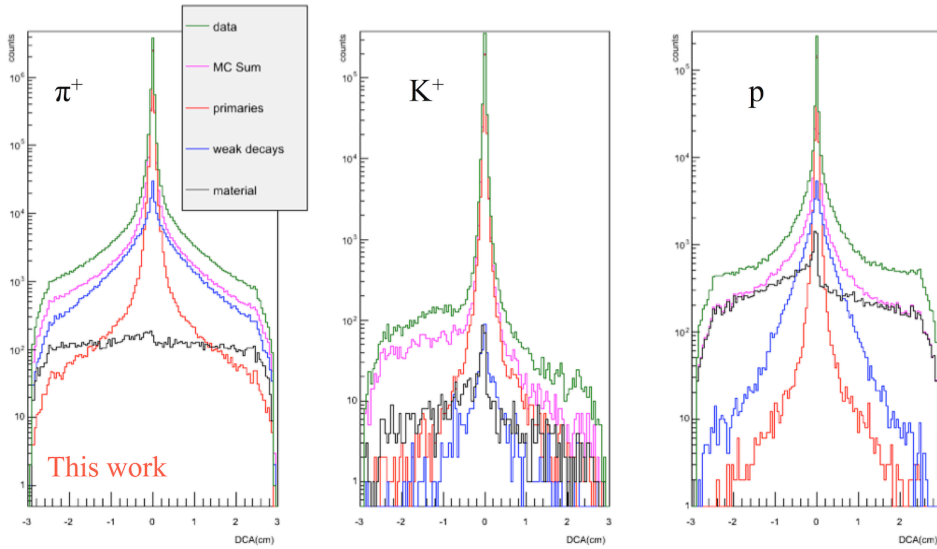


Figure 7.4: Monte-Carlo based shapes of the DCA distributions for particles from different sources. The total DCA distribution from data, not normalized, is also included.

In addition to the inclusive DCA distributions for the data (green symbols) and for the Monte-Carlo sample (magenta symbols), for the Monte-Carlo sample the DCA distributions for the primary particles, the secondary particles coming from weak decays and the secondary particles coming from interactions with the material (red, blue and black symbols, respectively) were also obtained. These DCA distributions are obtained for each p_T bin, in Fig. 7.4 the projection over all the p_T bins is shown. In this figure the DCA distribution from the data was also included, not normalized, in order to show that the inclusive shape of the DCA distribution from the Monte-Carlo simulations (magenta curve) reproduces very well the shape of the experimental distribution (green curve).

The shapes of DCA distributions, for all the contributing particles: primary, secondary coming from weak decays and secondary coming from interactions

with the material, are correctly described by the simulation due to the fact that they are based on the transport code and do not depend on the model used for the generation of particles. The normalization factors for each of these components, needed in order to describe exactly the experimental data, are obtained by fitting the DCA distribution from the data with the sum of the primary, weak decay and material distributions from the Monte-Carlo. As an example, the results of such fits, for positive pions, are shown in Fig. 7.5.

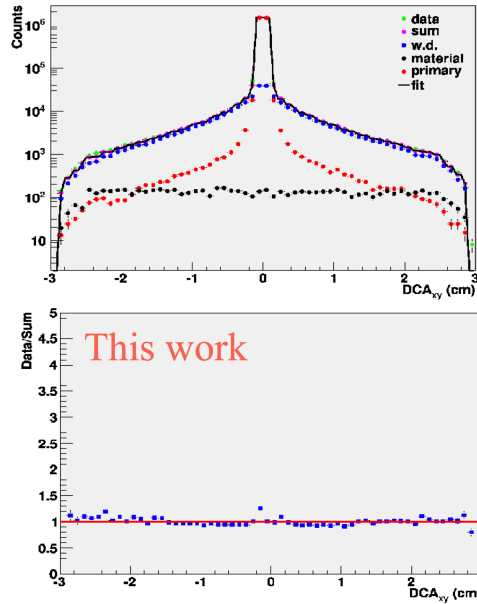


Figure 7.5: The result of the fit of the DCA distributions, for positive pions, in one p_T bin.

In the case of kaons the percentage of secondaries is negligible; for the pions and protons the final results are shown in Fig. 7.6. This result (the red symbols) is compared with the similar correction extracted directly from the Monte-Carlo simulations [66].

7.5 Multiplicity dependence of the corrections

In order to obtain the p_T spectra in the different multiplicity bins that were mentioned in Section 5.2 the behavior of all the corrections as a function of multiplicity needs to be studied. As it was mentioned in Section 5.2 the use of the combined multiplicity estimator, due to its much better performance in reproducing the Monte-Carlo simulated multiplicity distribution, has eliminated the bias on the tracking efficiency that was observed when the global tracks multiplicity estimator was used.

For this study the tracking, matching and PID efficiencies, as well as the

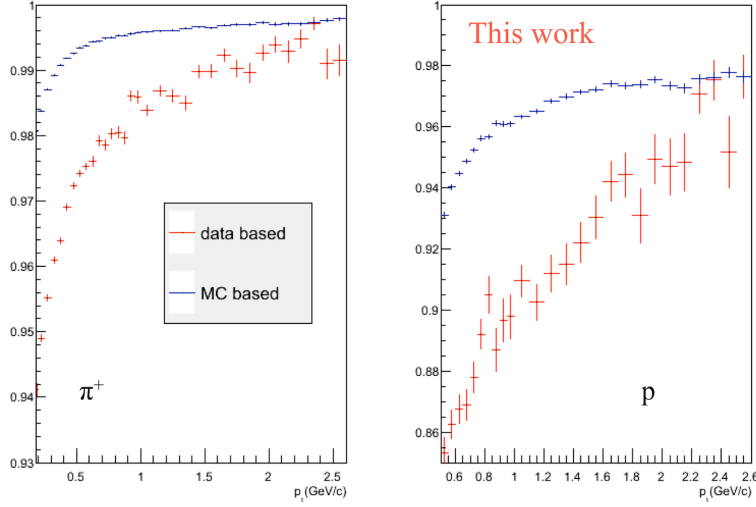


Figure 7.6: Percentage of secondary particles (coming from weak decays and material) as a function of p_T for pions and protons; obtained using the DCA distribution fits on the data (red symbols) and extracted from the MC simulations (blue symbols). For kaons this correction is negligible.

percentage of misidentified particles were estimated, using the procedures described above, but only considering the simulated events with a combined multiplicity belonging to the respective multiplicity bin. The behavior of the correction for secondary particles as a function of multiplicity was studied as a part of the estimation of the systematic errors and it is described in Section 8.5.

In Fig. 7.7 and 7.8 the tracking and matching efficiencies are plotted for all the multiplicity bins. As it can be seen in the bottom row of these figures, where the ratio of the efficiency in each multiplicity bin to the efficiency determined for the MB case is plotted, the variation is below 2% for all the multiplicities and no systematic trend is visible.

For the PID efficiency (Fig. 7.9) and the percentage of misidentified particles (Fig. 7.10), in the kaons case, a multiplicity dependence still seems to exist for p_T larger than 1.5 GeV. This dependence was further quantified and it was included in the systematic errors (see Section 8.5).

Based on this very good stability of the corrections as a function of multiplicity, for this analysis, the corrections determined for the MB case were used to correct the p_T spectra in all multiplicity bins. By using all the available events to estimate the corrections, the statistical fluctuations, that are quite important for the high multiplicity bins, were very much reduced, despite the low number of Monte-Carlo events available for the data period considered in this analysis. Further than this, the use of the same corrections over all the multiplicity bins guaranties that no efficiency related bias is introduced by the correction procedure [67].

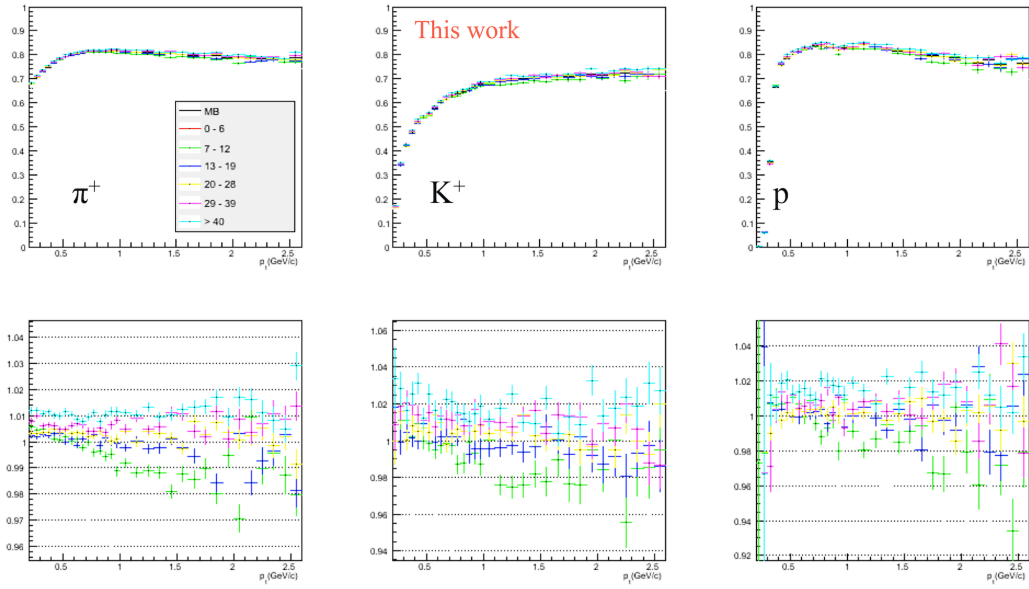


Figure 7.7: Tracking efficiency as a function of multiplicity.

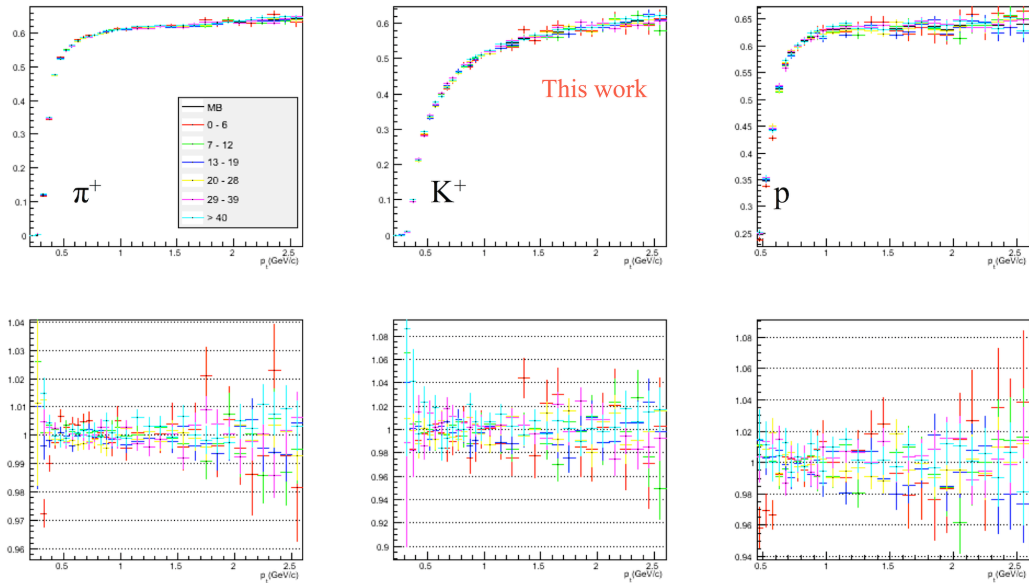


Figure 7.8: Matching efficiency as a function of multiplicity.

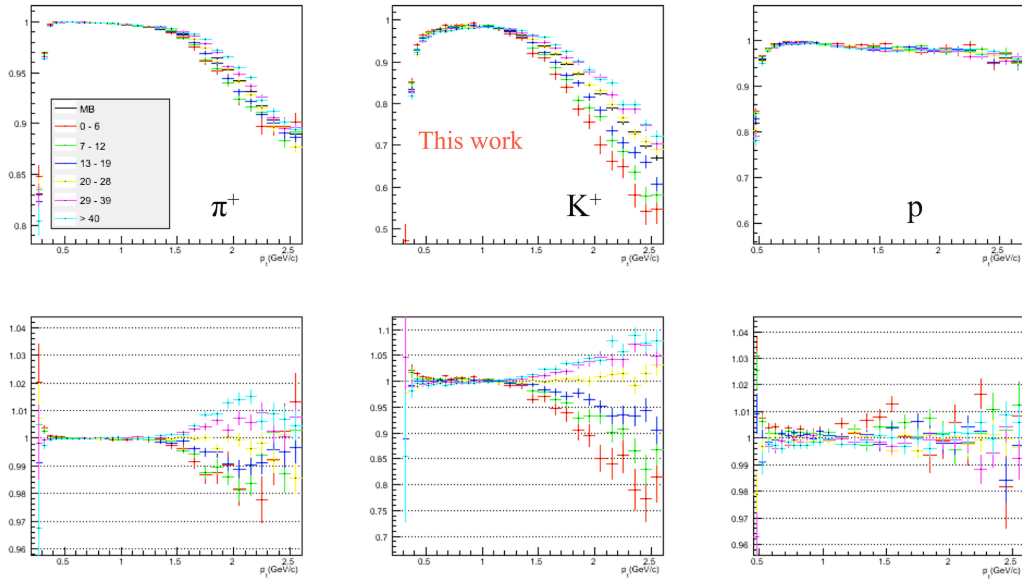


Figure 7.9: PID efficiency as a function of multiplicity for TOF.

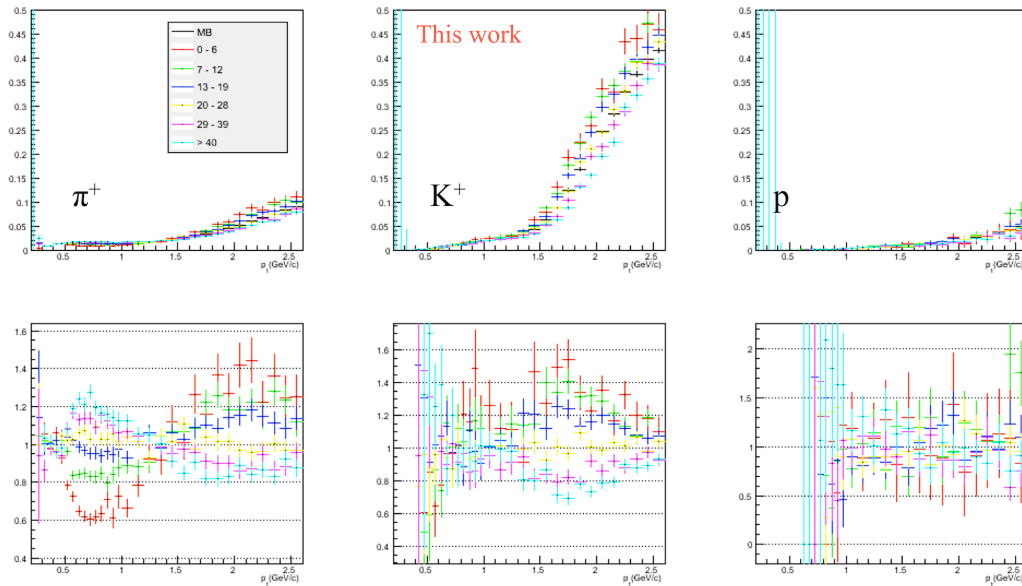


Figure 7.10: Misidentified percentage as a function of multiplicity for TOF.

7.6 Trigger and Vertex efficiencies

The estimation of the corrections for all the combined multiplicity bins is possible, in the analysis task, by selecting the simulated events based on the same reconstructed observables as the ones used for the data: the event has to be successfully triggered, has to have a reconstructed main vertex and this vertex needs to be in the ± 10 cm interval along the z -axis. In this way the combined multiplicity of the considered simulated event can be computed and the event can be assigned to the corresponding multiplicity bin.

The difficulty that appears when using this recipe for computing the corrections is given by the fact that the generated particles used in the estimation of the tracking efficiency (the denominator of Equation 7.1) are not all the generated particles that should be considered but only the generated particles from the simulated events that were triggered, had a reconstructed main vertex and this vertex was in the ± 10 cm interval. These missed generated particles are accounted for by computing a trigger efficiency and a vertex efficiency.

The *trigger efficiency* is defined as the ratio of all the primary, generated particles coming from events that were successfully triggered (events after PhysicsSelection - see Section 5.1) and all the primary, generated particles from all the events in the analyzed Monte-Carlo sample (Equation 7.5).

$$\text{trigger eff} = \frac{\text{all primary particles after PhysicsSelection}}{\text{all primary particles before PhysicsSelection}} \quad (7.5)$$

In the Equation above PhysicsSelection refers to the offline procedure of selection of events with a correct trigger class, described in Section 5.1.

The resulted correction is negligible (blue symbols in Fig. 7.11). This is due to the fact that, like for all the corrections used in this analysis, for both the numerator and the denominator of the above Equation the condition $|y| < 0.5$ has to be fulfilled and, once the event has a particle at mid rapidity, the probability that it will be triggered is very close to 1.

The *vertex efficiency* on the other hand has a strong influence on the obtained spectra. As it can be seen in Fig. 7.11 this correction is about 10% and it is almost constant as a function of p_T and independent of the particle species. The definition of this correction is summarized in Equation 7.6. It accounts for both the events that don't have a reconstructed vertex and for the events that have a vertex but it is outside of the ± 10 cm range.

$$\text{vertex eff} = \frac{\text{all primary particles after PhysicsSelection and vertex selection}}{\text{all primary particles after PhysicsSelection}} \quad (7.6)$$

It is important to note that these two corrections were only applied to the MB p_T spectra (Fig. 9.1). For the p_T spectra in the multiplicity bins these corrections are not needed because, as described in Chapter 9, these spectra are normalized to the number of analyzed events in each multiplicity bin and not to the number of inelastic events as for the MB spectra.

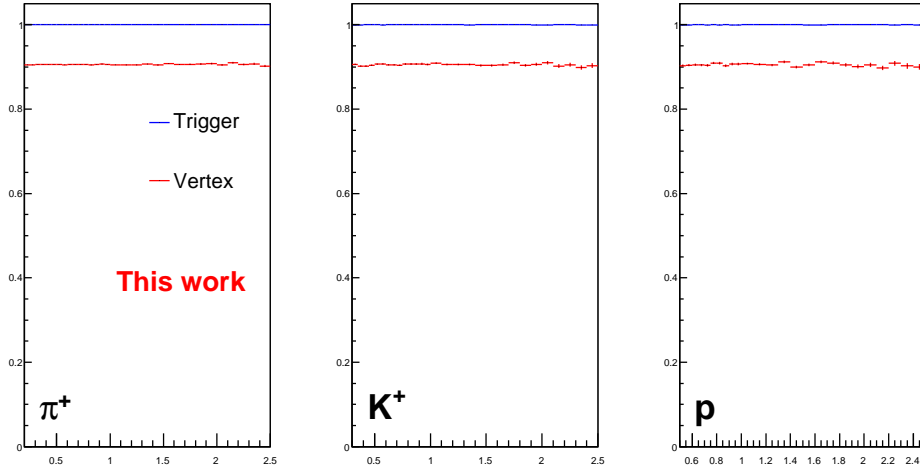


Figure 7.11: Trigger and vertex efficiencies.

7.7 Distribution of the vertex on the z-axis

Because of the fact that the vertex efficiency, described in the above section is based completely on the Monte-Carlo simulations, the fraction of events with the position of the vertex along the z-axis within ± 10 cm range for the data and for the simulations must be compared. In Fig. 7.12 the distributions of the position of the vertex for the two cases are plotted.

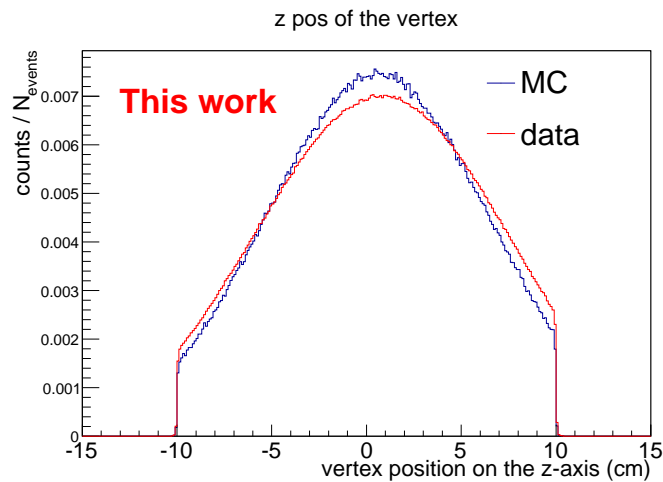


Figure 7.12: The distributions of the vertex position along the z-axis for data and Monte-Carlo simulations.

In order to have a quantitative estimation of the difference between the two distributions the following procedure was used[68]: first the two distributions

were fitted with a gaussian and then, the results of the fits were integrated in the considered range of ± 10 cm and also in the $\pm\infty$ range. The obtained ratio between these two integrals is 0.909 for the Monte-Carlo simulations and 0.874 for the data. By comparing these two results the final correction factor of 1.04 is obtained.

As in the case of the vertex and trigger efficiencies, that were described above, this correction is applied only to the MB p_T spectra and it is constant as a function of p_T .

7.8 Monte-Carlo closure test

The first test that can be performed for the entire correction procedure is to run the analysis, by treating as data a subsample of the same Monte-Carlo simulations that were used to determine the corrections. The “raw” simulated spectra obtained in this way can be then corrected by applying the corrections described above. Due to the use of Monte-Carlo simulations, the final corrected spectra can be compared with the initial generated spectra and obviously, if the corrections are correctly defined and computed, the two spectra should be identical. The results of this test can be seen in Fig 7.13.

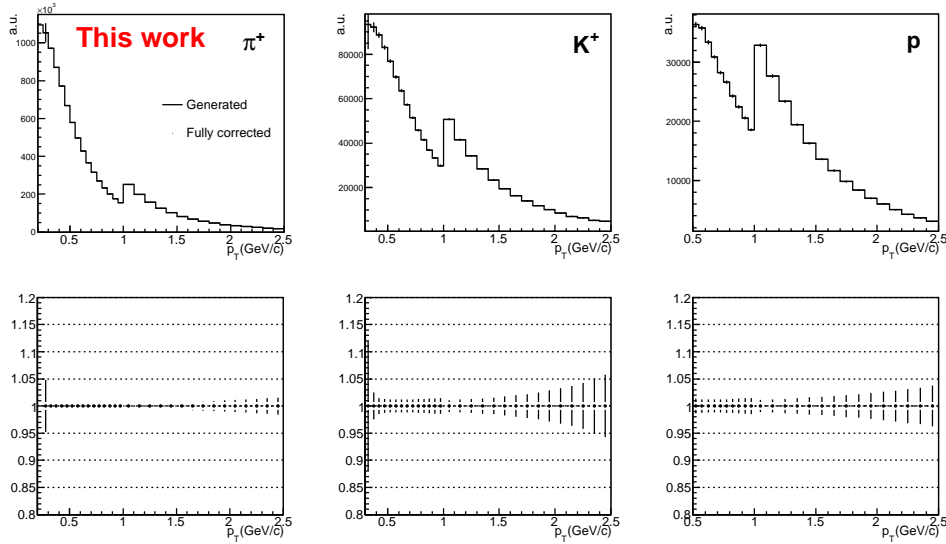


Figure 7.13: Comparison of generated p_T PYTHIA spectra - histograms with reconstructed and corrected PYTHIA spectra - dots with statistical error bars for pions, kaons and protons - upper row. Their ratios - bottom row.

It is important to note that, in order to obtain this perfect reproduction of the initial generated spectra, the used correction for secondary particles should be the one extracted directly from the Monte-Carlo simulations and not the one obtained using the data driven method described in Section 7.4.

This is also true for the correction for the misidentified particles: the percentages of misidentified particles used for the Monte-Carlo closure tests are the ones obtained from the Monte-Carlo sample and not the reweighted ones (Section 7.3).

Another such closure test, that can provide more information than the previously described one, was performed by using PHOJET based Monte-Carlo simulations, treating them as data, and extracting the “raw” spectra in this way. Then, as in the case of the experimental data, these “raw” spectra were corrected by using the efficiencies that were obtained from the PYTHIA based Monte-Carlo simulations, with the two exceptions, described above, of the correction of secondaries and of the percentage of misidentified particles. While the previous closure test demonstrates the consistency of the corrections used in the present analysis it has the drawback that it does not provide a measure of the performance of the PID procedure, because the “data” (in that case PYTHIA reconstructed) and the MC model (in that case the same - PYTHIA) are identical. This drawback is avoided, as described above, by using PHOJET as “data” PYTHIA for corrections. The two models have rather different particle ratios as a function of p_T , as could be seen in the bottom row of the Fig. 7.14 where the ratios of K^+/π^+ ; p/π^+ and p/K^+ predicted by the two models are represented as a function of p_T .

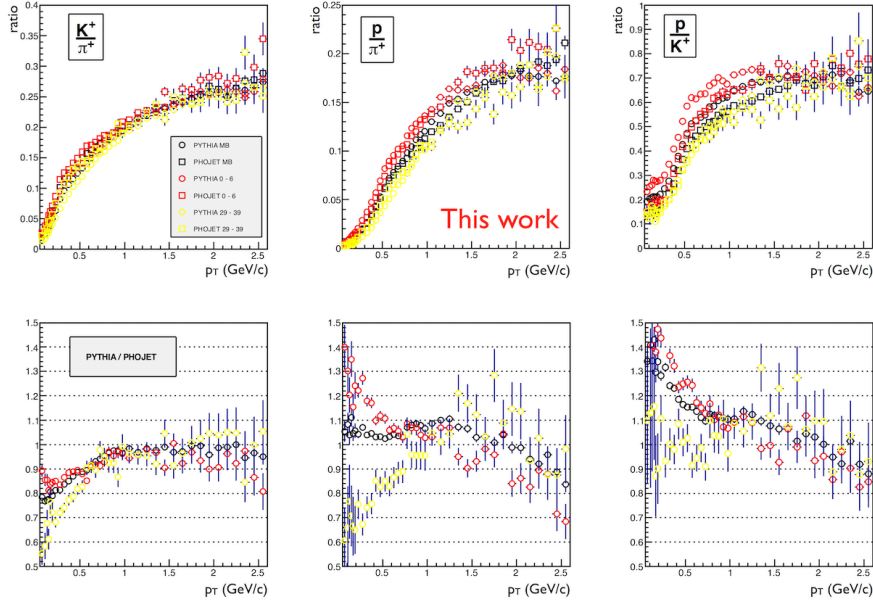


Figure 7.14: Comparison of generated particle ratios for PHOJET and PYTHIA, i.e. K^+/π^+ ; p/π^+ and p/K^+ , as a function of p_T for MB and two multiplicity bins - upper row and their ratios as a function of p_T - bottom row.

As it can be seen in Fig. 7.15, the p_T spectra in all the multiplicity bins are very well reconstructed. For the MB spectra, which are not affected by

statistical fluctuations that dominate the high multiplicity bins, the agreement is within $\pm 2\%$. A considerable difference is observed only in the case of the kaons, for p_T higher than 1.5 GeV/c and only for the lowest multiplicity bin. This effect is explained by the fact that, for low multiplicity events, the start time of the event is determined with a very low resolution. This low resolution affects the TOF based PID in the most sensible case which is that of the high p_T kaons.

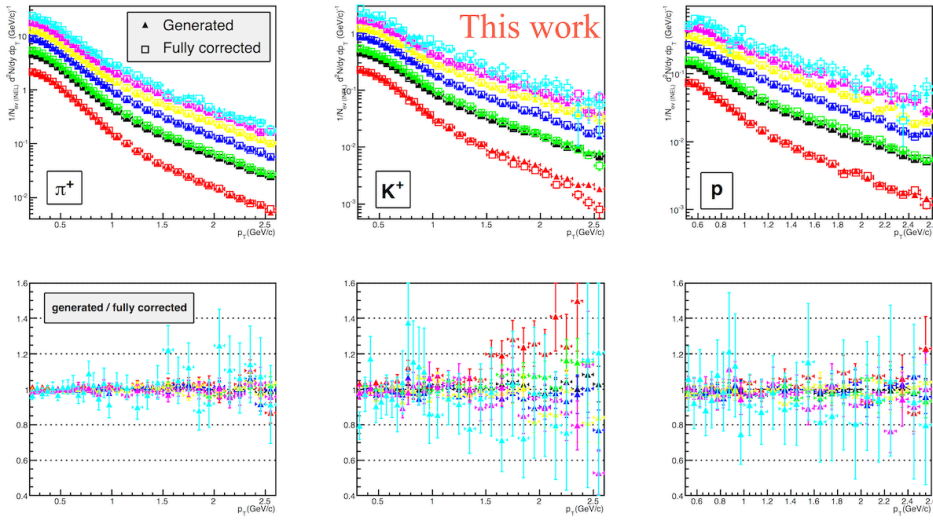


Figure 7.15: Comparison of generated particle ratios for PHOJET and PYTHIA, i.e. K^+/π^+ ; p/π^+ and p/K^+ , as a function of p_T for different multiplicity bins - upper row and their ratios as a function of p_T for MB - bottom row.

First, this very good agreement shows that there is no dependence of the corrections on the generator that is used in the Monte-Carlo simulations. This is a critical test for the entire correction procedure.

Second, the corrections determined for the MB case are used for obtaining the p_T spectra in all the multiplicity bins, exactly as in the case of the experimental data and the initial generated p_T spectra in all the multiplicity bins are very well reproduced. This, together with the cross-checks described in Section 7.5, supports the conclusion that the corrections determined for the MB selection can be used to correct the p_T spectra in all the multiplicity bins.

Third, as in the case of the experimental data, the same set of priors for the bayesian PID was used, for the two Monte-Carlo simulations and for all the multiplicity bins, the result obtained confirming that this procedure does not introduce a bias in the final spectra. This effect of the priors over the final spectra was further studied as a part of the systematic errors and the results are shown in Section 8.3.

Chapter 8

Systematic errors

In order to estimate the systematic errors assigned to the final spectra, three different approaches were used. First, the values of the parameters that define the selection of the tracks considered in the analysis were varied between some reasonable limits and the effect of this variation on the final spectra was evaluated. In this case both the raw spectra and the related corrections were determined using the modified parameters. Second, there are systematic effects that are common to a wide range of analysis within the ALICE Collaboration because they are generated by detector limitations or by the reconstruction procedure. Such effects were evaluated in dedicated studies and those relevant for this analysis are described below. Third, for the spectra in multiplicity bins, a systematic error was added in order to account for the variations of the corrections as a function of multiplicity.

8.1 Variation of the track quality cuts

As already mentioned, after each change of the cuts parameters the entire analysis procedure was repeated and both the raw spectra and the corrections were determined using the new conditions. The difference between the two extreme cases was computed and the result is presented as a percentage of the value that was obtained using the standard conditions. Then, in order to eliminate the statistical fluctuations that can affect this estimation, the difference relative to the standard condition was fitted by a third order polynomial. However, as each p_T spectrum is obtained by combining two regions in which the identification is provided by different detectors (see Chapter 6), the two regions were fitted independently, the resulting error reflecting the behavior of the respective detector.

The effect on the final p_T spectra for each of the considered parameters and the associated p_T dependent systematic errors are presented in the following. As described in Chapter 7, a minimum number of 70 TPC clusters associated to the track was required for the track selection. In order to have an estimate of the influence of this cut on the p_T spectra the analysis was repeated using a low and a high value of 60 and 80 respectively, for the minimum number of

clusters. The results are presented in Fig. 8.1 in terms of p_T spectra, upper row, and the difference relative to the standard cut in the bottom row. While up to p_T values lower than 1.2 GeV/c the difference is negligible, above this value it starts to increase up to 3-4%.

The contribution of statistical fluctuations was eliminated by fitting the absolute values of the relative difference using a third order polynomial. The result is showed in Fig. 8.2.

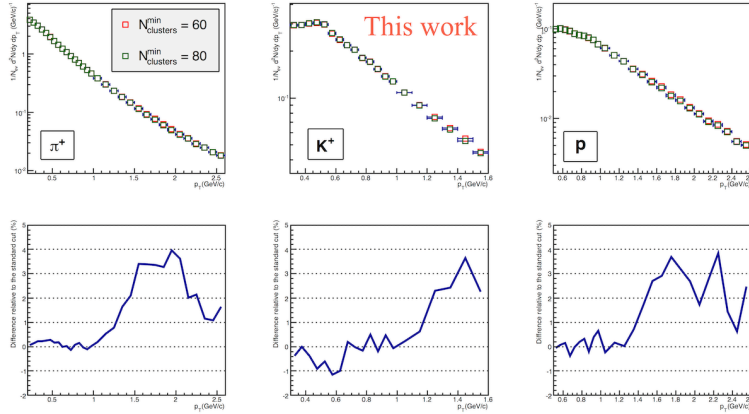


Figure 8.1: Systematic errors associated with the cut in the number of TPC clusters.

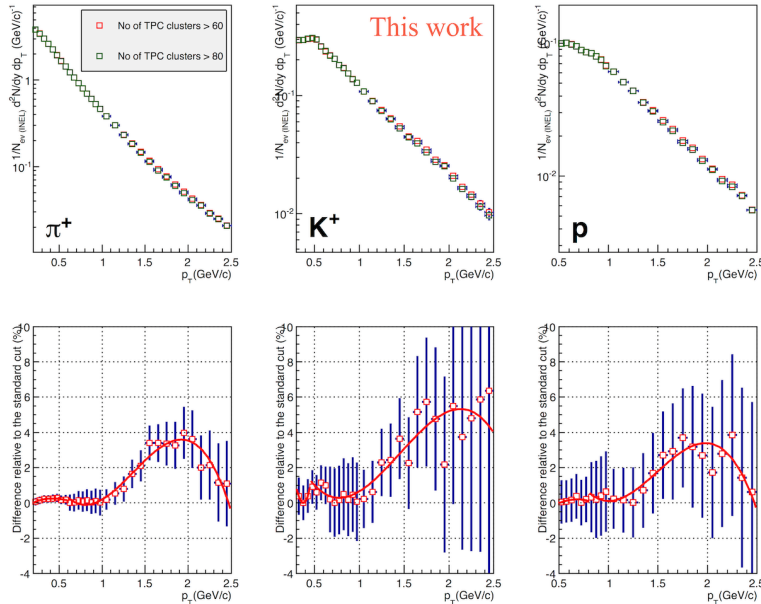


Figure 8.2: Fits of the systematic errors associated with the cut in the number of TPC clusters.

Another very important parameter of the track selection is the χ^2 per TPC cluster. In this analysis the maximum χ^2 per TPC cluster was set at 4. To

evaluate the associated systematic error the analysis was run setting this parameter at 3 and 5 (Fig. 8.3). Further, the results were treated exactly as in the case of the minimum number of TPC clusters: the absolute values of the relative difference were fitted and the result of the fit was considered as a p_T dependent systematic error. This adds a maximum value of 4% systematics errors for pions and 6% for kaons and protons.

The tracks were also selected by applying a cut in the maximum DCA in the z-direction of 2 cm. A variation of this parameter between 1 cm and 3 cm resulted in a systematic error that increases with the p_T and reaches 2% at 2.5 GeV for kaons and protons; for pions this error is negligible.

For the part of the spectra that uses the TOF for PID (see Chapter 6) the TPC track has to be matched with a signal in the TOF. This condition is imposed by requiring a maximum mismatch probability of 0.01. This maximum value was increased and decreased with 10% respectively. For the pions and protons the resulted systematic error is under 1%; for the kaons, at 2.5 GeV, this error reaches 3%.

8.2 Influence of the TRD subdetector

Also, for tracks with p_T larger than 0.6, 0.45 and 0.8 for pions, kaons and protons, respectively, which require the TOF signal for identification, the influence of the TRD modules, which are placed in front of the TOF, has to be evaluated. As described in Section 4.2, in 2010, when these data were recorded, the TRD was incomplete and, in order to estimate the effect of its presence, the analysis was run considering only the tracks that passed through the TRD and the results were compared with the tracks that did not suffered the TRD influence. As it can be seen in Fig. 8.6 the maximum systematic error associated with the presence of the TRD reaches 6% at 2.5 GeV.

8.3 PID procedure

The PID procedure, described in Chapter 6 is a complex part of the analysis and the systematic effects related to it were also evaluated.

For this, the analysis was run using two different sets of priors which were obtained using the iterative procedure described in Section 7.3. The priors determined for the MB case, for multiplicity bellow 6 and for multiplicity above 49 are shown in Fig. 8.7.

The final spectra that were obtained using the different sets of priors are shown in Fig. 8.8. In the case of the pions the difference does not exceed 1%, for the kaons and protons the error increases with the p_T , reaching 2% at 2.5 GeV.

As it will be shown in Chapter 9 the relative yields of pions, kaons and protons change significantly as a function of multiplicity but for the bayesian PID the

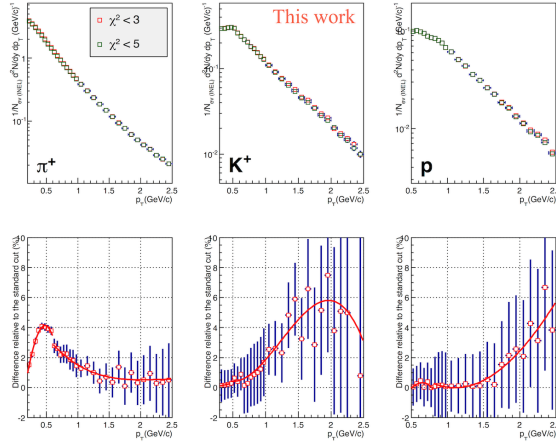


Figure 8.3: Systematic errors associated with the cut in the maximum χ^2 per TPC cluster.

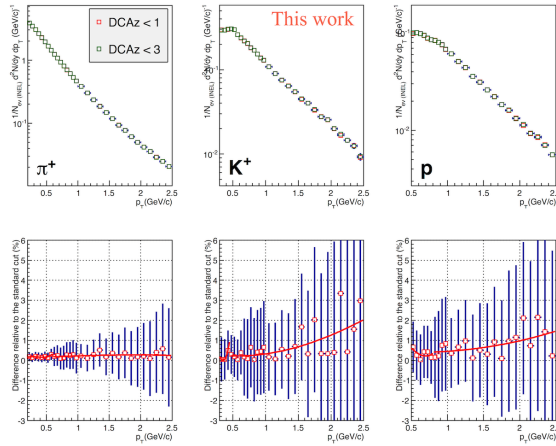


Figure 8.4: Systematic errors associated with the cut in the maximum DCA for the z-direction.

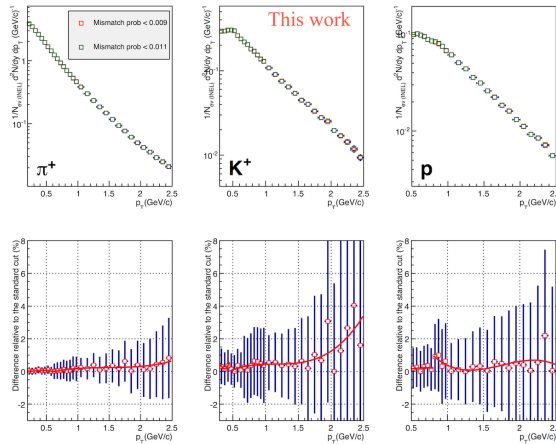


Figure 8.5: Systematic errors associated with the cut in the maximum TPC-TOF mismatch probability.

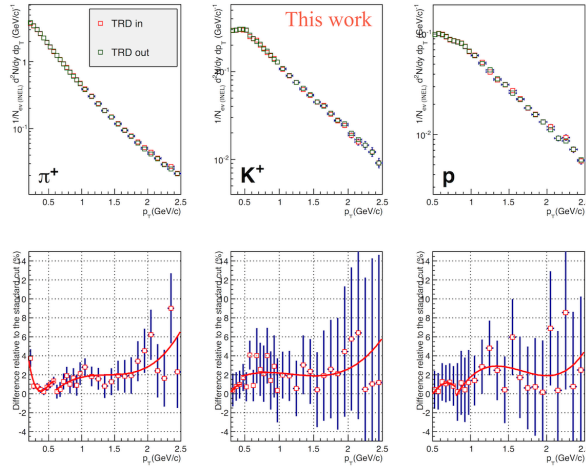


Figure 8.6: Systematic errors associated with the presence of TRD modules in front of the TOF.

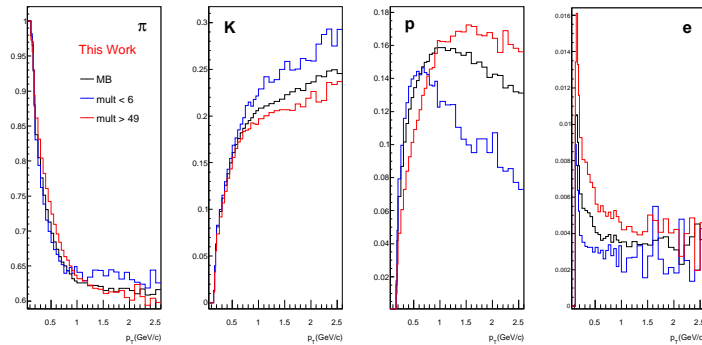


Figure 8.7: Priors determined using an iterative procedure for MB, multiplicity < 6 and multiplicity > 49.

priors used were always the ones determined for the MB case. Therefore, the effect of different priors over the PID procedure had to be evaluated and, due to the fact that the sets of priors that were determined as described before are quite different this result provides not only an estimation of the systematic errors associated with the selection of the priors, but also a very important stability test for the bayesian PID procedure. Based on the above result for the bayesian PID the priors used were always the ones determined for the MB case.

Another parameter that influences the response of the PID procedure is the purity cut. As it was described in Chapter 6, in the present analysis, except for the kaons above 1.5 GeV, no purity cut was used and, in order to evaluate the effect of this selection on the final spectra, the analysis was rerun after

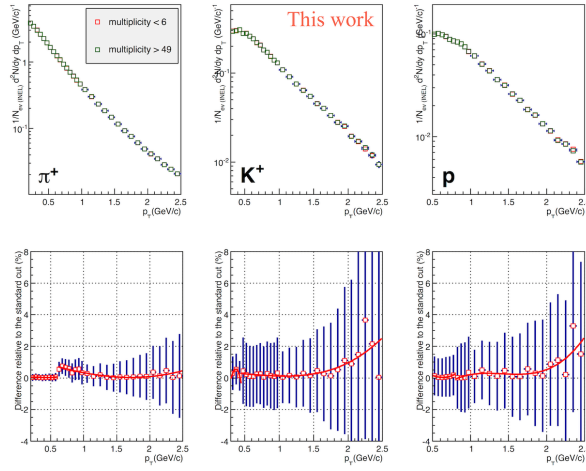


Figure 8.8: Systematic errors associated with the use of different priors for the bayesian PID procedure.

applying a 80% minimum probability cut for all the species over the entire p_T range. As it can be seen in Fig. 8.9 the difference is below 4% for pions and protons but, in the case of the kaons, a very sharp increase of the difference is observed for p_T below 0.45 GeV. This effect is explained by the fact that, in this p_T range, the kaons are identified using the TPC and, by requesting a purity above 80%, the PID efficiency drops drastically.

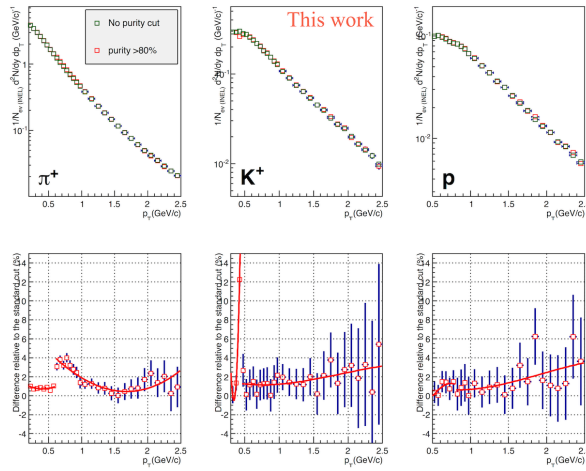


Figure 8.9: Systematic errors associated with the use of a 80% minimum probability cut for the bayesian PID procedure.

8.4 Tracking and matching

The uncertainty of the tracking efficiency was determined in dedicated studies, within the ALICE Collaboration, in which MC simulations with different material budgets were used. By comparing these simulations the associated systematic error was estimated at 4% for unidentified charged particles over the entire p_T range. For identified particles this value is expected to decrease but, as these studies are still underway, it was decided that a conservative systematic error of 4%, associated with the tracking efficiency, should be used for all the three species.

For the tracks that are identified using the TOF an additional correction is needed in order to account for the TPC tracks that are not matched with a TOF signal (see Chapter 7). The systematic error of this matching efficiency was studied at $\sqrt{s} = 900$ GeV [69] by comparing the matching efficiency that was extracted from MC simulations (as it is used also in this analysis) with the matching obtained from the data. The obtained results were 3% for the pions, 6% for the kaons and 4% for the protons and these values were included as systematic errors in this analysis.

8.5 Multiplicity variation of the corrections

As it was described in Chapter 7 the p_T spectra obtained in different multiplicity bins were corrected using the efficiencies determined for the MB case. Although, as already shown, there is no significant multiplicity dependence of the corrections, the differences between the corrections determined on a low multiplicity bin (multiplicity between 7 and 12) and the ones obtained for a high multiplicity bin (multiplicity between 29 and 39) were evaluated and used in the estimation of the systematic errors.

For the tracking (Fig. 8.10) and the matching, the ratios of these efficiencies to the one determined on MB (which was used to correct the spectra) are constant as a function of p_T . In order to eliminate the statistical fluctuations, which are quite important for the high multiplicity bin, these ratios were fitted with a zero degree polynomial and the difference between the two cases was assigned to the p_T spectra as systematic errors. This fitting procedure generates, of course, a systematic error that is constant as a function of p_T , however, as described above, the ranges where the identification is provided by different detectors were fitted independently.

In the cases of the PID efficiency (Fig. 8.11) and of the percentage of misidentified particles the ratios of the efficiencies in the low and high multiplicity bins to the MB one are no longer constant for kaons above 1.5 GeV. In this cases the ratios were fitted using a second degree polynomial and for the kaons PID efficiency the associated systematic error reaches 15%.

The correction for secondary particles was obtained, as it was explained in Chapter 7, with a rather complex procedure that uses the MC shapes for

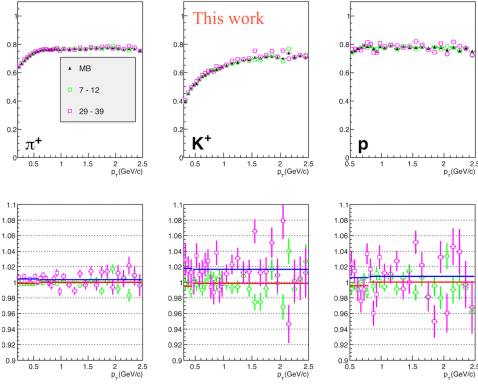


Figure 8.10: Systematic errors associated with the multiplicity variation of the tracking efficiency.

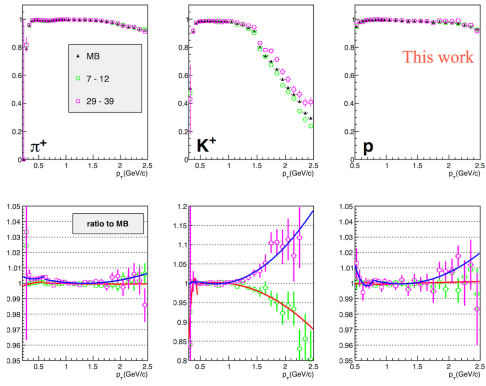


Figure 8.11: Systematic errors associated with the multiplicity variation of the PID efficiency; only for TOF.

the DCA distributions of primary particles, of particles coming from weak decays and of particles coming from conversion in the detector material to fit the total DCA distribution from the data. In order to check the behavior of this correction as a function of multiplicity, first the behavior as a function of multiplicity of the Monte-Carlo shapes of the DCA distributions was studied. As it can be seen in Fig. 8.12 there is no modification of the simulated percentage of secondary particles. Based on this result, the shapes of the DCA distributions of primary particles, of particles coming from weak decays and of particles coming from conversion in the detector material which were determined for the MB were used to estimate the percentage of secondary particles when only data events with a multiplicity above 49 were considered. Similar to the PID efficiency and to the percentage of misidentified particles,

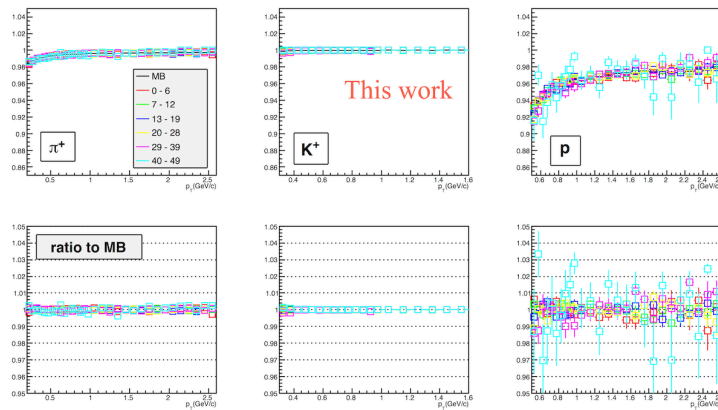


Figure 8.12: The behavior as a function of multiplicity of the simulated percentage of secondary particles.

the difference between the MB correction and the high multiplicity case was

fitted using a second degree polynomial (Fig. 8.13). For all the species, except the kaons where this correction is negligible, the result is well below 1% on the entire p_T range.

As in the case of the variation of the priors with the multiplicity this result is also an essential stability check of the entire DCA based estimation of the percentage of secondary particles.

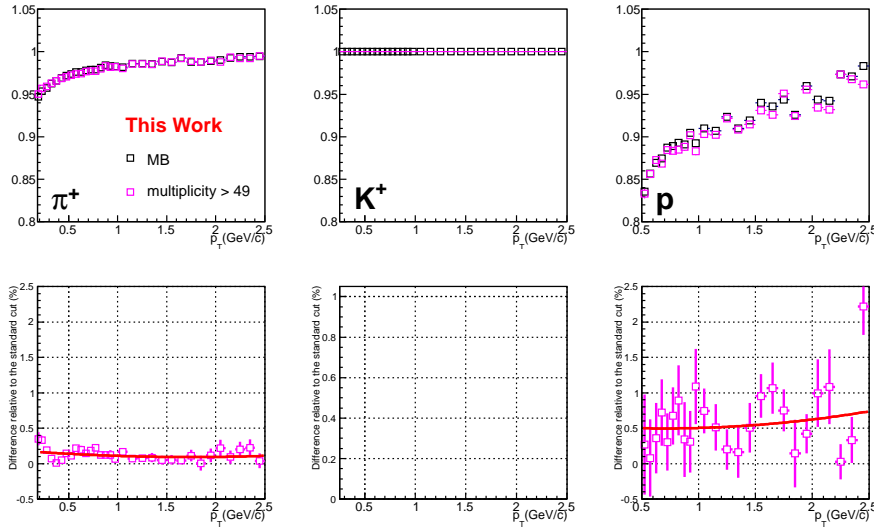


Figure 8.13: Systematic errors associated with the multiplicity variation of the correction for secondary particles; for the kaons this correction is negligible.

8.6 Combined systematic errors

For the MB p_T spectra all the systematic errors described above, except the ones coming from the multiplicity variation of the corrections, were added quadratically, for each p_T bin. The combined systematic errors are plotted in Fig 8.14 as a function of p_T .

For the p_T spectra in multiplicity bins, in addition to the errors from the MB case, the errors described in Section 8.5 were also added, the result being shown in Fig. 8.15. As it can be seen from the plot, for the p_T spectra in multiplicity bins the errors are significantly larger only for kaons above 1.5 GeV, where the variation of the PID efficiency with the multiplicity is important.

However, one has to note that, despite the fact that the obtained differences were fitted, the effect of the limited available statistics was only diminished, not eliminated. These statistical fluctuations play a very important role especially in the estimation of the variation of the corrections with the multiplicity, where the distributions for the high multiplicity bins are affected by

the very limited number of available MC events. Therefore, this estimation of the systematic errors has to be considered conservative.

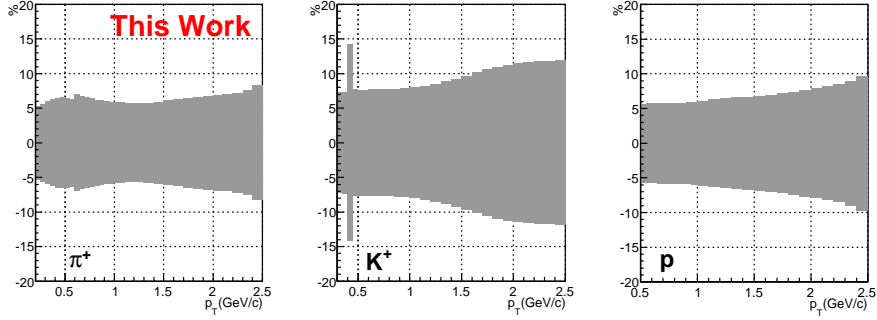


Figure 8.14: Total systematic error for the MB p_T spectra.

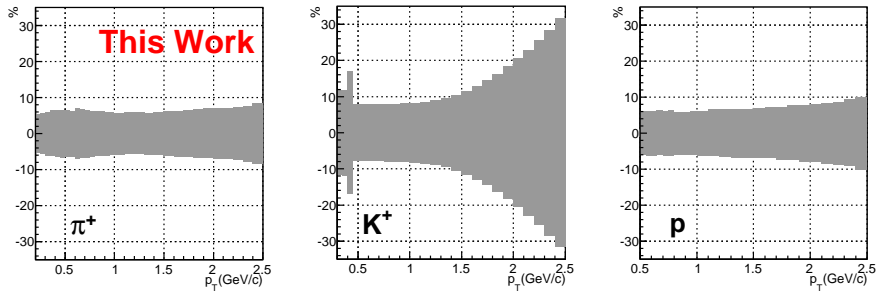


Figure 8.15: Total systematic error for the p_T spectra in multiplicity bins.

All the sources of systematic errors that were described above are summarized in Table 8.1.

	standard	low	high	pions	kaons	protons	
MB	TPC clusters	70	60	80	0 - 4%	1 - 5%	0 - 3.5%
	TPC χ^2	4	3	5	0.5 - 4%	0 - 6%	0 - 6%
	DCAz	2 cm	1 cm	3 cm	<1%	0.5 - 2%	0.5 - 1.5%
	Mismatch probability	<0.01	<0.009	<0.011	<1%	0.5 - 3.5%	1%
	TRD presence	all tracks	WITH TRD	WITHOUT TRD	1 - 6%	2 - 6%	1 - 4%
	Tracking		dedicated study		4%	4%	4%
	Matching		dedicated study		3%	6%	4%
	PID priors	MB	mult <6	mult >49	<1%	0.5 - 2%	0.5 - 2%
	PID purity	none	-	>80%	0.5 - 4%	2 - 12%	1 - 4%
	tracking efficiency				<1%	2%	1%
	matching efficiency	MB	7 - 12	29 - 39	negligible	negligible	negligible
	PID efficiency				<1%	0 - 30%	0 - 2%
	misidentified				<1%	<1%	<1%
secondary particles	MB	-	mult >49	<0.5%	-	0.5%	

Table 8.1: Summary of the sources of systematic errors.

Chapter 9

p_T distributions

The raw p_T spectra obtained as described in Section 5.3 were corrected using the efficiencies described in Chapter 7.

For these results $\sim 60 \cdot 10^6$ MB trigger events were analyzed which correspond to a total number of $\sim 70.4 \cdot 10^6$ inelastic events.

For the very high multiplicity events enough statistics was obtained using the hardware HM trigger described in Section 5.2. In the analyzed data sample $\sim 3.8 \cdot 10^6$ HM events were selected.

9.1 Comparison with similar MB p_T spectra

The obtained fully corrected spectra, normalized to the number of inelastic collisions, for the minimum bias case, are compared, as a final validation, with the similar spectra obtained within the ALICE collaboration.

The MB p_T spectra from 7 TeV p+p collisions were already approved as “preliminary” by the ALICE collaboration and therefore, these spectra provide a very good benchmark for this analysis.

The “preliminary” 7 TeV p+p MB spectra [70] are based on LHC10b and LHC10c periods and were obtained by combining four independent p_T spectra. These spectra are based on the ITS and TPC detectors, where the specific-energy loss (dE/dx) is used for the PID, on the TOF where the velocity of the particles is measured and on the HMPID which uses Cherenkov radiation.

The corresponding independent analyses were developed within the groups that were involved also in the calibration of the respective detectors and each of them can provide p_T spectra on the limited p_T range on which each detector has PID capabilities. All these partial p_T spectra were combined in order to obtain the final MB spectra on a wide p_T range: from 0.1 up to 3 GeV/c for pions and kaons and up to 6 GeV/c for protons. Two very different particle identification techniques were used for the different analyses: a track-by-track 3-sigma cut around the Bethe-Bloch parametrization of the dE/dx curves (for ITS and TPC detectors) and an inclusive unfolding method, i.e. the response of the detector being fitted with a superposition of

Gaussian-like shapes (one for each particle) plus background, in bins of p_T (for TOF and HMPID).

Therefore, comparing the MB p_T spectra obtained using the analysis procedure described in this thesis with the ALICE “preliminary” spectra that were obtained as an average of all the analyses described above represents a very good test of the entire analysis.

In Fig. 9.1 the result of this comparison is shown. A very good agreement within the statistical and systematic error bars can be observed on the upper row of the figure, although the methods used in the two analyses, as already mentioned, as well as the analyzed data sets are very different. In the bottom row of the figure, where the ratios of the p_T spectra are represented, a systematic increase of the ratio for the kaons as a function of p_T starting from ~ 1.2 GeV/c up to 1.6 GeV/c where it levels off at about a value of 1.2 is observed.

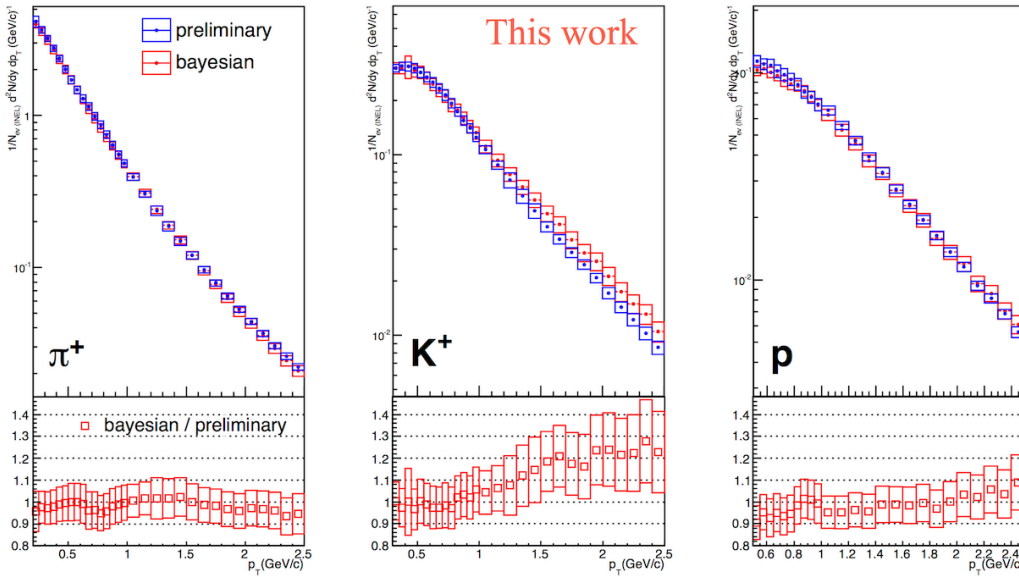


Figure 9.1: The fully corrected MB spectra from this analysis compared with the ALICE “preliminary” ones; includes data from [70].

In addition, for this sensitive case (from the point of view of the PID) of the kaons an extra comparison was done.

The p_T spectra for MB obtained in the present analysis for K^+ and the “preliminary” p_T spectra of K^+ [70], K_s^0 [71] and kinks analysis [72] were compared and the result can be seen in Fig. 9.2. In the bottom row, left side, are presented the ratios of the p_T spectra of K_s^0 , kinks, and K^+ of preliminary 7 TeV p+p MB spectra relative to the K^+ p_T distribution of the present analysis.

On the bottom right side, the same ratios are shown but removing the “preliminary” spectra in order to make the comparison with K_s^0 and kinks spectra

easier to be followed. With a small general offset of $\sim 5\%$, within $\pm 5\%$, there is a very good agreement between the result of the present analysis and those for K_s^0 and kaons obtained from kinks analysis.

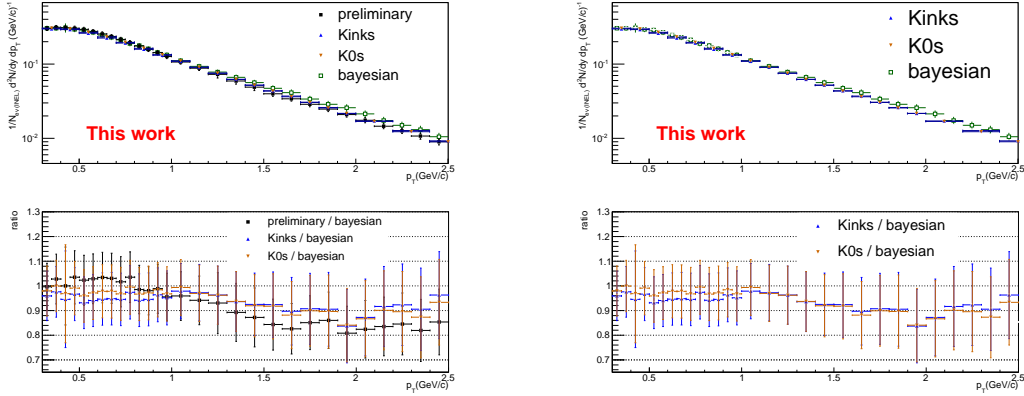


Figure 9.2: The fully corrected MB spectrum K^+ from this analysis compared with “preliminary” 7 TeV p+p MB K^+ spectrum, K_s^0 spectrum, kinks spectrum; includes data from [70, 71, 72].

Another check that has been done was to compare the sum of the identified particles obtained in this analysis with the charged particles distribution obtained for minimum bias by using the average Jacobian. In Fig. 9.3 it is shown the comparison between the sum of MB identified charged hadrons spectra obtained in this analysis and the MB charged particles spectrum obtained in other ALICE analyses [73, 74]. The agreement is good in all cases, the deviations being less than $\pm 5\%$.

9.2 Comparison with similar p_T spectra as a function of multiplicity

The next step was to compare the summed identified p_T distributions with the charged particles spectra obtained in the same multiplicity bins in another ALICE analysis [74]. This comparison can be seen in Fig. 9.4. The ratios were fitted with a zero-degree polynomial and the two lines correspond to the two extreme values of fit results. The agreement is again within $\pm 5\%$. For p+p collisions at 7 TeV, p_T spectra in bins of multiplicity were obtained also by the CMS experiment [75]. Taking into account the differences between CMS and ALICE in terms of detector performance and the phase space in which the data were analyzed, it is rather difficult to compare the distributions obtained in the present work with the CMS ones. The normalization of the distributions is different in the two cases. Nevertheless one could compare the shapes of the p_T spectra. As it can be seen from Table 5.1 and Table 9.1, the correspondence between the multiplicity bins in ALICE and CMS is not one to one.

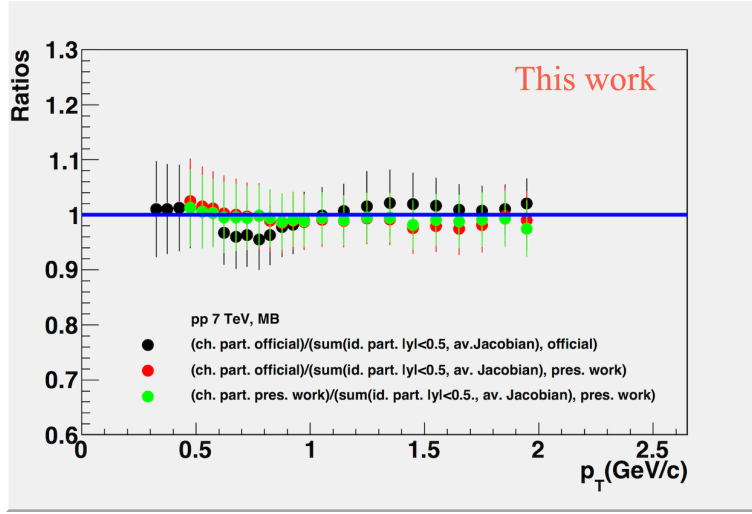


Figure 9.3: The sum of the MB p_T distributions for identified charged hadrons obtained in this analysis compared with the charged particles spectrum, obtained in other ALICE analyses; includes data from [73, 74].

N_{rec}	0-9	10-19	20-29	30-39	40-49	50-59	50-69	70-79	80-89	90-99	100-109	110-119
$\langle N_{tracks} \rangle$	7	16	28	40	52	63	75	86	98	109	120	131

Table 9.1: Correlation between the number of reconstructed (N_{rec}) and true ($\langle N_{tracks} \rangle$) in the 12 multiplicity bins within $|\eta| < 2.4$ range by the CMS collaboration [75].

Thus the comparison has been done by normalizing the p_T spectra to the integral of the distribution. In the CMS case the values given by CMS have been used. In the ALICE case the value of the integral has been determined from the fit with the Levy - Tsallis function on the measured range: 0.17-2.6 GeV/c for pions, 0.25-1.4 GeV/c for kaons and 0.45-2.6 GeV/c for protons, respectively. Then, the ratio of the two distributions has been done. For non equivalent multiplicity bins the ratio is not a constant but a line with a given slope relative to a horizontal line. In the case of equivalent multiplicity bins this ratio has to be 1 as proved to be in most cases or, in the worst case, a constant, over the whole p_T range. This latter situation appears more often in the case of kaons. The χ^2 of the ratio relative to this constant has been determined globally for pions, kaons and protons distributions and the bin correspondence has been established to be for the case of the minimum χ^2 . One has to be aware that this procedure is sensitive to the value of the integral determined on the basis of the fit of the distribution. For some bins the agreement is better for pions + kaons and becomes worse when the protons are added as compared with a neighbor bin where the overall

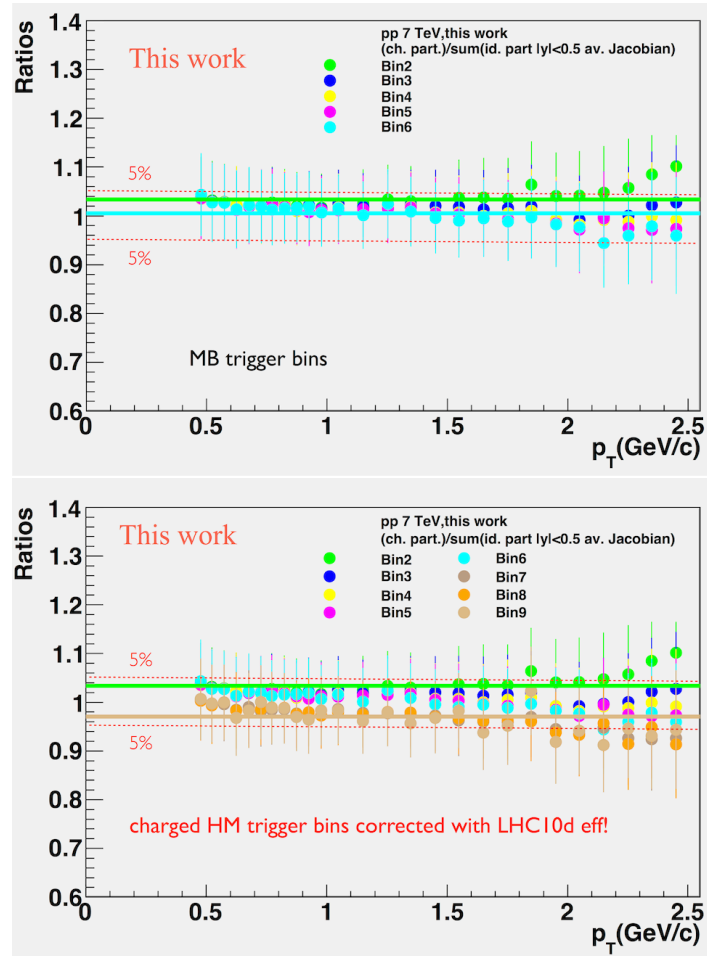


Figure 9.4: The summed p_T distributions for identified charged hadrons compared with the charged particles spectra in all multiplicity bins; includes data from [74].

agreement is better but worse for pions + kaons. That is why in some cases two possible comparisons have been considered. In Fig. 9.5 are presented the ratios between the ALICE and CMS distributions for π^+ , K^+ and p for the one or two multiplicity bins that give a satisfactory value for χ^2 . The pions are represented by the red symbols, kaons by black and protons by green. In the case of the multiplicity bins where two close matches, in terms of χ^2 , were found, the ratio to the lower multiplicity bin from CMS is represented by full circles and the one to the higher multiplicity bin from CMS is represented by the full triangles. Apart from a deviation from 1 of the ratios in several cases, the agreement between the shapes of the p_T distributions is quite good.

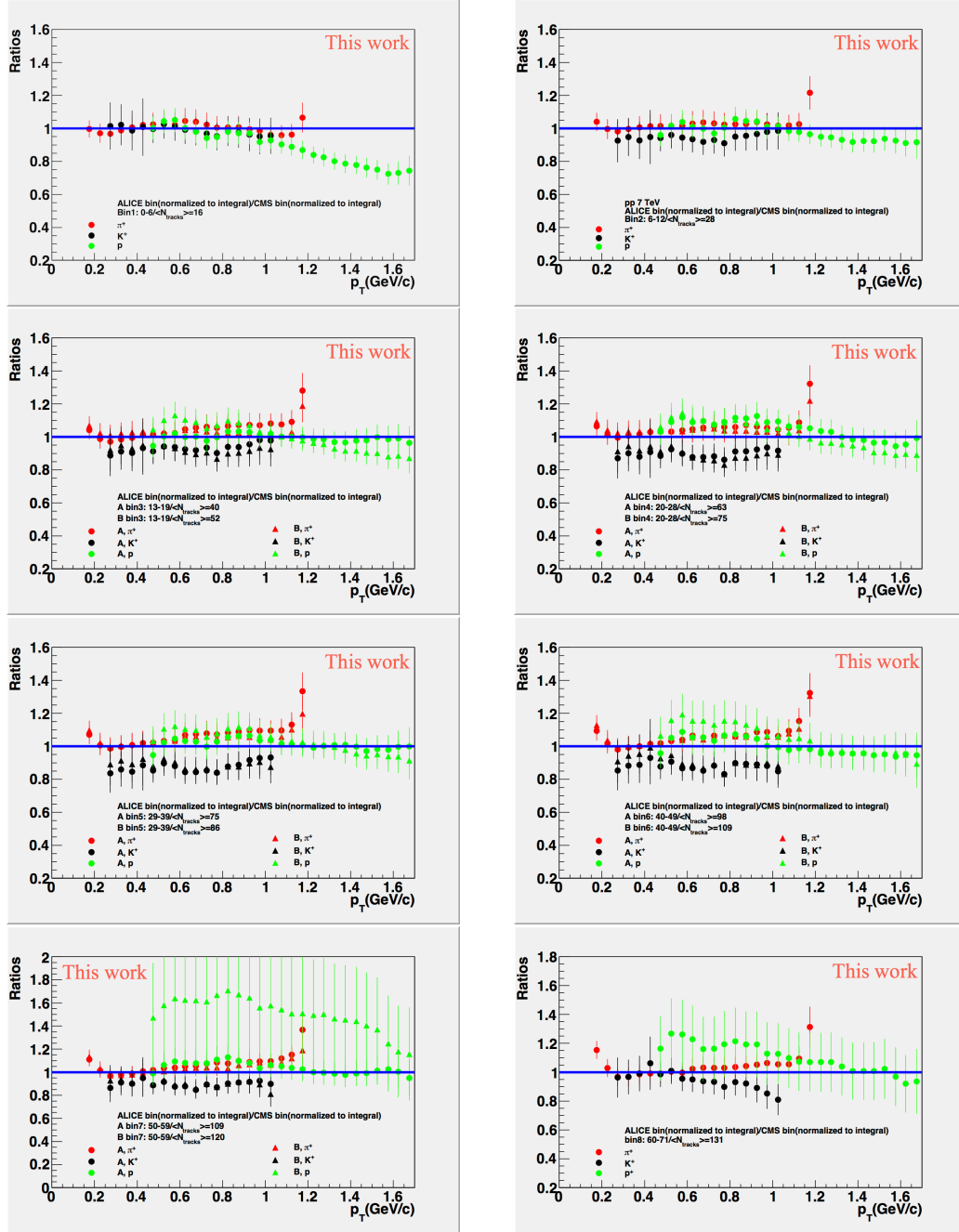


Figure 9.5: Ratio between ALICE and CMS p_T distributions normalized to integral, for ALICE multiplicity bins 0-6, 7-12, 13-19, 20-28, 29-39, 40-49, 50-59 and 60-71 [76]; includes data from [75].

9.3 p_T spectra as a function of multiplicity

Based on these exhaustive crosschecks the fully corrected p_T spectra for pions, kaons and protons were obtained by selecting events in six multiplicity bins: 0-6, 7-12, 13-19, 20-28, 29-39 and 40-49, using the MB trigger. In addition, by using the hardware high multiplicity trigger (HM) three more multiplicity bins were obtained: 50-59, 60-71 and 72-82.

In Fig. 9.6 the multiplicity >0 spectrum, this time normalized to the number of analyzed events, is compared with the p_T spectra in eight multiplicity bins. The lowest multiplicity bin was discarded because of the fact that, in events with a very low number of particles, the TOF based procedure of determining the start time (see Chapter 6) of the event has a very low resolution. This can have a negative impact on the results of the PID procedure and it is more obvious for the case of the high p_T kaons as it can be observed from the Monte-Carlo closure test (Fig. 7.15).

In the bottom row of this figure are represented the ratios of p_T distributions at a given multiplicity relative to the mult >0 case. Besides the lowest multiplicity bins, one could observe a systematic change in the spectra shape, i.e. a depletion in the low p_T region and a trend of leveling off at p_T values larger than 1.5 GeV/c. The observed depletion clearly depends on the mass of the species and multiplicity: it is enhanced going from pions to protons and increasing multiplicity for a given mass.

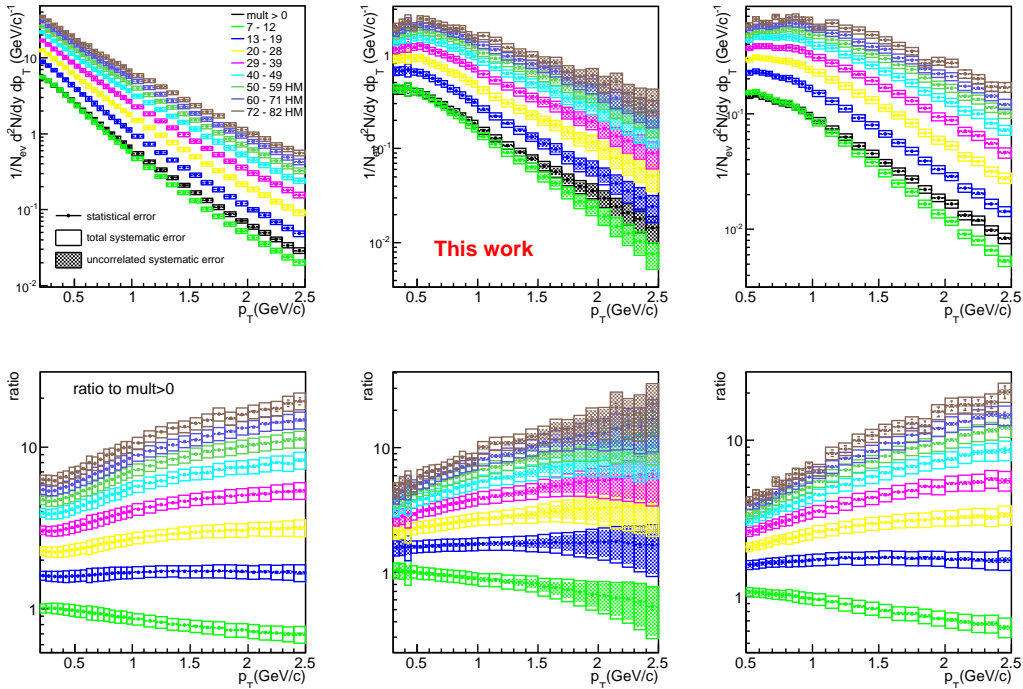


Figure 9.6: The fully corrected spectra in different multiplicity bins.

In order to cross check that the hardware high multiplicity trigger does not influence the results of the present analysis, besides the ratios between the multiplicity distributions with MB and HM triggers presented in Fig. 5.6, we analyzed the highest multiplicity bins for events obtained with the two triggers. The results are presented in Fig. 9.7. The upper row shows the p_T spectra for the last three bins of multiplicity for events with MB trigger (full symbols) and for events with HM trigger (open symbols), while the bottom row show their ratios, bin wise.

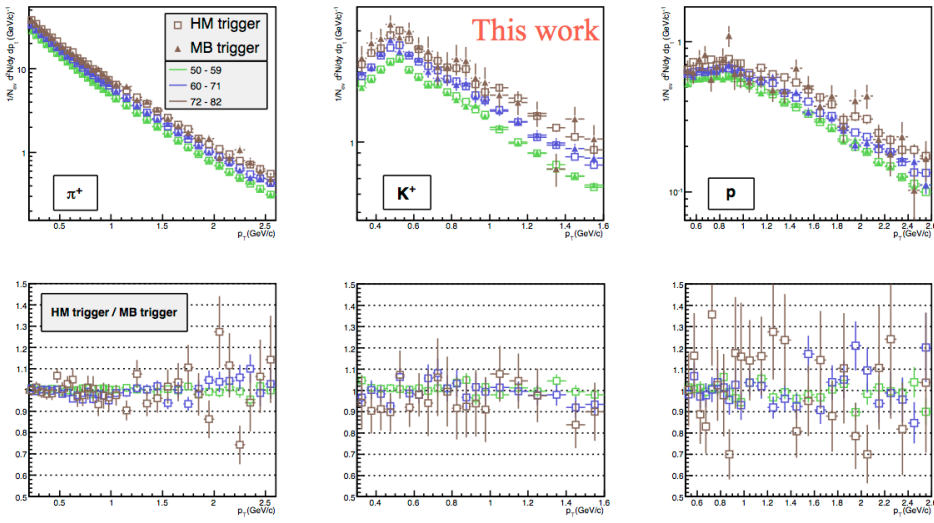


Figure 9.7: Comparison of the spectra obtained with the 2 trigger settings.

As expected, for MB trigger these very high multiplicity bins have quite a modest statistics. However, the general trends from Fig. 9.7 show a very good agreement between the p_T spectra obtained using MB and those obtained using HM hardware trigger for the last three multiplicity bins. This result shows that above a combined multiplicity of 49, the hardware HM trigger works very well, no bias of the experimental results being observed.

The quantitative support for the above statement is based on the results of fitting the ratios with a zero degree polynomial function. The results of that fit is summarized below:

- pions: 0.995 ± 0.008 with $\chi^2/NDF = 1.02$
- kaons: 0.933 ± 0.028 with $\chi^2/NDF = 0.686$
- protons: 0.936 ± 0.033 with $\chi^2/NDF = 1.003$

The K^+/π^+ , p/π^+ and p/K^+ ratios for all the multiplicity bins were also obtained and are plotted in Fig. 9.8. The general trends observed in the p_T distributions as a function of multiplicity and their ratios relative to the MB case presented in Fig. 9.6 can be seen in a more quantitative way in these

representations.

The observed depletion in p/π^+ and p/K^+ at low p_T , increasing with the multiplicity and decreasing towards 1.5 GeV/c looks very much similar with the trend observed in A + A collisions, the heavier particles being pushed towards larger transverse momenta. Such behavior was observed in heavy ion collisions, and especially in measurements of the ALICE collaboration in Pb-Pb collisions at 2.76 TeV, where it was attributed to the existence of collective transverse flow [77].

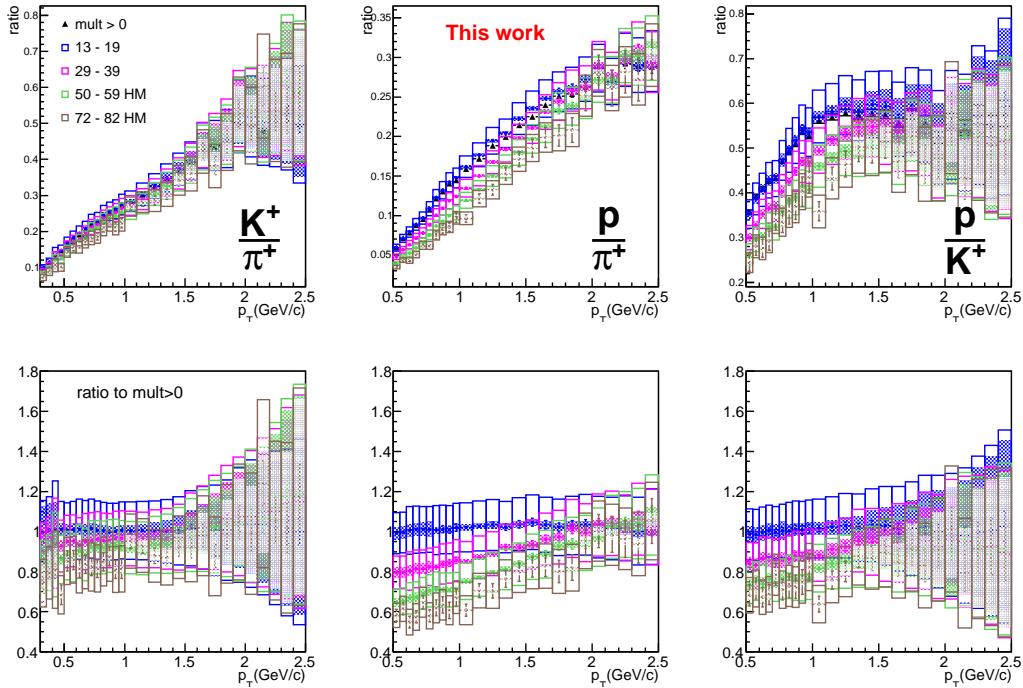


Figure 9.8: p_T dependence of particle ratios for different multiplicity bins.

9.4 Comparison with models predictions

A comparison between experimental p_T spectra and predictions from PYTHIA [78] and HIJING/ $\overline{\text{BB}}$ v2.0 [79] for MB and two multiplicity bins available for the moment from HIJING [80], is presented in Fig. 9.9. A quantitative comparison between experimental data and the predictions of the two theoretical models are presented in terms of ratios of p_T spectra at different multiplicity bins relative to MB is presented in the next Section.

For an easier quantitative comparison of the experimental data and predictions of the two considered models, in Fig. 9.10 are represented the particle ratios as a function of p_T for MB and the two multiplicity bins mentioned above.

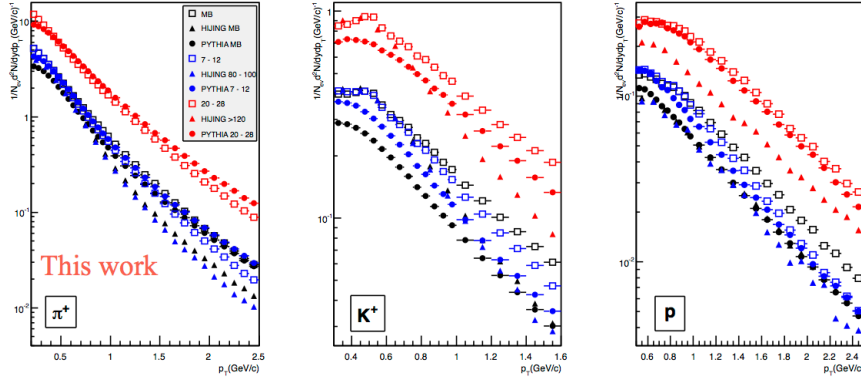


Figure 9.9: Comparison with predictions from PYTHIA and HIJING models; includes data from [80].

Rather significant discrepancy is evidenced for all three ratios between experimental data and the predictions of the two models. The difference is increasing with p_T . If for p/π^+ there is a rather good agreement especially between HIJING and data up to 0.9 GeV/c, a strong underestimation and overestimation for PYTHIA and HIJING respectively starts to develop above 0.9 GeV/c.

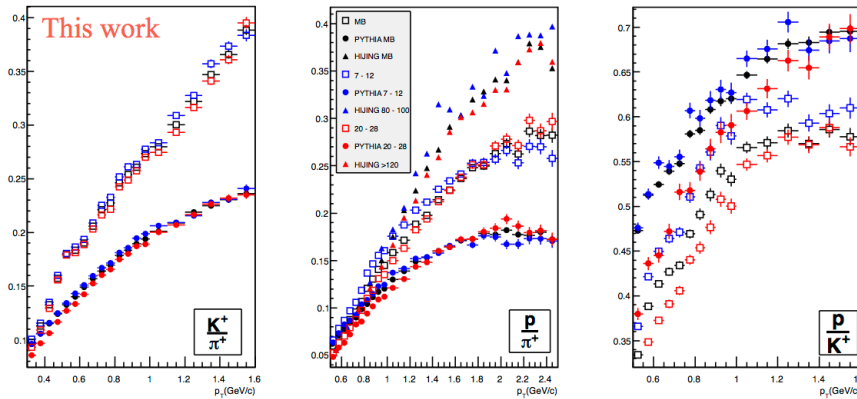
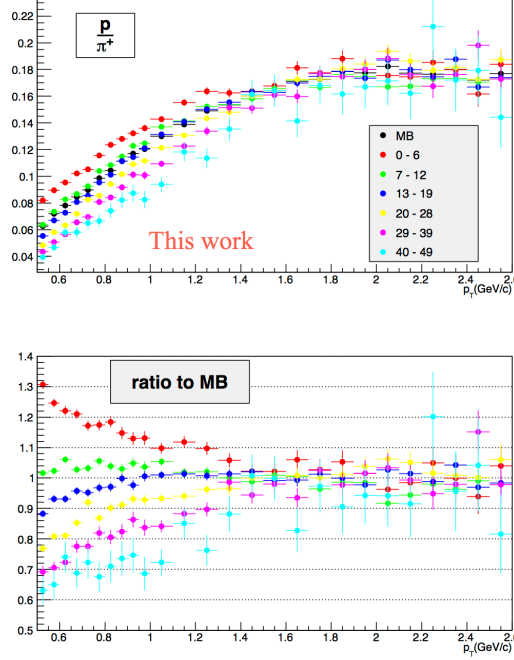


Figure 9.10: Comparison with predictions from PYTHIA and HIJING models; includes data from [80].

As it can be seen in Fig. 9.11, for p/π^+ , qualitatively similar behavior is predicted by PYTHIA. Although the present statistics is not sufficient to access the highest 3 multiplicity bins it seems that in the model all ratios presented in Fig. 9.11 converge towards 1 at about 1.5 GeV/c while for the experimental data this seems to happen rather close to 2 GeV/c.

Figure 9.11: p/π^+ ratio for PYTHIA in all multiplicity bins.

9.5 $\langle p_T \rangle$ and particle ratios multiplicity dependence

In order to extract from the experimental data the average p_T values an extrapolation of measured p_T spectra in the unmeasured p_T regions is necessary. This is done usually by fitting the experimental p_T distributions with different expressions, generally inspired by different phenomenological models. The best fits are then used to extrapolate the measured p_T distributions. In the present analysis three expressions were used, i.e.:

Levy-Tsallis [81] :

$$\frac{d^2N}{dp_T d\eta} = p_T \frac{dN}{d\eta} \frac{(n-1)(n-2)}{nC(nC + m_0(n-2))} \left(1 + \frac{m_T - m_0}{nC}\right)^{-n} \quad (9.1)$$

Modified Hagedorn [28]:

$$\frac{1}{2\pi p_T} \frac{d^2N}{dp_T dy} \sim \frac{p_T}{m_T} \left(1 + \frac{p_T}{p_0}\right)^{-n} \quad (9.2)$$

A. Bylinkin et al. [82]:

$$\frac{d\sigma}{p_T dp_T} = A_e \exp(-E_T^{kin}/T_e) + \frac{A}{\left(1 + \frac{p_T^2}{T^2 \cdot n}\right)^n} \quad (9.3)$$

The three above expressions were tested in order to decide which one gives the best fit of the experimental identified charged particle distributions for the 9 multiplicity bins and MB. The used fit ranges were: p_T between 0.17 and 2.6 GeV/C for π^+ , between 0.25 and 2.6 GeV/c for K^+ and between 0.45 and 2.6 GeV/c for p, respectively.

Each p_T distribution for a given multiplicity bin was fitted separately. The combination between the statistical and systematic errors was taken into account. Based on the results obtained previously [83, 84] one can conclude that the best fit quality is obtained using the expression proposed by A. Bylinkin et al.[82], which is a combination of an exponential and a power law function. The fit quality is quite good up to larger p_T values relative to what is used in the present analysis for all multiplicity bins. Thus, for the extrapolation of p_T spectra of charged identified hadrons and for estimating the multiplicity dependent average p_T and yield values the expression 9.3 was used.

The final $\langle p_T \rangle$ values for pions, kaons and protons, based on the measured p_T spectra in the same p_T range used for the fit and extrapolated at lower p_T values down to zero and at higher p_T values up to 10 GeV/c using expression 9.3 with the parameters fixed by the fits are presented in Fig. 9.12 left as a function of multiplicity. The multiplicity represents the mean multiplicity value in the analyzed multiplicity bin.

Based on the extrapolations in the unmeasured regions it is possible to access also the absolute yield values for pions, kaons and protons and thus their ratios, as a function of multiplicity. In the right side of Fig. 9.12 are represented the yield ratios as a function of multiplicity.

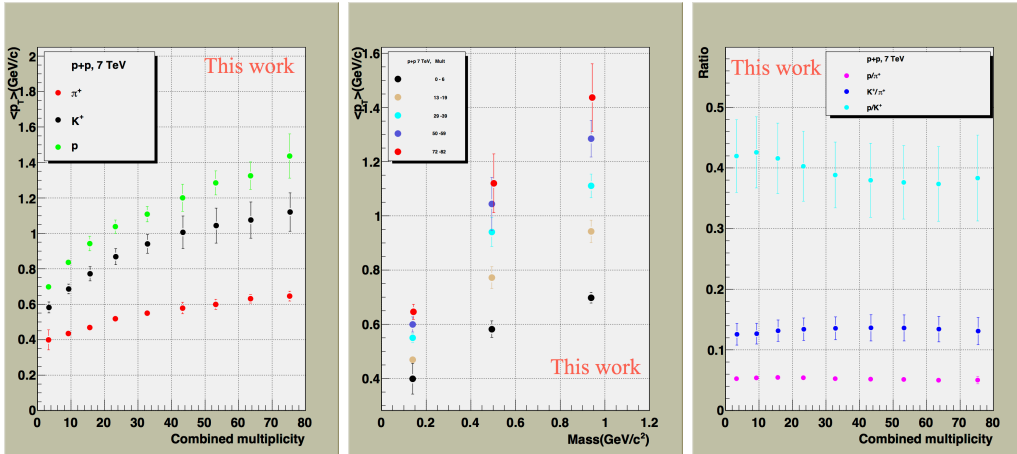


Figure 9.12: $\langle p_T \rangle$ (left) and yields ratios(right) as a function of multiplicity. $\langle p_T \rangle$ as a function of mass in all multiplicity bins (middle) [83].

In the middle of Fig. 9.12 are represented the $\langle p_T \rangle$ as a function of mass for every second multiplicity bin.

In all these figures the final errors are obtained by assuming that errors of the

p_T distribution function in the extrapolated zones are given by the difference between the lowest and the highest value of the p_T distributions estimated with the best fit parameters in the case of all three formulas. In addition, on the measured p_T range the errors were estimated as the difference in $\langle p_T \rangle$ obtained when fitting two extreme p_T distributions built as data plus/minus the corresponding error, point by point.

A continuous increase of the slope of $\langle p_T \rangle$ versus mass can be observed for the first six multiplicity bins followed by a saturation tendency for the very last three multiplicity bins.

The fits of p_T spectra with other type of expressions, a systematic study of the obtained fit parameters as a function of multiplicity and comparison with the values extracted from similar fits for A+A collisions is in progress.

In Fig. 9.13 a comparison between the $\langle p_T \rangle$ values of this analysis and the ones obtained in an independent analysis within ALICE Collaboration [70] for MB, is presented. Within the error bars, the values obtained from these two independent analyses that are based on two different PID methods, are the same [84].

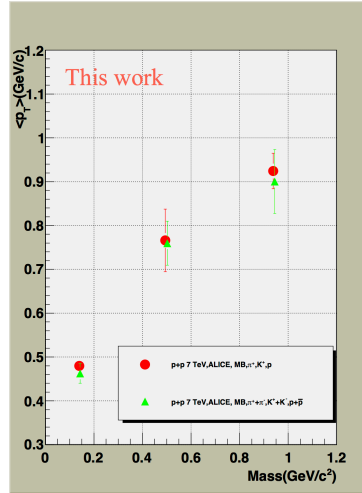


Figure 9.13: $\langle p_T \rangle$ as a function of mass for MB obtained in an independent analysis within ALICE Collaboration and in the present analysis, respectively [83]; includes data from [70].

Although the Boltzmann-Gibbs Blast Wave (BGBW) expression:

$$Ed^3N/dp^3 \sim \int_0^R r dr m_T K_1(m_T \cosh \rho/T) I_0(p_T \sinh \rho/T) \quad (9.4)$$

where:

$$m_T = \sqrt{m^2 + p_T^2} \quad \beta_r(r) = \beta_s \left(\frac{r}{R} \right)^n \quad \rho = \tanh^{-1} \beta_r \quad (9.5)$$

is not able to perform a good simultaneous fit of pions, kaons and protons p_T spectra [58], in order to have a comparison with the parameters of similar fits done for Pb+Pb collisions at 2.76 TeV [85], this exercise was done also for the p_T spectra obtained in this analysis for the 9 combined multiplicity bins.

The p_T ranges for the fits were chosen in order to be similar with the ones used in the ALICE Collaboration for Pb+Pb and p+Pb analysis, i.e. 0.5-1 GeV/c for pions, 0.3-1.5 GeV/c for kaons and 0.5-2.0 GeV/c for protons. These ranges are slightly different as those used initially for Pb+Pb published data (see Fig. 9.17) but the conclusions remain unchanged. All the three species were fitted simultaneously with n (Eq. 9.5) as a free parameter.

The fit quality can be seen in Fig. 9.14 in terms of Data/Fit ratios as a function of p_T for all 9 combined multiplicity classes.

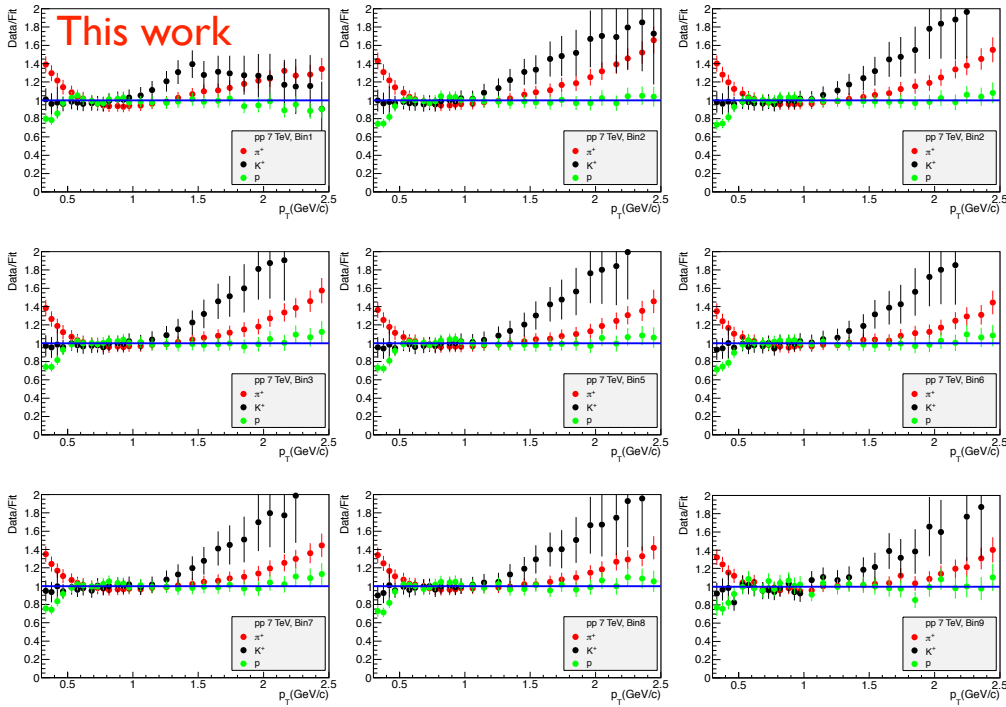


Figure 9.14: Quality of the simultaneous fit with BGBW, of π^+ , K^+ , p p_T distributions, for pp data, present analysis, as a function of multiplicity [83].

As expected, the quality is rather modest. For protons it works rather well in all multiplicity bins, for pions it improves at high multiplicity bins while for kaons the fit quality is rather modest and multiplicity independent above 1.4 GeV/c. The fit quality slightly improves with the increase of the multiplicity and for the highest multiplicity it reaches a rather similar quality as the one obtained for the fits of the most central Pb+Pb collisions. The evolution of

the obtained ($T_{fo}, \langle \beta \rangle$) values as a function of multiplicity can be seen in Fig. 9.16. The same dependence obtained by the ALICE Collaboration in Pb+Pb collisions at 2.76 TeV is plotted in Fig. 9.17. The same exercise was done on MC simulations with Pythia 6.4 for the 9 multiplicity bins. In contrast with the experimental trend, for PYTHIA the fit quality seems to be better for lower multiplicity bins Fig. 9.15. The Pythia ($T_{fo}, \langle \beta \rangle$) within the error bars show the same dynamics in $\langle \beta \rangle$, while T_{fo} remains almost constant. The origin of the observed similarities and differences between the data and PYTHIA model remains to be studied in terms of other observables behavior.

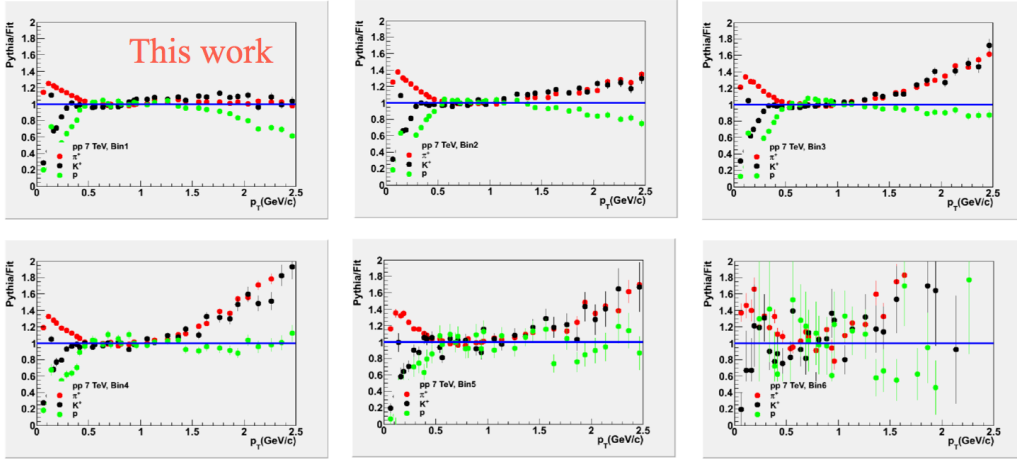


Figure 9.15: Quality of the simultaneous fit with BGBW, of π^+ , K^+ , p p_T distributions, for PYTHIA 6.4 simulations, as a function of multiplicity [83].

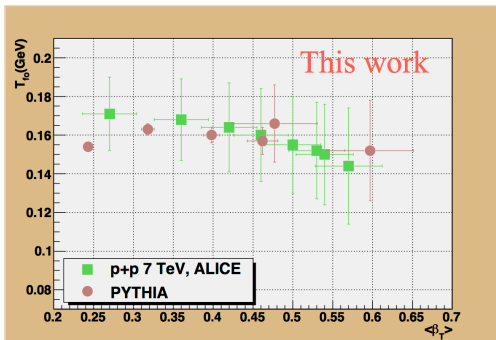


Figure 9.16: Evolution of ($T, \langle \beta \rangle$) values as a function of multiplicity obtained in pp collisions at 7 TeV using this analysis [83].

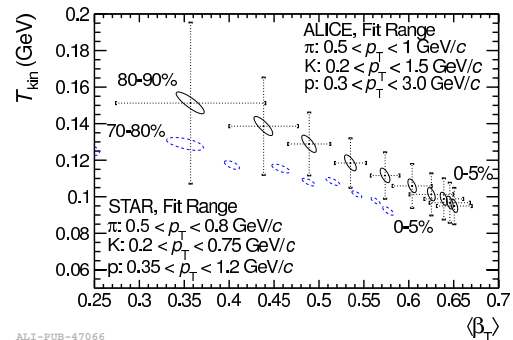


Figure 9.17: Evolution of ($T, \langle \beta \rangle$) values as a function of multiplicity obtained in Pb+Pb collisions at 2.76 TeV by the ALICE Collaboration [85].

Chapter 10

Azimuthally symmetric events

As it was shown in Section 3.2, events with high azimuthal isotropy are of a special interest for this analysis. In order to estimate the degree of azimuthal isotropy the global observable *directivity* was used [86]. This observable is defined as:

$$D^{\pm} = \frac{|\sum_i \vec{p}_t^i|}{\sum_i |\vec{p}_t^i|} \Big|_{\eta^{pos/neg}}, \quad (10.1)$$

As it can be seen from the formula, the events with a high azimuthal isotropy will have a low directivity. For events dominated by jets the directivity increases towards 1.

The two dimensional directivity (computed as the mean of D^+ and D^-) versus multiplicity representation is shown in Fig. 10.1.

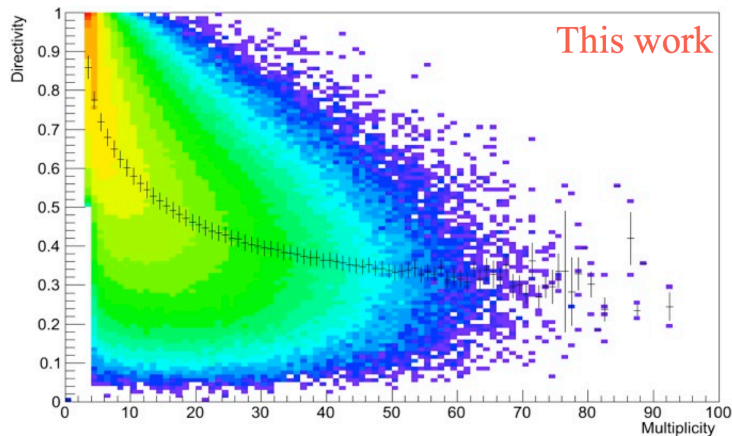


Figure 10.1: Two dimensional directivity (mean of D^+ and D^-) versus combined multiplicity.

A $d^2N/\Delta\varphi\Delta\eta$ two dimensional representation for minimum bias and multiplicity >30 & directivity <0.3 , where $\Delta\varphi$ and $\Delta\eta$ represent the difference in pseudo-rapidity and azimuthal angle between a given identified charged hadron and the leading particle in the respective event, can be used in order to evaluate the performance of the estimation (Fig. 10.2 and 10.3).

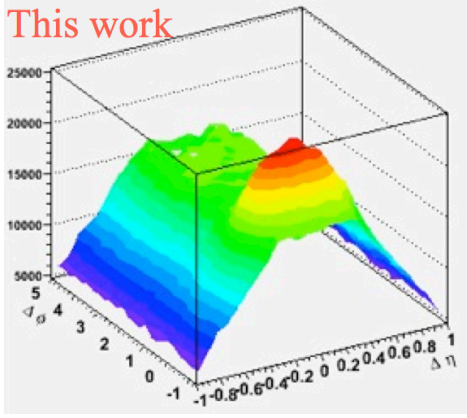


Figure 10.2: Two dimensional $d^2N/\Delta\varphi\Delta\eta$ representation for the minimum bias case.

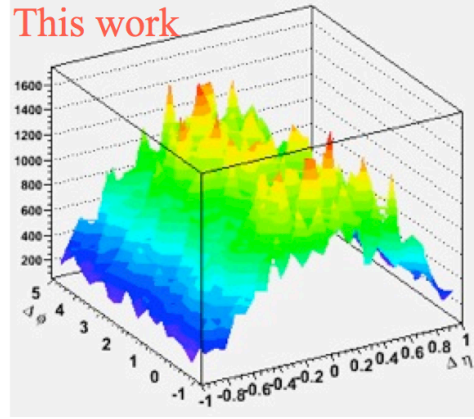


Figure 10.3: Two dimensional $d^2N/\Delta\varphi\Delta\eta$ representation for $M > 30$ & $D < 0.3$.

Even without extracting the background correlation one could observe, comparing the two distributions, that high multiplicity and low directivity cut removes the jet-like correlation observed in the minimum bias case [87].

In the case of the selections using the events multiplicity based on the combined multiplicity estimator, there is no dependence of the corrections as a function of multiplicity (Section 7.5). When on top of the multiplicity selection an extra cut using the event directivity is applied this is no longer the case.

For the low multiplicity bins the corrections described in Chapter 7 show a strong variation with the directivity of the considered events. However, as the multiplicity increases this dependence becomes smaller very fast. For a combined multiplicity above 40 this variation is below 3%. Consequently, as in the case of the spectra in multiplicity bins, the MB determined corrections were used also for the spectra in directivity bins, only for events with multiplicity above 40.

The mentioned 3% variation for the tracking, matching, PID efficiency and percentage of misidentified particles was included in the systematic errors.

For this analysis three directivity ranges were established: directivity lower than 0.3, 0.3 to 0.6 and 0.6 to 0.9. In order to consider an event to be in one of the above mentioned directivity classes both D^+ and D^- have to fulfill simultaneously the imposed condition. A visual representation of the selected events in terms of mean directivity and combined multiplicity is shown in Fig. 10.4, where only events for which the simultaneous D^+ and D^- condition was fulfilled. This procedure selects samples with high purity but it decreases considerably the available statistics.

In Fig. 10.5 the p_T spectra for the highest four multiplicity bins and the three directivity classes are plotted. As it can be seen, for the high directivity class the available statistics is very low. The statistical errors, total systematic errors and the systematic errors related with the multiplicity and directivity

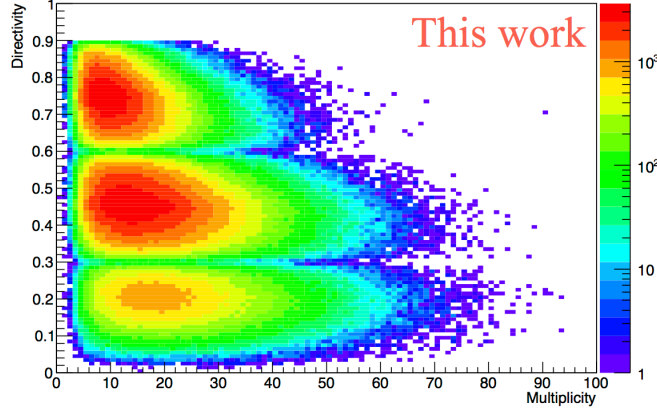


Figure 10.4: Two dimensional directivity (mean) versus combined multiplicity - filled only when simultaneous D^+ and D^- condition was fulfilled.

selections are plotted separately as in the case of the p_T spectra as a function of multiplicity.

The change of the shape of the p_T spectra can be easier followed in Fig. 10.6 where the ratio of the spectra of all the three directivity classes to the spectra in the respective multiplicity bin is plotted.

In low directivity events (red symbols) an enhancement of the low p_T region and a depletion of the high p_T can be observed, relative to the corresponding multiplicity selected spectra. For the high directivity events (blue symbols) the behavior of the spectra mirrors the one for the low directivity events, being much harder. As expected, spectra obtained by using the medium directivity selection (green symbols) is very similar with the spectra in the corresponding multiplicity bins.

For the multiplicity bin 50 - 59 where the statistical fluctuations are reasonably low, the three directivity classes were plotted separately (Fig. 10.7). In this representation it can be seen that the crossing point between the enhancement at low p_T and the depletion at high p_T (for the low directivity bin) moves towards a higher p_T value with the increase of the mass of the considered particle, being around 1.6 GeV/c for pions and above 2.2 GeV/c for protons.

The behavior of the p_T spectra in the three directivity classes as a function of multiplicity is shown in Fig. 10.8. A clear change in the spectra shapes for all three species is evidenced going from large directivity values towards low values specific for less jetty events. While for pions the change is from exponential plus power law shape to exponential one, for kaons and protons a transition from exponential shape to a concave one with maxima at ~ 0.6 GeV/c and $0.8 - 0.9$ GeV/c, respectively, is observed. Fits with BGBW of the type presented in Section 9.5 in order to obtain quantitative arguments for the origin of this behaviors are in progress.

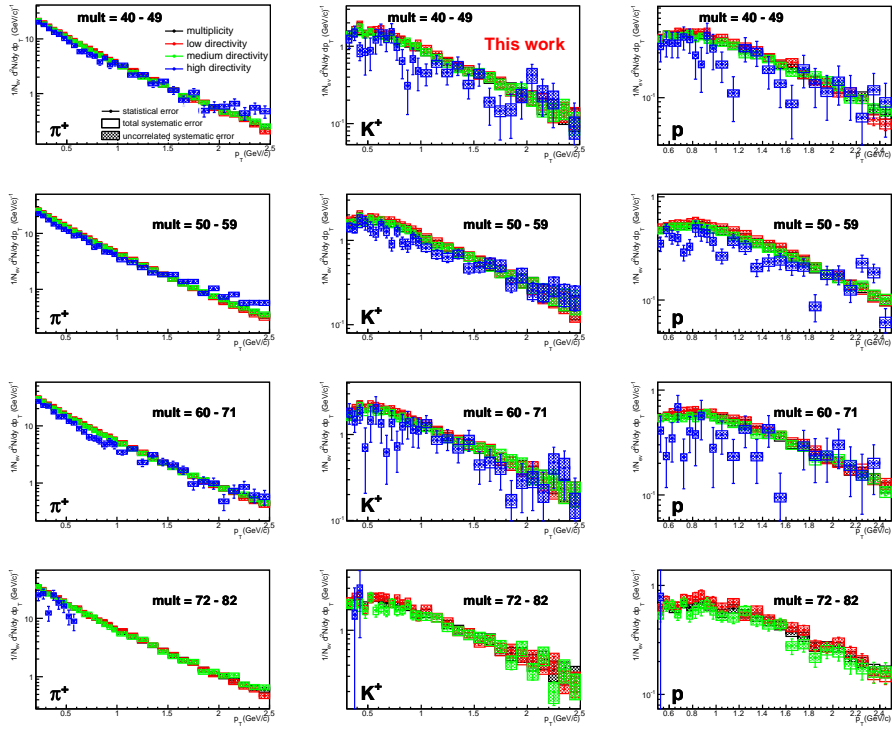


Figure 10.5: p_T spectra as a function of directivity in the highest four multiplicity bins.

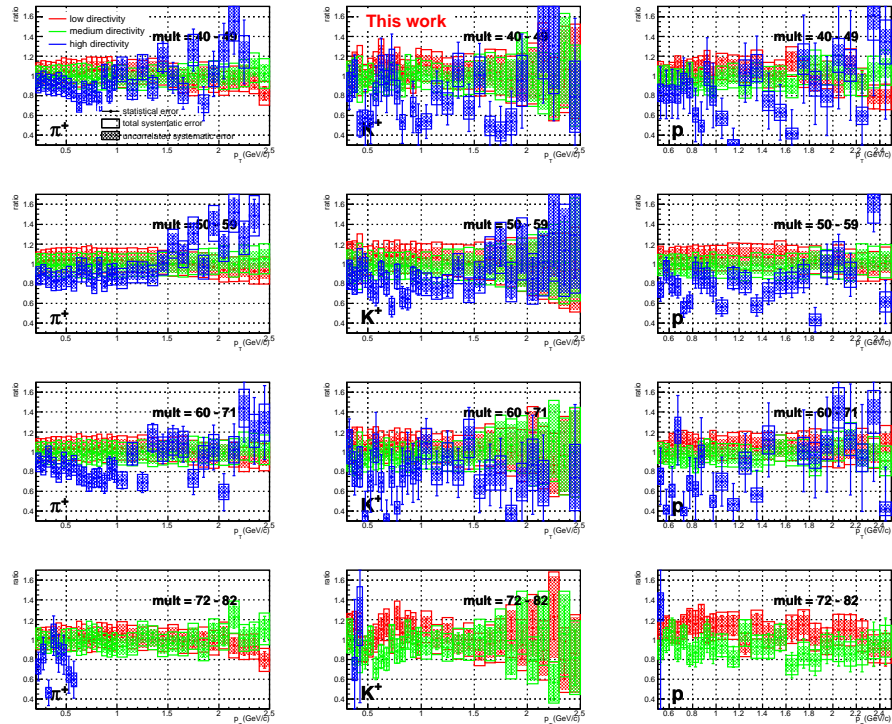


Figure 10.6: ratio of the p_T spectra as a function of directivity relative to the spectra in the corresponding multiplicity bin.

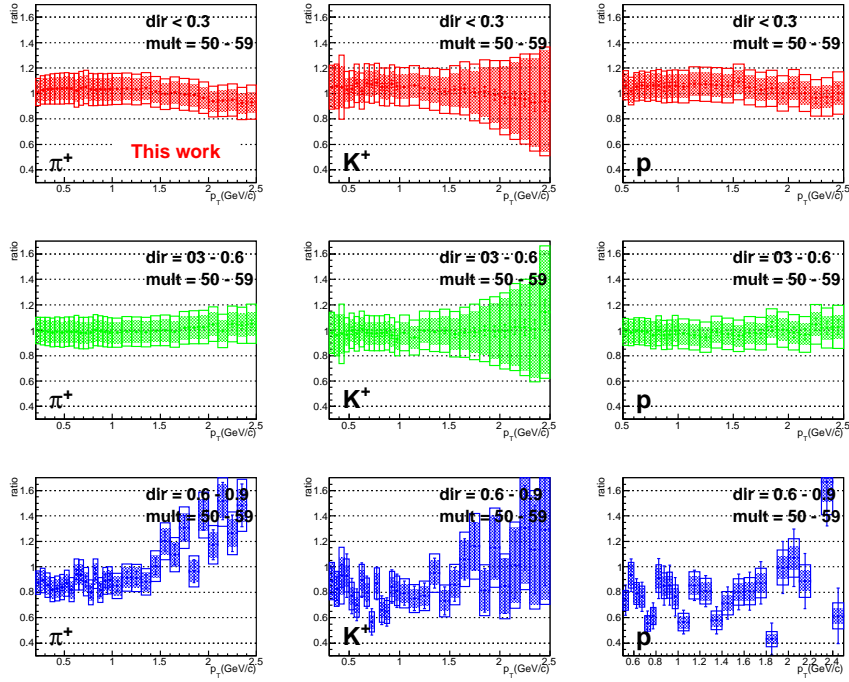


Figure 10.7: p_T spectra as a function of directivity in the 50 - 59 multiplicity bin, plotted separately.

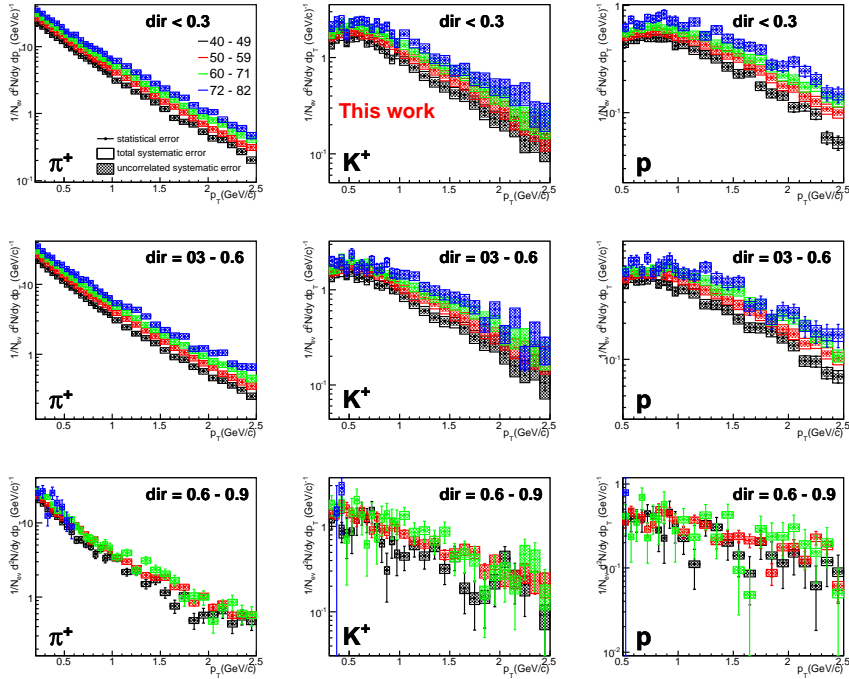


Figure 10.8: p_T spectra as a function of multiplicity in all the three directivity classes.

Chapter 11

Conclusions

The studies described in this thesis and their physics motivation were presented in more than 40 ALICE meetings (Physics Analysis Group, Physics Working Group, Physics Forum and ALICE Physics Weeks) over the last 4 years, and were extensively described in 7 ALICE internal notes. The analysis became mature and it was accepted by the ALICE Collaboration.

Experimental data obtained with the ALICE Experiment in 7 TeV pp collision were analyzed and the p_T spectra for positive identified charged particles as a function of multiplicity, in a rather large range of p_T relative to other LHC experiments were obtained, based on robust corrections, cross-checks, and error estimates.

Following detailed studies of the fit quality using different expressions for p_T distributions generally inspired by phenomenological models, accurate $\langle p_T \rangle$, particle yields and particle yields ratios as a function of multiplicity were obtained.

The p_T spectra shapes, their ratio relative to the MB spectrum, the p_T dependent yield ratios and their ratio relative to MB, as well as $\langle p_T \rangle$ as a function of particle mass evolution as a function of multiplicity show similar trends as those studied in A+A collisions at RHIC or LHC energies.

Fits of p_T spectra with Boltzmann-Gibbs Blast Wave expression show a similar fit quality as in the case of Pb+Pb collision at 2.76 TeV at large multiplicities and the freeze-out temperature (T_{fo}) and expansion velocity ($\langle \beta \rangle$) obtained as free parameters from these fits as function of multiplicity have similar trends as the ones obtained in Pb+Pb collisions at 2.76 TeV.

Preliminary results using, besides multiplicity selection, the event shape selection, show that for events close to azimuthal isotropy, the trends mentioned above are enhanced.

These type of studies will continue, they will be correlated with the results of other analyses, especially those from particle correlations, compared in details with the theory predictions in order to have unambiguous understanding of the origin of the observed trends.

However, at present, these results seem to confirm the expectations based on theoretical considerations, presented in Chapter 2, that at this energy,

even in p+p collisions, deconfined matter at high energy density is produced and its dynamics in the final phase resembles the trends observed in A+A collisions.

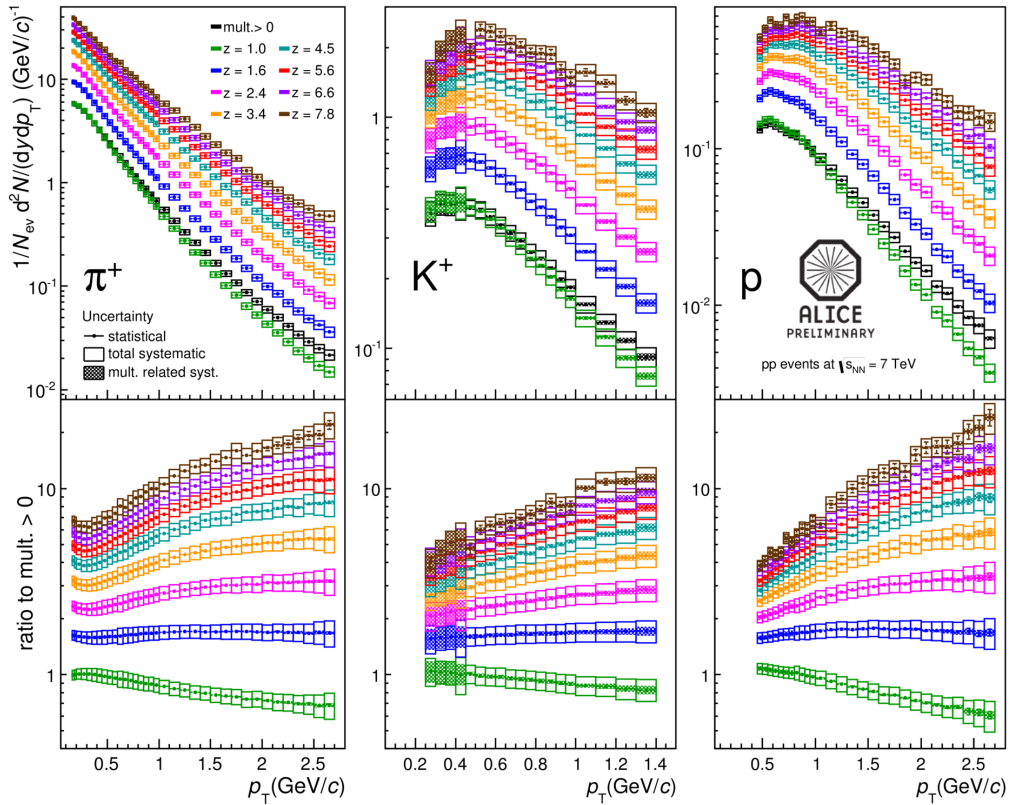
Addendum: *Preliminary* ALICE plots

Very recently the results of the present analysis were approved as *Preliminary* by the ALICE Collaboration. These results are presented in Fig 11.1 and 11.2.

In these plots the bins were labeled not as in Fig 9.6 with the combined multiplicity bin limits but using the observable z defined below:

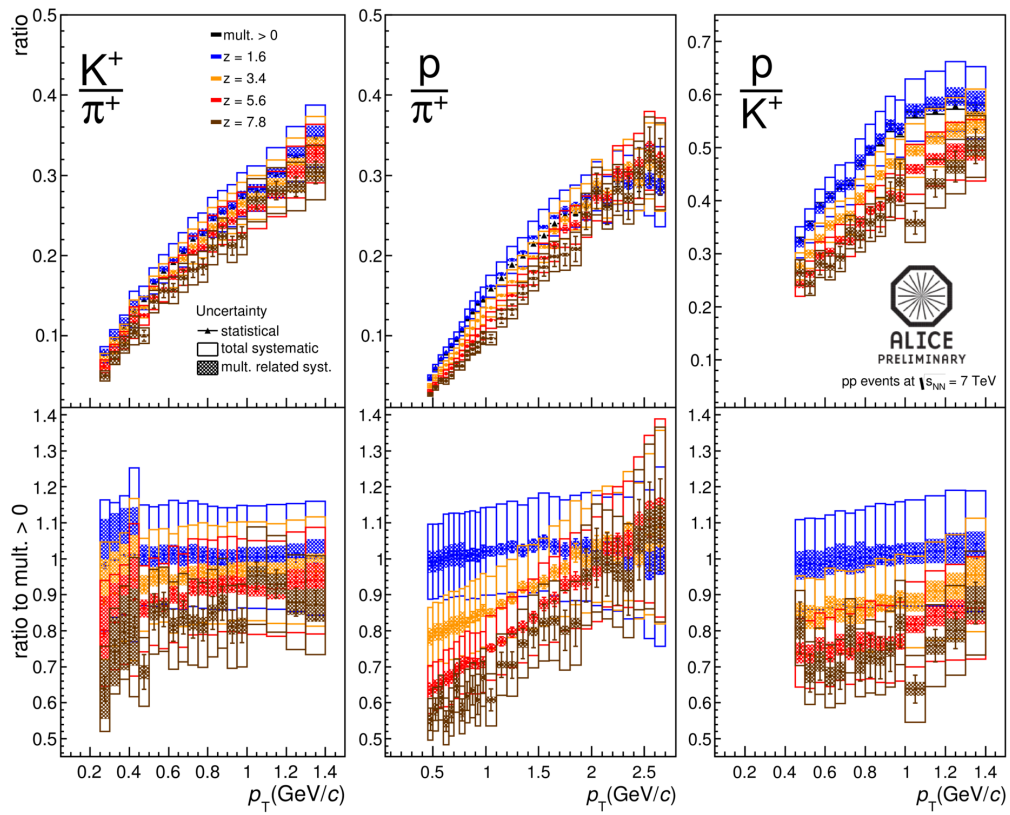
$$z = \frac{\left\langle \frac{dN}{d\eta} \right\rangle_{curr.bin}}{\left\langle \frac{dN}{d\eta} \right\rangle_{mult>0}}$$

The p_T range of the kaons spectra was restricted to 1.4 GeV/c due to the discrepancy shown in Fig. 9.1. Further investigations of the high p_T kaons spectra are presently in progress and the range of the approved plots will be extended once this checks are done.



ALI-PREL-51115

Figure 11.1: Upper row - Multiplicity dependence of the transverse momentum distributions for positive pions, kaons and protons in pp collision at 7 TeV. $z = \langle dN_{ch}/d\eta \rangle_{mult.bin} / \langle dN_{ch}/d\eta \rangle_{mult.>0}$. Bottom row - ratio of transverse momentum distributions in a given multiplicity bin (z) relative to $mult.>0$ - ALICE preliminary.



ALI-PREL-51119

Figure 11.2: Upper row - p_T dependence of the particle ratios K/p , p/π and p/K as a function of multiplicity in pp collisions at 7 TeV. $z = \langle dN_{ch}/d\eta \rangle_{\text{mult. bin}} / \langle dN_{ch}/d\eta \rangle_{\text{mult.} > 0}$. Bottom row - the ratio of the upper distributions relative to the one for $\text{mult.} > 0$ - ALICE preliminary.

Appendix A: Analysis Task Schema

A schematic view of the analysis software is presented in the following section. In this way is easy to see how the uncorrected p_T spectra are obtained and how each of the necessary corrections are determined.

All the selections criteria that reject events or tracks are represented in red. A dark green text marks the position where a container for tracks is filled. The blue color was dedicated to the explanations on how each of the filled containers are used.

In general, a C++ syntax was used in order to retain a resemblance with the original AliRoot analysis task but, to provide an easy to follow schematic view, this C++ syntax was substantially simplified.

Event LOOP{

trigger condition: may be MB of HM

vertex existence: global tracks of ITS only fallback
vertex position within +/- 10 cm

ESD tracks LOOP{

ALICE standard track cuts 2010

Get ESD PID response

set bMatched (0 = no matching; 1 = successful TOF matching)

PID detector LOOP{

// run PID using the ITS-TPC, TPC and TOF responses
// it generates 3 independent p_T spectra

if(yESD < 0.5){

if((Detector < 2) || (bMatched)) { // TOF matching needed only for

Detector=2 (TOF)

switch(PID response){
// all ESD tracks => hRaw[i] i = 0 (pi), 1(K), 2(pr)
Fill hRaw[particle]
}

}

} // end yESD cut

} // end detector loop

if(fSim){

Get MC PID // this eliminates also fake tracks

if(yMC_PID < 0.5) {

switch(MCpid){
Fill hAllESD[i] // all particles "surviving" the pass through the

detector (being successfully reconstructed)

}

// The ratio between hAllESD[i] and hGen[i] gives the Tracking efficiency

if(track does NOT come from IsPhysicalPrimary) continue;

// IsPhysicalPrimary = generated particles + particles coming from

resonance decay

switch(MCpid){
Fill hPrimary[i]; // all primary particles

}

// The ratio between hPrimary[i] and hAllESD[i] gives the FeedException

correction (for MC based correction and cross-check)

// The ratio between hPrimary[i] and hGen[i] gives the (Tracking - feedException

efficiency

```

} // end yMC cut

switch(MCpid){ // with NO y cut
    Fill hNotMatched[i]
}

if( isMatched ) {

    switch(MCpid){
        Fill hMatched[i]; // ONLY for Barbara's recipe (no Y cut for matching)
    }

    if ( | yMCPID | < 0.5){

        switch(MCpid){
            Fill hMatchedY[i]; // all particles with y cut and TOF matching
        }

        } // end yMCPID if
        // The ratio between hMatchedY[i] and hAllESD[i] gives the Matching
efficiency

    } // end isMatched if

    if(yESD > 0.5) continue;

    PID detector LOOP{
        // get individual contaminations
        Fill hCont[particle][contamination]
        // The ratio between Sum of hCont[ i ][ j != i ] (wrong identified) and { Sum of
hCont[ i ][ j != i ] (wrong identified) + hCont[i][i] (correctly identified)} gives the contamination correction

        if(ESDpid == MCpid){

            // correctly identified tracks =>hTrue[i]
            switch(ESDpid){
                Fill hTrue[i]
            }
        }
        // The ratio between hTrue[particle] and hMatchedY[particle] (for TOF) OR
hAllESD[particle] (for ITS & TPC) gives the PID correction

    } // end PID detector LOOP

} // end if fSim

} // end track loop

MC tracks loop{

    Make |yMCI| < 0.5 cut

    if(IsPhysicalPrimary){
        Fill hGen[i]
    }
} // end MC tracks loop

} // end UserExec()

```

Appendix B: ALICE Coordinate System

“The ALICE coordinate system is a right-handed orthogonal Cartesian system with point of origin $x, y, z = 0$ at the beams interaction point (IP)” [88]. In the figure below the axis of the coordinate system is overlaid on the ALICE experiment schematic view.

The definitions of the axis and angles are:

- x axis: perpendicular to the mean beam direction and horizontal; pointing to the accelerator centre
- y axis: perpendicular to the mean beam direction and to the x axis; pointing upwards
- z axis: parallel to the mean beam direction; pointing away from the muon arm
- azimuthal angle ϕ : increases counter-clockwise from the x axis towards the y axis (looking towards the muon arm)
- polar angle θ : increases from the z axis to the x-y plane

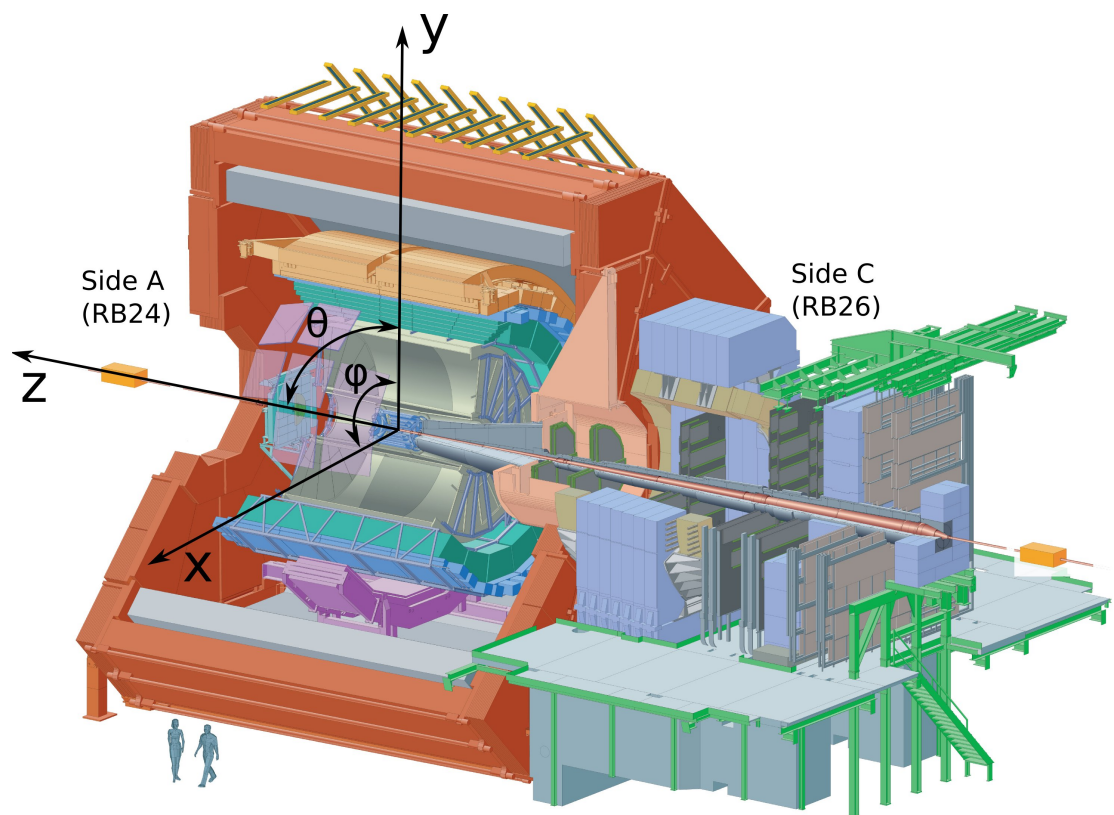


Figure 11.3: ALICE experiment coordinate system [89].

List of Figures

2.1	The running coupling constant as a function of Q [1].	7
2.2	QCD electric screening [2].	7
2.3	QCD color screening [2].	7
2.4	Strongly bound clusters: hadrons (left); Phase transition (middle); Weakly interacting: quarks and gluons (right) [3].	8
2.5	Quark masses in the QCD vacuum and the Higgs vacuum [6].	8
2.6	QCD critical points and phase boundaries [3].	10
2.7	QCD Phase Diagram [7].	10
2.8	Space-time diagram of a collision process [3].	11
2.9	(a) The structure function F in the continuous medium model; (b) The same with the fluctuations taken into account [8]. . .	12
2.10	$b_{i\perp}(x_i)$ trajectory of the cascade [8]	13
2.11	Interaction between partons correlated with the position in the cascade [8]	14
3.1	Overview of the existing and under construction experimental facilities [3].	15
3.2	Elliptic flow as a function of the beam energy [15].	17
3.3	v_2/n_q as a function of E_{k_t}/n_q [17].	17
3.4	p_T distributions for all the identified species [18].	18
3.5	top: T_{kin} as a function of multiplicity and comparison with T_{ch} ; bottom: $\langle \beta \rangle$ as a function of multiplicity [18].	18
3.6	Extracted chemical (open symbols) and kinetic (filled symbols) freeze-out temperatures for central heavy-ion collisions as a function of the collision energy [19].	19
3.7	Average transverse radial flow velocity extracted from the blast-wave model for central heavy-ion collisions as a function of the collision energy [19].	19
3.8	$\langle p_T \rangle$ as a function of mass for p+p, Cu+Cu and Au+Au collisions [20].	20
3.9	$\langle p_T \rangle$ as a function of mass for p+p and Au+Au collisions, compilation of STAR published data [22].	20
3.10	UA5: $\langle p_T \rangle$ of kaons in the central region as a function of c.m. energy [24].	21
3.11	E735: $\langle p_T \rangle$ of π , K and \bar{p} as a function of c.m. energy [25].	21

3.12	$\langle p_T \rangle$ vs. $\ln(s)$ extrapolations [26].	22
3.13	$\langle p_T \rangle$ statistical models [29].	22
3.14	E735: $\langle p_T \rangle$ at 1800 GeV as a function of $\langle dN_c/d\eta \rangle$ [25].	22
3.15	CDF: $\langle p_T \rangle$ at 630 GeV and 1800 GeV as a function of N_{ch} [33].	23
3.16	ALICE: two-pion correlation studies at 0.9 TeV and 7 TeV [34].	23
3.17	Double and triple partonic interactions as a function of $\ln(s)$ [10].	23
4.1	The CERN accelerator chain complex [36].	24
4.2	The ALICE experiment [38].	26
4.3	The Inner Tracking System [40].	27
4.4	Time Projection Chamber [38].	28
4.5	Longitudinal cross-section of the TRD [38].	29
4.6	Cross-section of the ALICE experiment during the 2010 data taking period [43].	29
4.7	Schematic view of a TOF sector [38].	29
4.8	The performance in terms of done jobs for the ALICE GRID sites starting with August 2007; NIHAM is represented by the dark yellow curve [49].	32
4.9	Photo of the NIHAM GRID site data center.	32
5.1	Ratio of the fully corrected p_T obtained with and without the pileup rejection procedure for pions, kaons and protons.	34
5.2	Reconstructed global multiplicity vs generated multiplicity.	37
5.3	Reconstructed combined multiplicity vs generated multiplicity.	37
5.4	Combined multiplicity estimator definition: labeled as "IT-STPC+" in this figure [56].	37
5.5	The method used to determine the correspondence of bin limits between the combined multiplicity estimator ($ \eta < 0.8$) and the generated multiplicity in the CMS acceptance ($ \eta < 2.4$).	39
5.6	The comparison of the MB trigger and of the HM trigger combined multiplicity distributions.	40
6.1	First PID method developed for testing the analysis feasibility.	43
6.2	dE/dx spectrum versus momentum in p+p collisions at $\sqrt{s} = 7\text{TeV}$ using TPC. The lines are a parameterization of the Bethe-Bloch curves [43].	44
6.3	Comparison of 2-sigma inclusive and exclusive PID and the bayesian PID.	45
6.4	TOF measured particle beta vs. momentum measured by TPC in p+p collisions at $\sqrt{s} = 7\text{TeV}$ [43].	46

7.1	Tracking, matching and PID efficiencies and the percentage of misidentified particles. The PID and the misidentified are showed for the TOF.	50
7.2	PID efficiencies and the percentage of misidentified particles for ITS-TPC, TPC and TOF based on PID responses.	52
7.3	Reweighted percentages of misidentified particles.	53
7.4	Monte-Carlo based shapes of the DCA distributions for particles from different sources. The total DCA distribution from data, not normalized, is also included.	54
7.5	The result of the fit of the DCA distributions, for positive pions, in one p_T bin.	55
7.6	Percentage of secondary particles (coming from weak decays and material) as a function of p_T for pions and protons; obtained using the DCA distribution fits on the data (red symbols) and extracted from the MC simulations (blue symbols). For kaons this correction is negligible.	56
7.7	Tracking efficiency as a function of multiplicity.	57
7.8	Matching efficiency as a function of multiplicity.	57
7.9	PID efficiency as a function of multiplicity for TOF.	58
7.10	Misidentified percentage as a function of multiplicity for TOF.	58
7.11	Trigger and vertex efficiencies.	60
7.12	The distributions of the vertex position along the z-axis for data and Monte-Carlo simulations.	60
7.13	Comparison of generated p_T PYTHIA spectra - histograms with reconstructed and corrected PYTHIA spectra - dots with statistical error bars for pions, kaons and protons - upper row. Their ratios - bottom row.	61
7.14	Comparison of generated particle ratios for PHOJET and PYTHIA, i.e. K^+/π^+ ; p/π^+ and p/K^+ , as a function of p_T for MB and two multiplicity bins - upper row and their ratios as a function of p_T - bottom row.	62
7.15	Comparison of generated particle ratios for PHOJET and PYTHIA, i.e. K^+/π^+ ; p/π^+ and p/K^+ , as a function of p_T for different multiplicity bins - upper row and their ratios as a function of p_T for MB - bottom row.	63
8.1	Systematic errors associated with the cut in the number of TPC clusters.	65
8.2	Fits of the systematic errors associated with the cut in the number of TPC clusters.	65
8.3	Systematic errors associated with the cut in the maximum χ^2 per TPC cluster.	67
8.4	Systematic errors associated with the cut in the maximum DCA for the z-direction.	67

8.5	Systematic errors associated with the cut in the maximum TPC-TOF mismatch probability.	67
8.6	Systematic errors associated with the presence of TRD modules in front of the TOF.	68
8.7	Priors determined using an iterative procedure for MB, multiplicity<6 and multiplicity>49.	68
8.8	Systematic errors associated with the use of different priors for the bayesian PID procedure.	69
8.9	Systematic errors associated with the use of a 80% minimum probability cut for the bayesian PID procedure.	69
8.10	Systematic errors associated with the multiplicity variation of the tracking efficiency.	71
8.11	Systematic errors associated with the multiplicity variation of the PID efficiency; only for TOF.	71
8.12	The behavior as a function of multiplicity of the simulated percentage of secondary particles.	71
8.13	Systematic errors associated with the multiplicity variation of the correction for secondary particles; for the kaons this correction is negligible.	72
8.14	Total systematic error for the MB p_T spectra.	73
8.15	Total systematic error for the p_T spectra in multiplicity bins.	73
9.1	The fully corrected MB spectra from this analysis compared with the ALICE “preliminary” ones; includes data from [70].	76
9.2	The fully corrected MB spectrum K^+ from this analysis compared with “preliminary” 7 TeV p+p MB K^+ spectrum, K_s^0 spectrum, kinks spectrum; includes data from [70, 71, 72].	77
9.3	The sum of the MB p_T distributions for identified charged hadrons obtained in this analysis compared with the charged particles spectrum, obtained in other ALICE analyses; includes data from [73, 74].	78
9.4	The summed p_T distributions for identified charged hadrons compared with the charged particles spectra in all multiplicity bins; includes data from [74].	79
9.5	Ratio between ALICE and CMS p_T distributions normalized to integral, for ALICE multiplicity bins 0-6, 7-12, 13-19, 20-28, 29-39, 40-49, 50-59 and 60-71 [76]; includes data from [75].	80
9.6	The fully corrected spectra in different multiplicity bins.	81
9.7	Comparison of the spectra obtained with the 2 trigger settings.	82
9.8	p_T dependence of particle ratios for different multiplicity bins.	83
9.9	Comparison with predictions from PYTHIA and HIJING models; includes data from [80].	84
9.10	Comparison with predictions from PYTHIA and HIJING models; includes data from [80].	84
9.11	p/π^+ ratio for PYTHIA in all multiplicity bins.	85

9.12	$\langle p_T \rangle$ (left) and yields ratios(right) as a function of multiplicity. $\langle p_T \rangle$ as a function of mass in all multiplicity bins (middle) [83].	86
9.13	$\langle p_T \rangle$ as a function of mass for MB obtained in an independent analysis within ALICE Collaboration and in the present analysis, respectively [83]; includes data from [70].	87
9.14	Quality of the simultaneous fit with BGBW, of π^+, K^+, p p_T distributions, for pp data, present analysis, as a function of multiplicity [83].	88
9.15	Quality of the simultaneous fit with BGBW, of π^+, K^+, p p_T distributions, for PYTHIA 6.4 simulations, as a function of multiplicity [83].	89
9.16	Evolution of (T, $\langle \beta \rangle$) values as a function of multiplicity obtained in pp collisions at 7 TeV using this analysis [83].	89
9.17	Evolution of (T, $\langle \beta \rangle$) values as a function of multiplicity obtained in Pb+Pb collisions at 2.76 TeV by the ALICE Collaboration [85].	89
10.1	Two dimensional directivity (mean of D^+ and D^-) versus combined multiplicity.	90
10.2	Two dimensional $d^2N/\Delta\varphi\Delta\eta$ representation for the minimum bias case.	91
10.3	Two dimensional $d^2N/\Delta\varphi\Delta\eta$ representation for $M>30$ & $D<0.3$	91
10.4	Two dimensional directivity (mean) versus combined multiplicity - filled only when simultaneous D^+ and D^- condition was fulfilled.	92
10.5	p_T spectra as a function of directivity in the highest four multiplicity bins.	93
10.6	ratio of the p_T spectra as a function of directivity relative to the spectra in the corresponding multiplicity bin.	93
10.7	p_T spectra as a function of directivity in the 50 - 59 multiplicity bin, plotted separately.	94
10.8	p_T spectra as a function of multiplicity in all the three directivity classes.	94
11.1	Upper row - Multiplicity dependence of the transverse momentum distributions for positive pions, kaons and protons in pp collision at 7 TeV. $z = \langle dN_{ch}/d\eta \rangle_{mult.bin} / \langle dN_{ch}/d\eta \rangle_{mult.>0}$. Bottom row - ratio of transverse momentum distributions in a given multiplicity bin (z) relative to mult.> 0 - ALICE preliminary.	98

11.2	Upper row - p_T dependence of the particle ratios K/p , p/π and p/K as a function of multiplicity in pp collisions at 7 TeV. $z = \langle dN_{ch}/d\eta \rangle_{mult.bin} / \langle dN_{ch}/d\eta \rangle_{mult.>0}$. Bottom row - the ratio of the upper distributions relative to the one for $mult.> 0$ - ALICE preliminary.	99
11.3	ALICE experiment coordinate system [89].	104

List of Tables

4.1	LHC parameters in 2010 [37].	25
5.1	Multiplicity bins correspondence: global tracks - combined multiplicity - generated CMS.	38
5.2	Multiplicity bins correspondence: combined multiplicity - generated PYTHIA multiplicity.	38
5.3	Summary of the event and track cuts used in the present analysis.	41
8.1	Summary of the sources of systematic errors.	74
9.1	Correlation between the number of reconstructed (N_{rec}) and true ($\langle N_{tracks} \rangle$) in the 12 multiplicity bins within $ \eta < 2.4$ range by the CMS collaboration [75].	78

Bibliography

- [1] P. Braun-Munzinger and J. Wambach. Colloquium: Phase diagram of strongly interacting matter. *Rev. Mod. Phys.*, 81:1031–1050, 2009. 6, 7, 105
- [2] F. Halzen and A.D. Martin. *Quarks and Leptons: An Introductory Course in Modern Particle Physics*. ISBN 0-471-88741-2. John Wiley & Sons Inc. 7, 105
- [3] M. Petrovici. Relativistic heavy ion collisions - expectations, experimental facts and future plans, 2012. <http://www.theory.nipne.ro/predeal12/pdf/MPetrovici-Predeal12.pdf>. 8, 10, 11, 15, 105
- [4] N.Cabibo and G.Parisi. Exponential hadronic spectrum and quark liberation. *Phys. Lett. B*, 59:67, 1957. 8
- [5] J.P.Collins and M.J.Perry. Superdense Matter: Neutrons or Asymptotically Free Quarks? *Phys. Rev. Lett.*, 34:1353, 1975. 8
- [6] X. Zhu, M. Bleicher, S.L. Huang, K. Schweda, H. Stöcker, N. Xu, and P. Zhuang. DD* correlations as a sensitive probe for thermalization in high energy nuclear collisions. *Phys. Lett. B*, 647(5-6):366 – 370, 2007. 8, 105
- [7] K. Fukushima and T. Hatsuda. The phase diagram of dense QCD. *Rep. Prog. Phys.*, 74:014001, 2011. 9, 10, 105
- [8] L.V. Gribov et al. Semihard processes in QCD. *Phys. Rep.*, 100:1, 1983. 12, 13, 14, 105
- [9] T. Alexopoulos et al. (E735 Collaboration). The role of double parton collisions in soft hadron interactions. *Phys. Lett. B*, 435:453, 1998. 14, 22
- [10] T. Alexopoulos et al. Evidence for hadronic deconfinement in $\bar{p} - p$ collisions at 1.8 TeV. *Phys. Lett. B*, 528:43, 2002. 14, 22, 23, 106
- [11] S.Z.Belenkji and L.D. Landau. Hydrodynamic Theory of Multiple Production of Particles. *Del Nuov. Cim.*, Suppl. Vol.III, Series X(1):15, 1956. 14

- [12] G.A. Milekhin. Hydrodynamic theory of multiple production of particles in collisions of fast nucleons on nuclei. *Zh. Eksp. Teor. Fiz.*, 35:1185, 1958. 14
- [13] L. Van Hove. Multiplicity dependence of p_t spectrum as a possible signal for a phase transition in hadronic collisions. *Phys. Lett. B*, 118:138, 1982. 14
- [14] B.Andersson, I.Holgersson, and R.Migneron. Generalized Hhydrodynamical Models. *Physica Scripta*, 20:10, 1979. 14
- [15] K.Aamodt et al.(ALICE Collaboration). Elliptic Flow of Charged Particles in Pb-Pb Collisions at $\sqrt{s_{NN}} = 2.76$ TeV. *Phys. Rev. Lett.*, 105:252302, Dec 2010. 17, 105
- [16] A.Andronic and FOPI Coll. Excitation function of elliptic flow in Au+Au collisions and the nuclear matter equation of state. *Phys. Lett. B*, 612:173, 2005. 17
- [17] A.Adare and PHENIX Coll. Scaling Properties of Azimuthal Anisotropy in Au+Au and Cu+Cu collisions at $\sqrt{s_{NN}} = 200$ GeV. *Phys. Rev. Lett.*, 98:162301, 2007. 17, 105
- [18] O.Barannikova and STAR Coll. Probing collision dynamics at RHIC. *nucl-ex/0403014*. 18, 105
- [19] B. I. Abelev et al. (STAR Collaboration). Systematic measurements of identified particle spectra in pp , $d + Au$, and $Au + Au$ collisions at the STAR detector. *Phys. Rev. C*, 79:034909, Mar 2009. 19, 105
- [20] M. Petrovici and A. Pop. Collective Phenomena in Heavy Ion Collisions. *nucl-ex0904.3666*, 2009. 20, 21, 105
- [21] B.I. Abelev and STAR Coll. Strange particle production in p+p collisions at $\sqrt{s} = 200$ GeV. *Phys. Rev. C*, 75:064901, 2007. 20
- [22] M.Petrovici and A.Pop. Selected aspects of flow phenomena in heavy ion collisions. *AIP Conf. Proc.*, 972:98, 2008. 20, 21, 105
- [23] M. Petrovici, I. Berceanu, A. Pop, C. Andrei, and A. Herghelegiu. Centrality dependence of mid-rapidity charged particles density in relativistic heavy ion collisions - energy scaling. *J. Phys.: Conf. Ser.*, 413:012022, 2013. 21
- [24] G.J.Alner et al. (UA5 Collaboration). Scaling violations in multiplicity distributions at 200 and 900 GeV. *Phys. Lett. B*, 167:476, 1986. 21, 105
- [25] T. Alexopoulos et al. (E735 Collaboration). Mass-identified particle production in proton-antiproton collisions at $\sqrt{s} = 300, 540, 1000$ and 1800 GeV. *Phys. Rev. D*, 48:984, 1993. 21, 22, 105, 106

- [26] G.J. Alner et al. (UA5 Collaboration). Kaon production in pp reactions at a center-of-mass energy of 540 GeV. *Nucl. Phys. B*, 258:505, 1985. 21, 22, 106
- [27] E. Fermi. Angular Distribution of the Pions Produced in High Energy Nuclear Collisions. *Phys. Rev.*, 81:683, 1951. 21
- [28] R. Hagedorn. Multiplicities, p_t distributions and the expected hadron - quark-gluon phase transition. *Riv. Nuovo Cim.*, 6(10):1, 1983. 21, 85
- [29] S. Kagiama et al. A Signal of Hydrodynamical Transverse Flow in High Energy Hadronic Collisions. *Progr. Theor. Phys.*, 81(2):266, 1989. 21, 22, 106
- [30] T. Sjostrand and P. Skands. Multiple Interactions and the Structure of Beam Remnants. *arXiv:hep-ph/0402078*, 2004. 22, 48
- [31] R. Corke. Multiple Interactions in PYTHIA 8. *arXiv:hep-ph/0901.2852*. 22, 48
- [32] K. Werner et al. Parton ladder splitting and the rapidity dependence of transverse momentum spectra in deuteron-gold collisions at the BNL Relativistic Heavy Ion Collider. 22, 48
- [33] D. Acosta et al. (CDF Collaboration). Soft and hard interactions in $p\bar{p}$ collisions at $\sqrt{s} = 1800$ and 630 GeV. *Phys. Rev. D*, 65:072005, 2002. 22, 23, 106
- [34] K. Aamodt et al. (ALICE Collaboration). Femtoscopy of pp collisions at $\sqrt{s} = 0.9$ and 7 TeV at the LHC with two-pion Bose-Einstein correlations. *Phys. Rev. D*, 84:112004, 2011. 22, 23, 106
- [35] CERN. *LHC Design Report*, volume 1. CERN-2004-003, June 2004. 24
- [36] CERN. Accelerator Complex. <https://espace.cern.ch/acc-tec-sector/default.aspx>. 24, 106
- [37] Mike Lamont for the LHC team. LHC Status and Plans, December 2010. <http://lhc-commissioning.web.cern.ch/lhc-commissioning/presentations/2010/lhc-status-ann-arbor.pptx>. 25, 110
- [38] ALICE Collaboration. ALICE: Physics Performance Report, Volume I. *J. Phys. G: Nucl. Part. Phys.*, 30:1517 – 1763, 2004. 25, 26, 28, 29, 31, 106
- [39] ALICE Collaboration. *Technical Design Report of the Inner Tracking System*. CERN/LHCC/1999-12, 1999. 25

- [40] V. Manzari. The present Inner Tracking System - Steps forward! *ALICE Matters*, December 2012. http://alicematters.web.cern.ch/?q=ALICE_currentITS. 27, 106
- [41] ALICE Collaboration. *Technical Design Report of the Time-Projection Chamber*. CERN/LHCC/2000-01, 2000. 27
- [42] ALICE Collaboration. *Technical Design Report of the Transition-Radiation Detector*. CERN/LHCC/2001-21, 2001. 27
- [43] ALICE Collaboration. ALICE Figures Repository. https://aliceinfo.cern.ch/Figure/general_fig. 29, 44, 46, 106
- [44] ALICE Collaboration. *Technical Design Report of the Time-Of-Flight Detector*. CERN/LHCC/2000-12, 2000. 28
- [45] ALICE Collaboration. *Technical Design Report on Forward Detectors*. CERN/LHCC/2004-25, 2004. 29, 30
- [46] AliRoot website. <http://aliweb.cern.ch/Offline/>. 30
- [47] ROOT website. <http://root.cern.ch/drupal/>. 31
- [48] Saiz P et al. AliEn - ALICE environment on the GRID. *Nucl. Instrum. Methods A*, 502:437, 2003. <http://alien.cern.ch/>. 31
- [49] MonALISA Repository for ALICE. <http://alimonitor.cern.ch/map.jsp>. 32, 106
- [50] ALICE collaboration. Charged-particle multiplicity measurement in proton-proton collisions at $\sqrt{s} = 0.9$ and 2.36 TeV with ALICE at LHC. *Eur. Phys. J. C*, 68:89, 2010. 33
- [51] ALICE collaboration. Transverse momentum spectra of charged particles in proton-proton collisions at $\sqrt{s} = 900$ GeV with ALICE at the LHC. *Phys. Lett. B*, 693:53, 2010. 33
- [52] A. Dainese and M. Masera. *ALICE-INT-2003-27*, 2003. 35
- [53] ALICE Collaboration. ALICE: Physics Performance Report, Volume II. *J. Phys. G: Nucl. Part. Phys.*, 32:1295 – 2040, 2006. 36, 41, 43
- [54] V. Karimäki. *CMS Note 1997/051*, 1997. 36
- [55] R.Shahoyan. ALICE Internal Communication. <https://indico.cern.ch/getFile.py/access?contribId=0&sessionId=0&resId=1&materialId=slides&confId=145707>. 36
- [56] A. Alkin. ALICE Internal Communication. <https://indico.cern.ch/getFile.py/access?contribId=25&resId=0&materialId=slides&confId=147348>. 37, 106

- [57] P. Billoir. Track fitting with multiple scattering: a new method. *Nucl. Instrum. Methods A*, 225:352, 1984. 40
- [58] Cristian Andrei, Ionela Berceanu, Alexandru Bercuci, Andrei Herghelegiu, Francesco Noferini, Mihai Petrovici, and Amalia Pop. Collective phenomena in p+p collisions at 7 Tev for high multiplicity and near azimuthal isotropic events. *Internal Note*, January 2011. https://twiki.cern.ch/twiki/pub/ALICE/PWGLFPAGSPECTRAMultiplicityEventShapePP7/coll_ph_pp_ALICE_internal_note_310111.pdf. 42, 88
- [59] W. Blum and L. Rolandi. *Particle Detection with Drift Chambers*. Springer, Berlin, 1998. 43
- [60] ALICE Collaboration. *Addendum to the Technical Design Report of the Time of Flight System (TOF)*. CERN / LHCC 2002-016, April 2002. 45
- [61] F. Noferini Internal Communication. Prospects for combined TOF + TPC PID. *Jyvaskyla - ALICE Physics Week*, sep 1st 2011. 46, 52
- [62] S. Roesler, R.Engel, and J. Ranft. The Monte Carlo event generator DPMJET-III. *Lisbon 2000-Advanced Monte Carlo*, pages 1033–1038, 2000. [hep-ph/0012252]. 48
- [63] Xin-Nian Wang and Miklos Gyulassy. HIJING: A Monte Carlo model for multiple jet production in pp, pA, and AA collisions. *Phys.Rev.D*, 44:3501, 1991. 48
- [64] S. Agostinelli et al. *A simulation toolkit*, CERN-IT-20020003, KEK Preprint 2002-85, SLAC-PUB-9350Proc., 2002. <http://wwwinfo.cern.ch/asd/geant4/geant4.html>. 48
- [65] A. Fass et al. *Proc. of Computing in High Energy and Nuclear Physics, La Jolla, California*, 2003. <http://www.slac.stanford.edu/econf/C0303241/proc/papers/MOMT004.PDF>. 48
- [66] Cristian Andrei, Ionela Berceanu, Alexandru Bercuci, Andrei Herghelegiu, Francesco Noferini, Mihai Petrovici, and Amalia Pop. Material and weak decay contaminations. *Internal Note*, April 2012. https://twiki.cern.ch/twiki/pub/ALICE/PWGLFPAGSPECTRAMultiplicityEventShapePP7/coll_ph_pp_ALICE_internal_note_3_04042012.pdf. 55
- [67] Cristian Andrei, Ionela Berceanu, Alexandru Bercuci, Andrei Herghelegiu, Francesco Noferini, Mihai Petrovici, and Amalia Pop. Multiplicity dependence of the efficiency correction. *Internal Note*, April 2012. <https://twiki.cern.ch/twiki/pub/ALICE/>

- PWGLFPAGSPECTRAMultiplicityEventShapePP7/coll_ph_pp_ALICE_analysis_note_4_04042012_v2.pdf. 56
- [68] M. Chojnacki. ALICE Internal Communication. <https://indico.cern.ch/getFile.py/access?contribId=0&resId=0&materialId=slides&confId=217294>. 60
- [69] ALICE Collaboration. Production of pions, kaons and protons in pp collisions at $\sqrt{s}=900$ GeV with ALICE at the LHC. *Eur. Phys. J. C*, 71:1655, 2011. 70
- [70] F. Barile on behalf of the ALICE experiment. Light flavour hadron production in pp and Pb-Pb collisions in the ALICE experiment at the LHC. *LHCP 2013 Conference*. <https://indico.cern.ch/getFile.py/access?contribId=322&sessionId=15&resId=0&materialId=slides&confId=210555>. 75, 76, 77, 87, 108, 109
- [71] D.D. Chinellato for the ALICE Collaboration. Strange and Multi-Strange Particle Production in ALICE. *Hot Quarks 2012*, October 2012. 76, 77, 108
- [72] M. Spyropoulou-Stassinaki. ALICE Internal Communication. <https://aliceinfo.cern.ch/Notes/node/148>. 76, 77, 108
- [73] ALICE Collaboration. Energy Dependence of the Transverse Momentum Distributions of Charged Particles in pp Collisions Measured by ALICE. *arXiv:1307.1093v1 [nucl-ex]*. <http://arxiv.org/abs/1307.1093v1>. 77, 78, 108
- [74] A. Herghelegiu. *Studies of charged hadrons p_T spectra for high multiplicity and nearly azimuthal isotropic events in p+p collisions at 7 TeV*. PhD thesis, University of Bucharest, 2013. 77, 78, 79, 108
- [75] CMS Collaboration. Spectra of identified charged hadrons at $\sqrt{s}=0.9, 2.76$ and 7 TeV via tracker energy loss. *CMS PAS FSQ-12-014*. 77, 78, 80, 108, 110
- [76] A. Pop, C. Andrei, I. Berceanu, A. Bercuci, A. Herghelegiu, and M. Petrovici. p_T spectra of charged particles and identified hadrons as a function of multiplicity in p+p collisions at 7 TeV, May 2013. <https://indico.cern.ch/getFile.py/access?contribId=2&sessionId=0&resId=0&materialId=slides&confId=251564>. 80, 108
- [77] Cristian Andrei, Ionela Berceanu, Alexandru Bercuci, Andrei Herghelegiu, Mihai Petrovici, and Amalia Pop. Identified charged hadrons p_t spectra as a function of multiplicity in p+p collisions at 7

- TeV- v4. *Internal Note*, April 2013. https://aliceinfo.cern.ch/Notes/sites/aliceinfo.cern.ch.Notes/files/notes/analysis/candrei/2013-Jul-01-analysis_note-InternalNote_v4.pdf. 83
- [78] T. Sjostrand, S. Mrenna, and P. Skands. PYTHIA 6.4 physics and manual. *JHEP05*, 026, 2006. 83
- [79] V. Topor Pop et al. Strong longitudinal color-field effects in pp collisions at energies available at the CERN Large Hadron Collider. *Phys. Rev. C*, 83:024902, 2011. and references therein. 83
- [80] V. Topor Pop. Private Communication. 83, 84, 108
- [81] C. Tsallis. Possible generalization of boltzmann-gibbs statistics. *J. Statist. Phys.*, 52:479–487, 1988. 85
- [82] A.A. Rostovtsev and A.A. Bylinkin. Systematic studies of hadron production spectra in collider experiments. *ArXiv:1008.0332v2*. [hep-ph]. 85, 86
- [83] A. Pop, C. Andrei, I. Berceanu, A. Bercuci, A. Herghelegiu, and M. Petrovici. Status of identified charged hadrons pT spectra as a function of multiplicity in p+p collisions at 7 TeV, April 2013. <https://indico.cern.ch/getFile.py/access?contribId=15&sessionId=1&resId=0&materialId=slides&confId=245355>. 86, 87, 88, 89, 109
- [84] Cristian Andrei, Ionela Berceanu, Alexandru Bercuci, Andrei Herghelegiu, Mihai Petrovici, and Amalia Pop. Identified charged hadrons p_t spectra as a function of multiplicity in p+p collisions at 7 TeV - v1. *Internal Note*, April 2013. https://aliceinfo.cern.ch/Notes/sites/aliceinfo.cern.ch.Notes/files/notes/analysis/candrei/2013-Apr-08-analysis_note-InternalNote_080413.pdf. 86, 87
- [85] ALICE Collaboration. Centrality Dependence of π , k, p Production in Pb-Pb Collisions at $\sqrt{s_{NN}} = 2.76$ TeV. *arXiv:1303.0737[hep-ex]*, March 2013. 88, 89, 109
- [86] J. P. Alard et al. Midrapidity source of intermediate-mass fragments in highly central collisions of Au + Au at 150 AMeV. *Phys. Rev. Lett.*, 69:889–892, Aug 1992. 90
- [87] Cristian Andrei, Ionela Berceanu, Alexandru Bercuci, Andrei Herghelegiu, Francesco Noferini, Mihai Petrovici, and Amalia Pop. Transverse momentum distributions of pions, kaons and protons for high multiplicity and close to azimuthal isotropic events in 7 tev pp collisions with the alice experiment at the lhc (short

- analysis note based on the previous notes and presentations). *Internal Note*, April 2012. https://twiki.cern.ch/twiki/pub/ALICE/PWGLFPAGSPECTRAMultiplicityEventShapePP7/coll_ph_pp_ALICE_internal_note_310111.pdf. 91
- [88] ALICE Collaboration. Definition of the alice coordinate system and basic rules for sub-detector components numbering. *ALICE-INT-2003-038*, 2003. <https://edms.cern.ch/document/406391/2>. 103
- [89] Thomas Bird. An Overview of the ALICE Experiment. January 2010. <http://static.thomasbird.com/files/the-alice-experiment.pdf>. 104, 110

Acknowledgments

I would like to express my deep gratitude to Prof. Dr. Mihai Petrovici, my research supervisor, for his continues guidance and useful critiques of this research work. Also, I would like to thank him for providing me with the opportunity to work in a remarkable research environment.

I would also like to thank Dr. Amalia Pop, for her invaluable contribution at the interpretation of the results obtained in this analysis.

With Prof. Dr. Mihai Petrovici, Dr. Amalia Pop, Dr. Ionela Berceanu, Dr. Alexandru Bercuci and Andrei Herghelegiu I had long and fruitful discussions, within the ALICE analysis group, without which this analysis would have not been possible.

I would also like to extend my thanks to all the members of the Hadron Physics Department.

Finally, I wish to thank my family for their support and encouragement throughout this period.